

ISTANBUL TECHNICAL UNIVERSITY ★ GRADUATE SCHOOL OF SCIENCE
ENGINEERING AND TECHNOLOGY

**NUMERICAL MODELLING OF SAND BEHAVIOR UNDER CYCLIC
SIMPLE SHEAR TESTS IN A SPECIAL LIQUEFACTION BOX**

M.Sc. THESIS

Ataollah Nateghi

Department of Civil Engineering

Soil Mechanics And Geotechnical Engineering Program

AUGUST 2015

ISTANBUL TECHNICAL UNIVERSITY ★ GRADUATE SCHOOL OF SCIENCE
ENGINEERING AND TECHNOLOGY

**NUMERICAL MODELLING OF SAND BEHAVIOR UNDER CYCLIC
SIMPLE SHEAR TESTS IN A SPECIAL LIQUEFACTION BOX**

M.Sc. THESIS

**Ataollah Nateghi
(501121302)**

Department of Civil Engineering

Soil Mechanics And Geotechnical Engineering Program

Thesis Advisor: Assist. Prof. Dr. E. Ece BAYAT

AUGUST 2015

İSTANBUL TEKNİK ÜNİVERSİTESİ ★ FEN BİLİMLERİ ENSTİTÜSÜ

**ÖZEL SIVILAŞMA DÜZENEĞİ İÇİNDE ÇEVİRİMSSEL BASİT KESME
DENEYLERİ ALTINDA KUM DAVRANIŞININ SAYISAL
MODELLENMESİ**

YÜKSEK LİSANS TEZİ

**Ataollah Nateghi
(501121302)**

İnşaat Mühendisliği Anabilim Dalı

Zemin Mekaniği ve Geoteknik Mühendisliği Lisansüstü Programı

Tez Danışmanı: Y.Doç. Dr. E. Ece BAYAT

AĞUSTOS 2015

Ataollah Nateghi, a **M.Sc.** student of ITU **Institute of Science** student ID **501121302** successfully defended the **thesis** entitled “**Numerical Modelling of Sand Behavior under Cyclic Simple Shear Tests in a Special Liquefaction Box**” which he prepared after fulfilling the requirements specified in the associated legislations, before the jury whose signatures are below.

Thesis Advisor : **Assist. Prof.Dr. Esra Ece BAYAT**
Istanbul Technical University

Jury Members : **Prof. Dr. Recep İYİSAN**
Istanbul Technical University

Assoc.Prof. Dr. Özer ÇİNİCİOĞLU
Bogazici University

Date of Submission : 4 May 2015
Date of Defense : 18 August 2015

To whom I love,

FOREWORD

I wish to extend my appreciation to my academic advisor Dr. Esra Ece Bayat for her valuable guidance, and support. I would like to thank her for giving me the opportunity to participate in this research and helping me improve my academic skills.

I would like to thank my colleague Navid Jadidoleslam for his effort and contribution on this research. Working in a team decreased the hardships and made the research more enjoyable.

I wish to thank my girlfriend, Sahar Haddadian for her support, encouragement, and understanding me during the process of writing this thesis. I wish to thank her for being patient in hard days of being far away.

I wish to thank my parents, Farzaneh Nasirzonouzi and Esmaeil Nateghi who dedicate their life providing me the best future. I thank for their support, trust, and patience while being away from home to achieve my goals. I would like to thank my brother and sister Aref Nateghi and Niloufar Nateghi for their endless support, and true love.

This research is funded by TÜBİTAK (TÜRKİYE BİLİMSEL ve TEKNOLOJİK ARAŞTIRMA KURUMU) with project No: 213M367 started in 2014. The support of TÜBİTAK is greatly appreciated. The thesis is prepared in Soil Mechanics and Geotechnical Engineering Program of Istanbul Technical University. The support of the department faculty and administrators are greatly appreciated.

August 2015

Ataollah Nateghi
Civil Engineer

TABLE OF CONTENTS

	<u>Page</u>
FOREWORD.....	IX
TABLE OF CONTENTS.....	XI
ABBREVIATIONS	XIII
LIST OF TABLES	XV
LIST OF FIGURES	XVII
SUMMARY	XXI
ÖZET.....	XXIII
1. INTRODUCTION.....	1
2. LITERATURE REVIEW.....	5
2.1 Liquefaction Evaluation Approaches	5
2.2 Cyclic Stress Liquefaction Evaluation Approach	6
2.2.1 Characterization of liquefaction resistance based on laboratory test	7
2.2.2 Characterization of liquefaction resistance based on in situ tests	9
2.2.3 Evaluation of initial liquefaction.....	10
2.3 Cyclic Strain Liquefaction Evaluation Approach	11
2.3.1 Characterization of loading conditions	12
2.3.2 Characterization of liquefaction resistance	12
2.3.3 Evaluation of liquefaction potential	13
2.4 Other Liquefaction Evaluation Approaches	13
2.5 Liquefaction Induced Deformations.....	15
2.5.1 Sand boils	15
2.5.2 Settlement.....	15
2.5.2.1 Settlement of dry sand.....	15
2.5.2.2 Settlement of saturated sands	16
2.6 Liquefaction Mitigation Methods.....	17
2.7 New Mitigation Method for Liquefaction (IPS Method)	18
2.7.1 Experimental setup of IPS.....	19
2.7.2 Mathematical model for prediction of pore water pressure ratio in IPS ...	22
3. NUMERICAL MODELING OF GEOTECHNICAL PROBLEM IN FLAC^{3D}	25
3.1 Grid Generation.....	27
3.2 Boundary Conditions.....	28
3.3 Initial Conditions.....	29
3.4 Soil Models	30
3.4.1 Algorithm Used in Constitutive Models in FLAC ^{3D}	31
3.4.2 Elastic model.....	32
3.4.3 Mohr-Coulomb model.....	33
3.5 Dynamic Loading and Damping	34
3.6 Numerical Modeling of Liquefaction.....	38

3.6.1 Relationship between the volume reduction and pore-water pressure increment.....	39
3.6.2 Volumetric strain increment calculation	40
3.6.2.1 Martin equation	40
3.6.2.2 Byrne equation	40
4. NUMERICAL MODEL OF CYCLIC SIMPLE SHEAR STRAIN TESTS ON SHAKING TABLE	43
4.1 Overview of Cyclic Simple Shear Liquefaction Box (CSSLB)	43
4.2 Material Properties	47
4.2.1 Mass density	48
4.2.2 Deformability properties of sand.....	48
4.2.2.1 Shear modulus of sand	49
4.2.2.2 Bulk modulus of sand.....	53
4.2.3 Strength properties of sand.....	54
4.3 Dynamic Analysis of Numerical Model.....	55
4.3.1 Maximum unbalanced force.....	57
4.3.2 Shear stress-shear strain behavior	57
4.4 Liquefaction Analysis of Numerical Model	58
4.4.1 Fully saturated sand analysis.....	58
4.4.2 Partially saturated sand analysis.....	60
5. NUMERICAL ANALYSIS RESULTS IN FLAC^{3D}	63
5.1 Dynamic Analysis Results.....	63
5.1.1 Simple shear condition verification.....	63
5.1.2 Settlement of sand under dynamic loading	69
5.2 Liquefaction Analysis Results.....	75
5.2.1 Comparison of experimental and numerical model results for fully saturated sand.....	75
5.2.2 Settlement of sand due to liquefaction	80
5.2.3 Liquefaction analysis of fully saturated sand at high effective stresses....	82
5.2.3.1 Numerical model results under high effective stress	82
5.2.3.2 Empirical formulation for number of cycles to reach liquefaction (N_L)	88
5.2.4 Numerical model results for partially saturated sand.....	95
5.3 Numerical Analysis Results for Free-Field Model.....	98
5.3.1 Numerical results for fully saturated sand in free-field.....	102
5.3.2 Numerical results for partially saturated sand in free-field.....	105
6. SUMMARY AND CONCLUSION.....	110
APPENDICES	116
CURRICULUM VITAE	133

ABBREVIATIONS

CDSS	: Cyclic Direct Shear Strain
CPT	: Cone Penetration Test
CSR	: Cyclic Stress Ratio
CUSSA Mk7	: Cambridge University Simple Shear Apparatus Mk7
FLAC^{3D}	: Fast Lagrangian Analysis of Continua in 3Dimensions
IPS	: Induced Partial Saturation
NGISSA	: Norwegian Geotechnical Institute Simple Shear Apparatus
NULB	: Northeastern University Liquefaction Box
PPT	: Pore Pressure Transducer
RuPSS	: r_u for Partially Saturated Sand
SPT	: Standard Penetration Test
TÜBİTAK	: Türkiye Bilimsel Ve Teknolojik Araştırma Kurumu

LIST OF TABLES

	<u>Page</u>
Table 3.1 : Primitive mesh shapes available with the GENERATE zone command.	27
Table 3.2 : Numerical fits to Seed & Idriss data for sand (FLAC 3D version 5, 2012).	37
Table 4.1 : Material properties used for numerical modelling of CSSLB	47
Table 4.2 : Relation between corrected $(N_1)_{60}$ and Relative Density (D_r) (Das, n.d.).	52
Table 4.3 : Poisson ratio for uniform sand (Skoglund, G. R. Marcuson III, W.F and Cunny, 1976).....	54
Table 4.4 : Friction angle of different material (Rc Chaney, Demars, Santamarina, & Cho, 2001).	54
Table 4.5 : Bulk modulus of water under different pressure and temperature.....	60
Table 5.1 : Dynamic settlement of sand in CSSLB under cyclic simple shear strain tests ($\gamma=0.052\%$).....	74
Table 5.2 : Volumetric strain for different γ and D_r	82
Table 5.3 : Possibility of liquefaction at different depths for field affected by Northridge earthquake.	103
Table 5.4 : Comparison of r_u 's obtained from RuPSS and numerical model.	108
Table A-1: Comparing experimental and numerical results when $\gamma^0=0.05$	116
Table A-2: Comparing experimental and numerical results when $\gamma^0=0.01$	116
Table A-3: Comparing experimental and numerical results when $\gamma^0=0.1$	117
Table B-1: Number of cycles to reach liquefaction under higher effective stress for sand with $D_r=20\%$	118
Table B-2: Number of cycles to reach liquefaction under higher effective stress for sand with $D_r=40\%$	120
Table B-3: Number of cycles to reach liquefaction under higher effective stress for sand with $D_r=60\%$	123

LIST OF FIGURES

	<u>Page</u>
Figure 2.1 : Zones of susceptibility of flow liquefaction (Kramer, 1996).	6
Figure 2.2 : Zones of susceptibility of cyclic mobility (Kramer, 1996).	6
Figure 2.3 : Rate of pore pressure generation in cyclic shear test(De Alba, P and Pyke, 1987).	9
Figure 2.4 : Zones of liquefaction is identified (Kramer, 1996).	10
Figure 2.5 : Relationship between residual excess pore pressure and factor of safety against liquefaction for level ground sites(Marcuson, William F., III, Hynes,M.E and Franklin, 1990).	11
Figure 2.6 : Chart for estimation of volumetric strain in saturated sand from cyclic stress ratio (Tokimatsu, K and Seed, 1987).	16
Figure 2.7 : Estimating the post liquefaction volumetric strain of clean sand as function of factor of safety (Ishihara, 1992).	17
Figure 2.8 : X-Displacements for the Plan View Model Normalized by the X- Displacements of the Mid-Points of Three Lines at $i = 6, 13$, and 20(Ortakci,2007).	21
Figure 2.9 : X-Displacements for the Plan View Model Normalized by the X- Displacements of the Mid-Points of Three Lines at $i = 6, 13$, and 20(Ortakci,2007).	22
Figure 3.1 : Dynamic boundary conditions in FLAC ^{3D}	29
Figure 3.2 : Mohr-Coulomb failure criterion 34	34
Figure 3.3 : Loose of energy under loading (damping) 36	36
Figure 3.4 : Modulus Reduction curve for sand (Seed and Idriss, 1970). 37	37
Figure 4.1 : Schematic Drawing of the Simple-Shear Test Setup 44	44
Figure 4.2 : Shaking Table of Northeastern University and CSSLB box. 45	45
Figure 4.3 : Simple shear mechanism for the CSSLB: (a) plan section before shearing, (b) elevation section before shearing, and (c) elevation section after shearing by displacing shaking table.(Eseller-Bayat et al., 2013). 46	46
Figure 4.4 : CSSLB and simple shear direction. 47	47
Figure 4.5 : Shear stress vs. Shear strain (Kramer, 1996). 49	49
Figure 4.6 : Bender elements locations in plan view (Eseller-Bayat, 2009). 50	50
Figure 4.7 : Shear wave velocity for $D_r=21\%$ (Eseller-Bayat, 2009). 51	51
Figure 4.8 : Shear wave velocity for $D_r=70\%$ by (Eseller-Bayat, 2009). 51	51
Figure 4.9 : Expansion of element in load perpendicular direction and compression in load vertical direction 53	53
Figure 4.10 : The applied velocity wave to the model. 55	55
Figure 4.11 : Maximum unbalanced force when $D_r=42\%$ and $\gamma = 0.052\%$ for dynamic model. 57	57

Figure 4.12 : Shear stress and strain relationship.....	58
Figure 4.13 : Micro picture of partially saturated sand (S=80%) (Eseller-Bayat, 2009).	61
Figure 5.1: Middle section view of the CSSLB in Z-direction (A-A section view) ..	64
Figure 5.2: X-Displacement of specimen in section view when $\gamma = 0.05\%$	64
Figure 5.3: X-Displacement of specimen in section view when $\gamma = 0.1\%$	65
Figure 5.4: X-Displacement of specimen in section view when $\gamma = 0.2\%$	65
Figure 5.5: Displacements of the specimen in X-direction for different shear strains	66
Figure 5.6: Uniform simple shear strains throughout the depth of specimen.....	66
Figure 5.7: Observed shear strain for different zones of the specimen from FISH ...	67
Figure 5.8: Different cross sections studied for X-displacement	68
Figure 5.9: X-displacement at different cross sections in Z-direction	68
Figure 5.10: X-displacement at different cross sections in X-direction.....	69
Figure 5.11: Settlement of fully saturated sand with $D_r=20\%$ under 10 kPa load under cyclic simple shear strain tests with $\gamma=0.052\%$ (using G_{max} from eqn 5.1).	70
Figure 5.12: Settlement in dry sand with $D_r=20\%$ under 10 kPa load under cyclic simple shear strain tests with $\gamma=0.052\%$ (using G_{max} from eqn 5.1).....	70
Figure 5.13: Settlement in fully saturated sand with $D_r=40\%$ under 10 kPa load under cyclic simple shear strain tests with $\gamma=0.052\%$ (using G_{max} from eqn 5.1).	71
Figure 5.14: Settlement in dry sand with $D_r=40\%$ under 10 kPa load under cyclic simple shear strain tests with $\gamma=0.052\%$ (using G_{max} from eqn 5.1).....	71
Figure 5.15: Settlement in fully saturated sand with $D_r=20\%$ under 10 kPa load under cyclic simple shear strain tests with $\gamma=0.052\%$ (using G_{max} from eqn 5.2).	72
Figure 5.16: Settlement in dry sand with $D_r=20\%$ under 10 kPa load under cyclic simple shear strain tests with $\gamma=0.052\%$ (using G_{max} from eqn 5.2).....	73
Figure 5.17: Settlement in fully saturated sand with $D_r=40\%$ under 10 kPa load under cyclic simple shear strain tests with $\gamma=0.052\%$ (using G_{max} from eqn 5.2).	73
Figure 5.18: Settlement in dry sand with $D_r=40\%$ under 10 kPa under cyclic simple shear strain tests with $\gamma=0.052\%$ (using G_{max} from eqn 5.2).	74
Figure 5.19: Excess pore water pressure generations in numerical analysis when $\sigma'_v=2.4$ kPa, $D_r=60\%$ and $\gamma=0.005\%$	76
Figure 5.20: Comparison of excess pore water pressure generations in numerical analysis and experimental tests when $\sigma'_v=2.4$ kPa, $D_r=31\%$ and $\gamma=0.0525\%$	76
Figure 5.21: Comparison of excess pore water pressure generations in numerical analysis and experimental tests when $\sigma'_v=2.5$ kPa, $D_r=62\%$ and $\gamma=0.0525\%$	77
Figure 5.22: r_u vs. Number of cycles when $\gamma=0.1\%$, $D_r=40\%$, $\sigma'_v=25$ kPa and 100kPa	78
Figure 5.23: Cyclic Direct Shear Strain (CDSS) test results for sand when $\gamma=0.1\%$, D_r is 40% in average and $\sigma'_v =100$ kPa and 25 kPa(Hazirbaba, 2005)..	78
Figure 5.24: r_u vs Number of cycles when $\gamma=0.294\%$, $D_r=40\%$ and $\sigma'_v=25$ kPa and 100kPa.....	79

Figure 5.25: Cyclic Direct Shear Strain (CDSS) test results results for sand when $\gamma=0.3\%$, D_r is 40% in average and $\sigma'_v=100$ kPa and 25 kPa(Hazirbaba, 2005).	79
Figure 5.26: Relationship between post liquefaction volumetric strain and maximum shear strain during undrained loading of sand(Ishihara, Yoshimini 1992)	81
Figure 5.27: σ'_v (Pa) vs. time (sec) when $\sigma'_v=25$ kPa, $\gamma=0.05\%$, $D_r=40\%$	83
Figure 5.28: σ'_v (Pa) vs. time (sec) when $\sigma'_v=35$ kPa, $\gamma=0.05\%$, $D_r=40\%$	83
Figure 5.29: σ'_v (Pa) vs. time (sec) when $\sigma'_v=45$ kPa, $\gamma=0.05\%$, $D_r=40\%$	83
Figure 5.30: Comparison of r_u vs N_L for fully saturated sand with $D_r=20\%$, $D_r=40\%$ and $D_r=60\%$ under $\gamma=0.1\%$ and $\sigma'_v=20$ kPa.....	84
Figure 5.31: Comparison of r_u vs N_L for fully saturated sand with $D_r=20\%$, $D_r=40\%$ and $D_r=60\%$ under $\gamma=0.2\%$ and $\sigma'_v=20$ kPa.....	84
Figure 5.32: Comparison of r_u vs N_L for fully saturated sand with $D_r=20\%$, $D_r=40\%$ and $D_r=60\%$ under $\gamma=0.2\%$ and $\sigma'_v=50$ kPa.....	85
Figure 5.33: N_L vs. σ'_v (kPa) when $D_r=20\%$ and $\gamma=0.05\%$, $\gamma=0.1\%$, $\gamma=0.2\%$	85
Figure 5.34: N_L vs. σ'_v (kPa) when $D_r=40\%$ and $\gamma=0.05\%$, $\gamma=0.1\%$, $\gamma=0.2\%$	86
Figure 5.35: N_L vs. σ'_v (kPa) when $D_r=60\%$ and $\gamma=0.05\%$, $\gamma=0.1\%$, $\gamma=0.2\%$	86
Figure 5.36: N_L vs. σ'_v (kPa) when $\gamma=0.05\%$ and $D_r=20\%$, $D_r=40\%$, $D_r=60\%$	87
Figure 5.37: N_L vs. σ'_v (kPa) when $\gamma=0.1\%$ and $D_r=20\%$, $D_r=40\%$, $D_r=60\%$	87
Figure 5.38: N_L vs. σ'_v (kPa) when $\gamma=0.2\%$ and $D_r=20\%$, $D_r=40\%$, $D_r=60\%$	88
Figure 5.39: N_L as a function of vertical effective stresses for different shear strains for $D_r=40\%$ (Eseller-Bayat, 2009).	88
Figure 5.40: Comparison between FLAC ^{3D} and linear equation results when $\gamma=0.05\%$ and $D_r=40\%$	89
Figure 5.41: Comparison between FLAC ^{3D} and linear equation results when $\gamma=0.1\%$ and $D_r=40\%$	89
Figure 5.42: Comparison between FLAC ^{3D} and linear equation results when $\gamma=0.2\%$ and $D_r=40\%$	90
Figure 5.43: Comparison of of the N_L results obtained from FLAC ^{3D} and the developed equation for different σ'_v , when $\gamma=0.2\%$ and $D_r=20\%$	91
Figure 5.44: Residuals of N_L obtained from FLAC ^{3D} analysis and N_L obtained from the developed equation for different σ'_v , when $\gamma=0.2\%$ and $D_r=20\%$	92
Figure 5.45: Comparison of N_L results obtained from FLAC ^{3D} and the developed equation for different σ'_v , when $\gamma=0.2\%$ and $D_r=40\%$	92
Figure 5.46: Residuals of the N_L results obtained from FLAC ^{3D} and the developed equation for different σ'_v , when $\gamma=0.2\%$ and $D_r=40\%$	93
Figure 5.47: Comparison of N_L results obtained from FLAC ^{3D} and the developed equation for different σ'_v , when $\gamma=0.2\%$ and $D_r=60\%$	93
Figure 5.48: Residuals of N_L obtained from FLAC ^{3D} analysis and N_L obtained from the developed equation for different σ'_v , when $\gamma=0.2\%$ and $D_r=60\%$	94
Figure 5.49: Comparison of modified equation and linear equation by Eseller-Bayat (2009), when $\gamma=0.1\%$ and $D_r=40\%$	94
Figure 5.50: Comparison of modified equation and linear equation by Eseller-Bayat (2009), when $\gamma=0.15\%$ and $D_r=40\%$	95
Figure 5.51: Comparison of modified equation and linear equation by Eseller-Bayat (2009), when $\gamma=0.2\%$ and $D_r=40\%$	95
Figure 5.52: r_u vs. Number of cycles for partially saturated sand when $\gamma=0.1\%$, $D_r=35\%$ and $\sigma'_v=2.5$ kPa and $S=84\%$	96

Figure 5.53: r_u vs. Number of cycles for partially saturated sand when $\gamma=0.1\%$, $D_r=37\%$ and $\sigma'_v=2.5$ kPa and $S=72\%$.	97
Figure 5.54: r_u vs. Number of cycles for partially saturated sand when $\gamma=0.2\%$, $D_r=47\%$ and $\sigma'_v=2.5$ kPa and $S=53\%$.	97
Figure 5.55: Concept of equivalent number of cycles for an earthquake with magnitude M (Eseller-Bayat, 2009).	99
Figure 5.56: Earthquake magnitude (M) vs. N_γ (Eseller-Bayat, 2009).	100
Figure 5.57: Free field model in $FLAC^{3D}$.	101
Figure 5.58: Acceleration, Velocity and displacement records of Northridge earthquake from Seimsosignal program.	101
Figure 5.59: Displacement of field numerical model in X direction (m), when accelartion is applied in X-direction ($H=12m$)	102
Figure 5.60: Shear strain obtained for $H=12m$ under Northridge earthquake	103
Figure 5.61: r_u generation at $H=12m$ under Northridge Earthquake.	104
Figure 5.62: r_u generation at $H=9m$ under Northridge Earthquake.	104
Figure 5.63: r_u generation at $H=6m$ under Northridge Earthquake.	105
Figure 5.64: r_u deneration at $H=3m$ under Northridge Earthquake.	105
Figure 5.65: Pore pressure ratio for sand with $D_r=40\%$ and $S=80\%$ at $H=12m$.	106
Figure 5.66: Pore pressure ratio for sand with $D_r=40\%$ and $S=80\%$ at $H=9m$.	106
Figure 5.67: Pore pressure ratio for sand with $D_r=40\%$ and $S=80\%$ at $H=6m$.	107
Figure 5.68: Pore pressure ratio for sand with $D_r=40\%$ and $S=80\%$ at $H=3m$.	107

NUMERICAL MODELLING OF SAND BEHAVIOR UNDER CYCLIC SIMPLE SHEAR TESTS IN A SPECIAL LIQUEFACTION BOX

SUMMARY

Liquefaction is one of the most catastrophic effects of earthquakes to the built environment. Liquefaction causes decrement of shear strength in fully saturated loose sands due to excess pore water pressure increment during a repeated loading or dynamic excitation, such as an earthquake. The devastating results of liquefaction can be listed as bearing capacity failures, lateral spreading, differential settlements, etc. In order to reduce liquefaction related failures, some mitigation techniques are implemented in practice. Induced-Partial Saturation (IPS) which has been recently proposed by Yegian et al.(2007) and Eseller-Bayat (2009) is a technique to mitigate liquefaction by generating air/gas in fully saturated liquefiable sand sites. An experimental study was performed to investigate excess pore water generations in partially saturated sands, that were tested in cyclic simple shear liquefaction box (CSSLB) by Eseller-Bayat (2009). This thesis study includes the initial tasks of a TUBİTAK funded project (No: 213M367) with a title "Dynamic Response of Sands Mitigated by IPS (Induced Partial Saturation) under New and Existing Structures". The primary goal of this project is to numerically model partially saturated sands and determine how much partial saturation should be induced in liquefiable areas and how accurate the RuPSS (excess pore water pressure ratio in partially saturated sands) empirical model predicts the liquefaction response of remediated sites by IPS. First, the shaking table tests and the CSSLB box setup are numerically modeled in FLAC^{3D}. Fully saturated sand specimens are tested under cyclic simple shear conditions at a range of relative densities (D_r) and shear strain amplitudes (γ) and compared with the shaking table test results from excess pore water pressure ratio (r_u) and number of cycles to liquefaction (N_L) point of view. More numerical data are obtained for high effective stresses that could not be achieved under shaking table tests due to the limitations of the CSSLB setup. A formulation for N_L is developed as a function of relative density (D_r), simple shear strain amplitude (γ) and initial effective stress (σ'_{v0}). Then, partially saturated specimens are modeled in FLAC^{3D}, by changing the bulk modulus of air-water mixture based on Koning (1963) equation and are compared with the shaking table test results in terms of maximum excess pore water pressure ratio ($r_{u\max}$) and number of cycles to $r_{u\max}$ (N_{\max}). It is concluded that the $r_{u\max}$ values obtained in numerical model analysis are lower for high degrees of saturation (S) and higher for lower degrees of saturation than experimental results. Also, N_{\max} values are achieved higher in numerical analysis results. Future research is needed for modelling the bulk modulus of air-water mixture for numerical modeling.

A procedure is suggested in this study for determining the initiation of liquefaction by using N_L formulation developed and equivalent number of earthquake cycles N_γ . If $N_\gamma / N_L \geq 1$ liquefaction initiates in that sand layer. The procedure is confirmed with the results of a free-field 15 m sand layer numerical model tested under an earthquake record with magnitude M . RuPSS model prediction is also compared with the free-field 15 m partially sand layer results. The excess pore water pressure ratio r_u reached $r_{u\max}$ in both results, however the RuPSS model predicted the $r_{u\max}$ values higher than the numerical model results. Finally, important issues in numerical modeling of

experimental and free-field fully and partially saturated sands for dynamic and liquefaction conditions in FLAC^{3D} are presented in this study.

ÖZEL SIVILAŞMA DÜZENEGİ İÇİNDE ÇEVİRİMSSEL BASİT KESME DENEYLERİ ALTINDA KUM DAVRANIŞININ SAYISAL MODELLENMESİ

ÖZET

Sıvılaşma sıklıkla gevşek suya doymun kumlu topraklarda görülen depremin çevremize ve yapılarımıza yaptığı yıkıcı etkilerinden biridir. Sıvılaşma deprem anında doymun gevşek kumlarda görülen ve boşluk suyu basıncının artması ile büyük deformasyonlara neden olan yıkıcı bir olaydır. Boşluk suyu basıncındaki artışın (Δu) düşey efektif gerilmeye (σ'_{v0}) eşit olma durumunda zemin dayanımını kaybeder ve sıvı faza geçer. Sıvılaşmanın neden olduğu hasarlar, taşıma gücü kayıpları, yanal yayılma ve farklı oturmalarla sonuçlanabilir. Sıvılaşmanın yıkıcı etkisini yok etmek adına, günümüzde çeşitli zemin iyileştirme yöntemleri geliştirilmiştir.

Bu tekniklere ek olarak, sıvılaşma etkisini engellemek adına diğerlerinden daha pratik ve ekonomik olması avantajıyla Kısmi-Doymuna İndirgeme (IPS) yeni bir yöntem olarak Yegian vd. (2007) ve Eseller-Bayat (2009) tarafından geliştirilmiştir. Bu yöntemin konsepti kumun boşluklarında gaz kabarcıkları üreterek kum zeminlerin doymunluk derecesini azaltmaktır. Bu tez çalışması TÜBİTAK destekli 213M367 proje numaralı "Deprem Anında Sıvılaşmayı Engellemek Amacıyla Önerilen "Kısmi-Doymuna İndirgeme (IPS)" Yöntemiyle İyileştirilmiş Zeminlerinin Mevcut veya Yeni Yapılar Altında Dinamik Davranışı" başlıklı proje çalışmasının ilk aşamalarını kapsamaktadır. Önerilen proje yeni bir zemin iyileştirme metodu olan "Kısmi Doymuna İndirgeme (IPS)" tekniğinin gerçek zemin koşullarında uygulandığında hem serbest zeminde hem de yapı-zemin etkileşimi ile oluşacak aşırı boşluk suyu basıncı ve oturmaları tahmin etmeyi amaçlayan bir modelin oluşturulmasını planlamaktadır. Aynı zamanda IPS saha uygulamasında spesifik bir bölgede sıvılaşma kaynaklı hasarı minimize etmek için sağlanması gereken kısmi doymunluk derecesini de bu modelle belirlemeyi amaçlanmaktadır. Bu kapsamda ilk olarak, sarsma tablası deneyleri ve özel sıvılaşma deney düzenegi (CSSLB, çevrimsel basit kesme sıvılaşma deney düzenegi) FLAC 3D sayısal analiz programında modellenmiştir. Suya tam doymun kum numuneleri bir dizi relatif sıklık (D_r) değerlerinde ve farklı kesme birim deformasyon büyüklükleri (γ) altında çevrimsel basit kesme birim deformasyonlarında sayısal olarak test edilmiş ve sarsma tablası deney sonuçları ile aşırı boşluk suyu basıncı (r_u) ve sıvılaşma için gerekli çevrim sayısı (N_L) değerleri cinsinden kıyaslanmıştır. Yüksek efektif gerilmeler için CSSLB deney düzeneginin sınırlandırmalarından dolayı elde edilemeyen çıktılar sayısal analizle elde edilmiştir. Tam doymun kumlarda yapılan basit kesme sayısal analiz sonuçlarına ve sarsma tablası deney sonuçlarına göre düşük ve yüksek efektif gerilmelerde elde edilen sıvılaşma için gereken çevrim sayısı N_L için relatif sıklık (D_r), kesme birim deformasyon büyüklüğü (γ) ve başlangıç efektif gerilme (σ'_{v0})'ye bağlı olarak bir formülasyon geliştirilmiştir. Kısmi doymun kum numuneleri boşluklardaki su-hava karışımının hacim modülü ya da sıkışabilirliğini doymunluk derecesine göre tahmin eden Koning (1963) denklemi kullanılarak FLAC^{3D} yazılımında modellenmiş ve sonuçlar sarsma tablası deney sonuçları ile maksimum boşluk suyu basınç oranı (r_{umax}) (zeminin çevrim sayısı devam edildiği sürece erişebileceği ve orda sabit kalacağı maksimum değer) ve r_{umax} 'e ulaşmak için gereken çevrim sayısı (N_{max}) cinsinden karşılaştırılmıştır. Sayısal

analizlerde elde edilen r_{umax} deęerleri deneysel sonulardan yksek doęunluk derecelerinde daha dřk, dřk doęunluk derecelerinde daha yksek, N_{max} deęerleri ise deneysel sonulardan daha fazla elde edilmiřtir. Kısmi doęun kumların modellenmesinde Koning denkleminin yetersiz kaldıęı ve hava-su karıřımının hacim modl veya sıkıřabilirlięi iin yeni bir formlasyonun gelecek arařtırmalarda geliřtirilmesi gerektięi sonucu ıkarılmıřtır.

Bu alıřmada ayrıca, sıvılařmanın olup olmadıęını tahmin edebilecek pratikte kullanılabilecek bir basit metod geliřtirilmiřtir. M řiddetindeki bir depreme eřdeęer evrim sayısı N_γ ve bu alıřmada geliřtirilen N_L deęerleri kullanılarak, $N_\gamma / N_L \geq 1$ olduęu durumda sıvılařmanın gerekleřtięi tahmin edilebilmektedir. Suyu tam doęun 15 m derinlięinde serbest saha kum modeli zerinde yapılan M řiddetindeki bir deprem altında yapılan sıvılařma analizleri ile bu metod doęrulanmıřtır. N_L deęerinin belirlenebilmesi iin kum tabakasından deprem kaynaklı oluřan birim kesme deformasyon kayıdının yer tepki analizleri ile belirlenmesi gerekmektedir. (ProSHAKE, EERA gibi programlar kullanılabilir.) Suyu kısmi doęun 15 m derinlięindeki serbest saha kum modeli zerinde M řiddetindeki bir deprem altında yapılan sıvılařma analizleri sonuları, RuPSS (kısmi doęun kumlarda bořluk suyu basıncı oranı) ampirik tahmin modeli sonuları ile kıyaslanmıřtır. Sayısal sonularda da ve RuPSS tahmin sonularında da r_u , r_{umax} deęerlerine ulařmıřtır ancak RuPSS modeli r_{umax} deęerlerini daha byk tahmin etmiřtir.

FLAC^{3D} programında dinamik ve sıvılařma modellemelerinde hem deneysel hem de serbest saha modellemelerinde dikkat edilmesi gereken nemli husular bu alıřmada sunulmuřtur.

1. INTRODUCTION

Seismic liquefaction occurs in saturated loose sandy soil when pore water pressure rises during shaking and effective stress decreases. In the extreme case, the effective stress reaches zero. Effective stress expresses the contact force at grain-to-grain contacts in sand so zero effective stress suggests that there is no effective contact between grains. In zero effective stress grains are actually floating in pore water without constraint from surrounding sand particles. Behavior of sand becomes similar the mud water. After complete loss of effective stress, sand has no shear modulus and no shear strength, and consequently develops large deformation even under small shear stress. Since effective stress disappears in sandy ground after liquefaction, bearing capacity disappears and consequently large settlements occurs in foundation of surface structures. Before the 1964, liquefaction was not considered seriously by engineers. In early days, collapse of buildings and failure of slopes were considered more, because those conventional types of seismic damage caused more human casualties.

Different methods are used to decrease the hazard of liquefaction. Relocating or abandoning the structure, structural solutions of improving soil by using pile beneath building and other structural systems that decrease the damage, controlling the undesirable pore-water pressure by using relief wells and drain systems and improving the sand of the site are some of these methods. Important factors for choosing the best method are economical parameters and practicality of the method. By considering these parameters, soil improvement and pore pressure controlling are most popular mitigating methods.

Yegian et al (2007) and Eseller-Bayat (2009) explored to use induced partial saturation (IPS) as technique to mitigate liquefaction risk. The concept of this technique is to reduce degree of saturation of sand by entrapping gas bubbles in sand skeleton. With experimental tests, it was observed that with small reduction in degree of saturation, possibility of liquefaction decreases effectively and air entrapped specimens never liquefied. Sustainability of entrapped air was also checked by Eseller (2007) and results were satisfactory. Before using the IPS method in the field, deep investigation

is necessary. For this purpose it was required to estimate the IPS behavior under different cyclic loading analytically. Analytical correlation for partially saturated sand was investigated by many researchers.((R Chaney, 1978), (Yang, J., Savidis, S., Sato, T., Li, 2003), (Ishihara, K.& Tsukamoto, 2004),(Okamura, M., Ishihara, M., Tamura, 2006)). Most of these correlations were done for partially saturated sand with degree of saturation greater than 95%. Eseller-Bayat (2009) performed a series of cyclic simple shear strain tests on partially saturated sand specimens and investigated the effect of the fundamental parameters (S , D_r , γ , M , σ_v') on maximum pore water pressure ratio ($r_{u\max}$) generated in partially saturated sands regardless of the number of cycles applied. Eseller-Bayat (2009) used an experimental setup called CSSLB to test partially saturated sands at lower degrees of saturation under cyclic simple shear conditions on a shaking table and developed an empirical model to predict excess pore water pressure ratio r_u in partially saturated sands under an earthquake with a magnitude M .

This thesis study includes the initial research tasks of a TÜBİTAK funded project (No: 213M367) titled "Dynamic Response of Sands Mitigated by IPS (Induced Partial Saturation) under New and Existing Structures". The primary goal of this project is to numerically model partially saturated sands and determine how much partial saturation should be induced in liquefiable areas and how accurate the RuPSS (excess pore water pressure ratio in partially saturated sands) empirical model predicts the liquefaction response of remediated sites by IPS. The main goals of this study can be listed as below:

- To numerically model the CSSLB (Cyclic simple shear liquefaction box) setup and to perform dynamic and liquefaction analysis on fully and partially saturated sand specimens modeled in CSSLB in FLAC^{3D} (Fast Lagrangian Analysis of Continua in 3 dimensions).
- After confirming the proper numerical model of CSSLB and shaking table tests on fully saturated sands, another goal of this study is to and to compare with the shaking tables test results.

- To obtain liquefaction analysis results in fully and partially saturated sand specimens at high effective stresses, that couldn't be achieved experimentally due to the limitations of CSSLB.
- To develop a formulation for N_L (number of cycles to reach liquefaction) for sands as a function of relative density (D_r), simple shear strain amplitude (γ) and initial effective stress (σ'_{v0}). This formulation aims to predict the initiation of liquefaction in free-field sand layers under an earthquake with a magnitude M .
- To eventually check the RuPSS model prediction by comparing with the numerical results for a free-field partially saturated sand layer.

This research contains five chapters. Chapter 2 presents literature review on liquefaction evaluation approaches, liquefaction-induced deformations, liquefaction mitigation methods emphasized on IPS. Shaking table experimental setup and empirical model RuPSS model developed by Eseller-Bayat (2009) are also mentioned in this section.

Chapter 3 presents an introduction of numerical modelling in $FLAC^{3D}$ emphasized on geotechnical dynamic and liquefaction analysis. In this chapter, constitutive models used for numerical modelling are presented briefly. Also uncoupled liquefaction model used for liquefaction numerical modelling (Finn Model) is mentioned in this section.

Chapter 4 includes the numerical modeling steps of CSSLB and fully and partially saturated sands in $FLAC^{3D}$ program. Dynamic analysis and liquefaction analysis were performed at a range of relative densities, shear strain amplitudes and degree of saturation. Modeling the different components of the CSSLB is represented here. Also properties of material used for numerical modeling are all stated.

Chapter 5 presents the results of the numerical modeling analysis. In this section simple shear strain condition is first proven confirming proper modeling of the CSSLB test setup. Comparison between experimental and numerical modeling test results for fully saturated sand specimens is presented. Also results of the numerical model under higher effective stress is discussed in this part. The N_L formulation is developed and the procedure to predict the initiation of liquefaction using the N_L formulation is presented and confirmed with liquefaction analysis results of a free-field fully

saturated sand layer tested under an earthquake with a magnitude M in $FLAC^{3D}$. Initial attempts are made for modeling the partially saturated sands in $FLAC^{3D}$ and the comparison of RuPSS model prediction results and liquefaction analysis results of partially saturated free-field sand layer modelled in $FLAC^{3D}$ are presented.

2. LITERATURE REVIEW

Liquefaction is the one the most costly phenomenon which happens in the saturated sand deposits. During the cyclic loading the loose sand tends to contract, which causes the normal stress to transfer from the sand particles to the water. The intensification happens when the sand matrix is saturated and drainage is impossible. Some of the most dramatic instances of liquefaction were observed after the 1964 Niigata, Japan earthquake and 1964 Prince William Sound, Alaska earthquake. These two earthquakes helped in the identification of liquefaction. The mechanism of liquefaction for fully saturated sand under cyclic loading was first recognized by Casagrande in 1936. Pore water pressure is the main cause of liquefaction initiation. Without pore pressure generation no liquefaction occurs.

2.1 Liquefaction Evaluation Approaches

Liquefaction is categorized in two different phenomenon which consist of Flow liquefaction and cyclic mobility. Flow liquefaction is phenomenon which initiated by cyclic loading, when shear stress required for static equilibrium is greater than steady state strength (Kramer, 1996). Main factor of these shear stress are gravity. An undrain disturbance is necessary for occurrence of flow liquefaction. Flow liquefaction surface (FLS) is locus of points describing effective stress at initiation of flow liquefaction and it is straight line. If sand initial stress condition is far from FLS it is more resistant against liquefaction. Zones where the flow liquefaction is susceptible is obvious in figure 2.1.

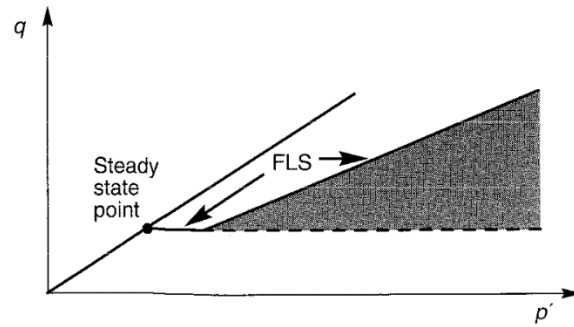


Figure 2.1 : Zones of susceptibility of flow liquefaction (Kramer, 1996).

When shear stress is smaller than steady state shear strength, cyclic mobility can develop. Cyclic mobility can occur in both loose and dense sand. In contrast to flow liquefaction there is no clear point where the cyclic mobility occurs. Zones of susceptibility of cyclic mobility are shown in figure 2.2.

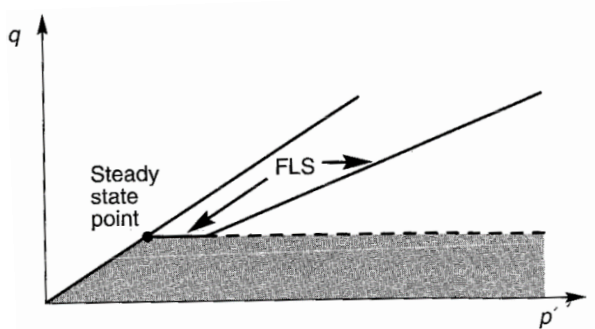


Figure 2.2 : Zones of susceptibility of cyclic mobility (Kramer, 1996).

By considering the steady state and flow liquefaction concept mechanism of liquefaction can be understood. There are some other approaches to evaluate the potential of liquefaction. Main approaches which are preferred by engineers are cyclic stress approach and cyclic strain approach. In the following part, these two methods are going to be discussed.

2.2 Cyclic Stress Liquefaction Evaluation Approach

Studies of H.B. Seed at Berkley University consider evaluation of the loading condition required to triggering liquefaction. Loading in Seed's studies describe cyclic shear stress. Also liquefaction potential is evaluated on the basis of amplitude and number of cycles of earthquake which induced shear stress. This approach is named

cyclic stress approach. Initial liquefaction is defined as the point where the increment of pore pressure is equal to initial effective confining pressure(Seed, 1966).

Concept of cyclic stress approach is: earthquake induced loading which is expressed in terms of cyclic simple shear stress is compared with liquefaction resistance of sand which is also in terms of simple shear stress. When the loading exceeds the resistance, liquefaction is expected to occur. For using the cyclic stress approach it is necessary to characterize loading conditions and liquefaction resistance. Loading can be studied in two ways: by detailed ground response or by use of simplified approaches. Ground response analysis characteristics of actual earthquake motion, on the other hand laboratory data for liquefaction consider uniform amplitudes. Seed et al (1975) innovate a weighting procedure to convert shear stress time histories from records of ground motion to shear stress of uniform cycles that is shown in equation 2.1 (Seed, H.B, Idriss I.M, Lee K, 1975)

$$\tau_{cyc} = 0.65\tau_{max} \quad (2.1)$$

where τ_{cyc} is amplitude of uniform shear stress, τ_{max} is Maximum shear stress of ground motion. Seed and Idriss (1971) also calculate uniform cyclic shear stress amplitude for surface sites or gently sloping sites by equation 2.2

$$\tau_{cyc} = 0.65 \frac{a_{max}}{g} \sigma_v r_d \quad (2.2)$$

where a_{max} is peak ground surface acceleration, g is acceleration of gravity, σ_v total vertical stress, r_d is a factor which consider stress reduction at depth.

Characterization of liquefaction resistance developed with two methods. Methods based on results of laboratory tests and methods based on observation of liquefaction behavior.

2.2.1 Characterization of liquefaction resistance based on laboratory test

The early development of cyclic stress approach emphasized on laboratory testing for characterization of liquefaction resistance. Most of these laboratory tests performed on isotopically consolidated triaxial specimen or simple shear specimens. In these tests liquefaction failure is defined as point at which initial liquefaction was reached. In

some other tests liquefaction is defined where limiting cyclic strain amplitude (commonly 5% for dense specimens) was reached.

Laboratory tests show that number of loading cycles required to produce liquefaction failure (N_L), decreases by increasing shear stress amplitude and it increases by increasing density. While liquefaction can occur in few cycles in loose specimen subjected by large cyclic shear stress, thousands cycles of low amplitude shear stress is necessary to cause liquefaction in dense specimen.

Cyclic stress curves can be normalized by initial effective stress and produces cyclic stress ratio (CSR). For different experimental setups CSR should be calculated differently. Earthquake produces shear stress in different directions. Multi directional shaking makes the pore pressure generation rapidly. Seed et al (1975) suggested that CSR required to produce initial liquefaction in field is 10% less than that required in unidirectional simple shear tests which is mentioned in equation 2.3

$$(CSR)_{field} = 0.9(CSR)_{ss} \quad (2.3)$$

where $(CSR)_{field}$ is field cyclic stress ratio, $(CSR)_{ss}$ is simple shear test cyclic stress ratio.

Laboratory tests can also expose the manner where excess pore pressure is generated. For stress controlled uniform loading, it was found that pore pressure ratio r_u , is related to number of loading cycles by equation 2.4

$$r_u = \frac{1}{2} + \frac{1}{\pi} \sin^{-1} \left[2 \left(\frac{N}{N_L} \right)^{\frac{1}{\alpha}} - 1 \right] \quad (2.4)$$

where N_L is the number of cycles required to produce initial liquefaction and α is function of sand properties under test conditions (Lee K.L and Albaisa, 1974) and (De Alba, P and Pyke, 1987). Equation 2.4 is obvious in Figure 2.3 as a dashed line when $\alpha=0.7$. Figure 2.3 shows rate of pore pressure generation in cyclic simple shear tests.

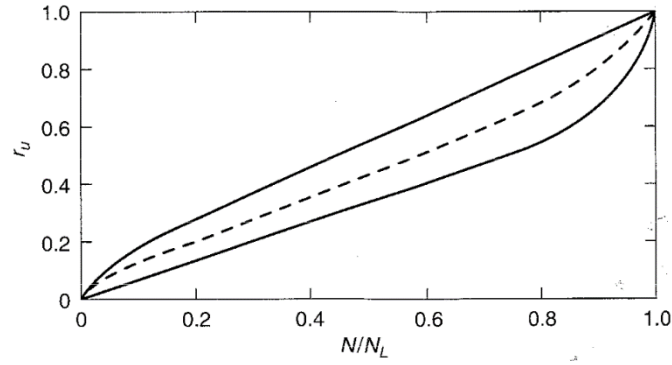


Figure 2.3 : Rate of pore pressure generation in cyclic shear test(De Alba, P and Pyke, 1987).

The CSR that is required to reach liquefaction in a specified number of loading cycles (N) may also be called sand's cyclic resistance ratio (CRR). The relationship between CRR and N can generally be approximated with the power function as it is shown in equation 2.5

$$CRR = a \cdot N^{-b} \quad (2.5)$$

where the parameters a and b are determined by regression against the experimental data.

2.2.2 Characterization of liquefaction resistance based on in situ tests

An alternative approach to use liquefaction case histories to characterized liquefaction resistance by using in situ test parameters was described(Whitman, 1971). Previous case histories characterized by combination of loading parameters and liquefaction resistance parameters. Cyclic stress ratio is used as loading parameter and density and pore pressure generation are used as liquefaction resistance. A boundary usually was drawn conservatively that all the cases which liquefaction has been observed lie above. There are different methods for analyzing liquefaction resistance in situ. Some of these methods are going to discuss briefly in this part.

Standard Penetration Resistance: Standard penetration test (SPT) is one the most common field tests. Factors which increase the SPT resistance also tend to increase the liquefaction resistance. By considering this fact, SPT test can be helpful in liquefaction resistance calculation. SPT is the most commonly used method in situ method for liquefaction.

Cone Penetration Resistance: Cone penetration test (CPT) can also be used to measure liquefaction resistance. CPT has an advantage over SPT in its ability to detect thin seams of loose sand.

Shear wave velocity: Shear wave velocity can be useful in studying and measuring liquefaction resistance. Some observation show that shear wave velocity of sand do not consider all the effective factors such as sand fabrics, over consolidation ratio and prior cycling straining. Shear wave velocity measurement may not be sufficient to evaluate the liquefaction potential of all sand deposits.

2.2.3 Evaluation of initial liquefaction

After characterizing the liquefaction resistance, liquefaction potential can be evaluated. Cyclic stress approach considers the earthquake loading by equivalent uniform cyclic stress and liquefaction resistance by uniform cyclic stress required to produce liquefaction in the same number of cycles. Factor of safety which is expressed in equation 2.6 is smaller than one when liquefaction happens

$$FS = \frac{\tau_{cyc,L}}{\tau_{cyc}} \quad (2.6)$$

where $\tau_{cyc,L}$ is cyclic shear stress required to cause liquefaction, τ_{cyc} is equivalent cyclic shear stress induced by earthquake.

Evaluation of initial liquefaction can also be done graphically. First equivalent cyclic shear stress in depth is plotted. Then variation of cyclic shear stress required to cause liquefaction is plotted in the same graph by depth. Liquefaction is expected at depth where equivalent cyclic shear stress in depth exceeds the resistance which is shown in figure 2.4.

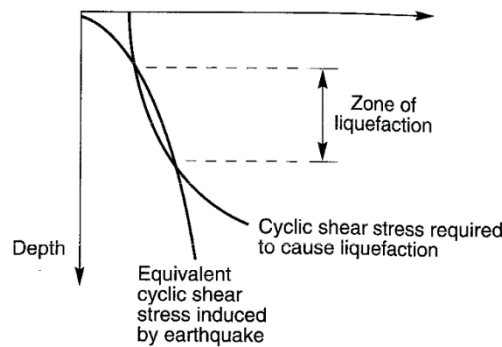


Figure 2.4 : Zones of liquefaction is identified (Kramer, 1996).

Sometimes significant excess pore pressure may develop even if the computed factor of safety is greater than one. Magnitude of this excess pore pressure at level ground sites can be estimated from figure 2.5

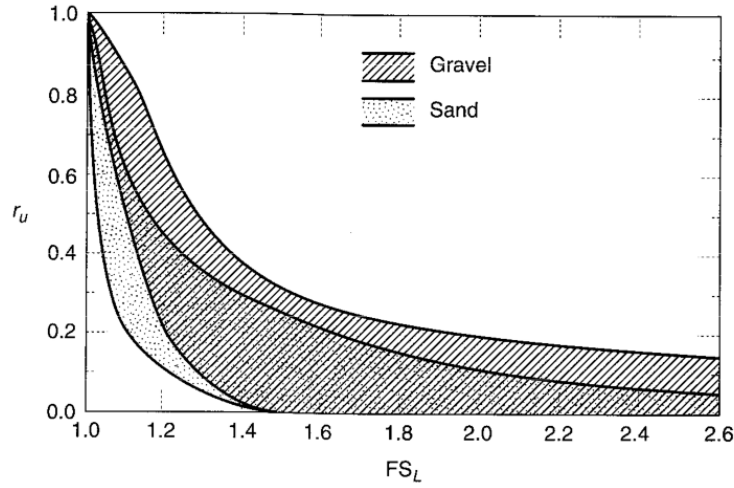


Figure 2.5 : Relationship between residual excess pore pressure and factor of safety against liquefaction for level ground sites(Marcuson, William F., III, Hynes,M.E and Franklin, 1990).

The overburden correction factor (K_σ) was introduced by Seed (1983) to adjust the CSR or CRR to a common value of effective overburden stress, because these two parameters depends on effective overburden stress. Definition of K_σ is mentioned in equation 2.7

$$K_\sigma = \frac{CRR_{\sigma'_{vc}}}{CRR_{\sigma'_{vc}=1}} \quad (2.7)$$

where $CRR_{\sigma'_{vc}}$ is the CRR of a soil under specific value of σ'_{vc} and $CRR_{\sigma'_{vc}=1}$ is the CRR of the same soil when $\sigma'_{vc} = 1$ atm. Most K_σ is derived from laboratory test results as described by Harder and Boulanger (1997) or by theoretical considerations as described by Hynes and Olsen (1998), Boulanger (2003) or by regression against field case histories that was introduced by Cetin et al (2004).

2.3 Cyclic Strain Liquefaction Evaluation Approach

Dobry and Ladd (1980) and Dobry et al (1982) described an approach that used cyclic strain rather than cyclic stress to characterized earthquake induced loading and liquefaction resistance. Seed and Silver (1971) and Youd (1972) investigation show

that densification of dry sand is controlled by cyclic strain rather than cyclic stress. This conclusion is base of cyclic strain approach.

2.3.1 Characterization of loading conditions

In the cyclic strain approach earthquake induced loading is expressed in terms of cyclic strain. As it was mentioned in previous part, time history of a real earthquake is irregular. To compare the loading with laboratory liquefaction resistance it is necessary to convert shear strain induced by real earthquake to uniform cyclic strain of laboratory tests. A simplified method for estimating the amplitude of uniform cyclic strain from the amplitude of uniform cyclic stress which is calculated by equation 2.2 was proposed in equation 2.8 (Dobry, R.Ladd, R.S , Yokel, F.Y., Chung , R.M AND Poweel, 1982)

$$\gamma_{cyc} = 0.65 \frac{a_{max}}{g} \frac{\sigma_v r_d}{G(\gamma_{cyc})} \quad (2.8)$$

where a_{max} is peak ground surface acceleration, g is acceleration of gravity, σ_v total vertical stress, r_d is a factor which consider stress reduction at depth and $G(\gamma_{cyc})$ is shear modulus of soil when $\gamma = \gamma_{cyc}$.

γ_{cyc} is mentioned at both sides of the equation so value of $G(\gamma_{cyc})$ should be calculated iteratively from measured G_{max} profile and appropriate modulus reduction curves. Once γ_{cyc} is determined it can be compared with threshold shear strain (γ_t). If $\gamma_{cyc} < \gamma_t$ liquefaction cannot be initiated.

2.3.2 Characterization of liquefaction resistance

Characterization of liquefaction resistance from laboratory tests is simpler in cyclic strain approach because factors that increase cyclic stress required to initiate liquefaction, (density, sand fabric, over consolidation ratio) also increase shear modulus of sand. By considering this relation $\gamma_{cyc} = \tau_{cyc}/G$ these parameters have small influence on pore pressure generation when interpreted in terms of cyclic strain. Dobry and Ladd (1980) investigation shows that generated pore pressure is insensitive to the factors other than cyclic strain amplitude.

2.3.3 Evaluation of liquefaction potential

Evaluation of liquefaction potential in cyclic strain approach is similar that used in cyclic stress approach. Cycling loading imposed by earthquake, characterized by the amplitude of a series of equivalent number of cycles in uniform strain cycles, is compared with liquefaction resistance, which is expressed in terms of cyclic strain amplitude required to initiate liquefaction in the same number of cycles. There is no factor of safety in cyclic strain approach, because loading and resistance are characterized in terms of strain.

The main advantage of cyclic strain approach is strong relation between pore pressure generation and cyclic strain amplitude. Excess pore pressure can be calculated more accurately in cyclic strain approach than cyclic stress approach.

2.4 Other Liquefaction Evaluation Approaches

Some other approaches also has been developed beside the cyclic stress and cyclic strain approaches. As additional data are become available for calibration of these approaches, they use become more likely. Three of these approaches are going to be stated briefly in this part.

Energy dissipation approach: this approach consider both cyclic stresses and cyclic strains. Densification of dry sand cause rearrangement of grains and use of energy. Dry sand under cyclically loading densifies and amount of energy required rearranging sand particles increases. In the saturated sand tendency to densification cause pore pressure to increase and contact forces to decrease. By decreasing the contact force between the particles amount of energy needed to rearrange sand grains decreases.

Effective stress base response analysis approach: Stress-strain modeling of sand behavior was considered as a subject of intense for many years. Cyclic nonlinear stress strain models use an empirical backbone curve and series of unloading-reloading curves that manage cyclic behavior. Numbers of models was generated to predict pore pressure generation. Martin et al 1975, Ishihara and Towhata 1980 and Finn and Bhaitea 1981 predict generation of pore pressure under irregular cyclic loading conditions. In Martin's model pore pressure generated in an increment of undrained loading is related volumetric strain that would have occurred in the same loading under drained condition by equation 2.9

$$\Delta u = E_r \cdot \Delta \varepsilon_{vd} \quad (2.9)$$

where E_r is rebound modulus and $\Delta \varepsilon_{vd}$ is incremental volumetric strain under drained condition. The rebound modulus is expressed with equation 2.10

$$E_r = \frac{(\sigma'_v)^{1-m}}{mk_2(\sigma'_{v0})^{n-m}} \quad (2.10)$$

where σ'_v and σ'_{v0} are current initial vertical effective stress and m , n and k_2 are parameters which calculated experimentally. Increment of volumetric strain is going to be calculated with equations 2.11

$$\Delta \varepsilon_{vd} = C_1(\gamma - C_2 \varepsilon_{vd}) + \frac{C_3 \varepsilon_{vd}^2}{\gamma + C_4 \varepsilon_{vd}} \quad (2.11)$$

where γ is cyclic shear strain and ε_{vd} is cyclic volumetric strain. $C_1 - C_4$ are constant determined from experimental setups (Martin, Seed, & Finn, 1975a). Further, simpler equation (2.12) was generated where the constant values could be calculated from the material properties and not only from experimental setups by Byrne 1991

$$\frac{\Delta \varepsilon_{vd}}{\gamma} = C_1^C \exp(-C_2^C \left(\frac{\varepsilon_{vd}}{\gamma}\right)) \quad (2.12)$$

Where C_1^C and C_2^C are constants which relates to relative density (D_r)(Byrne, 1991).

Probabilistic approach: there are lots of uncertainty in loading and resistance aspects of liquefaction. Uncertainties can be considered by using standard probabilistic approaches that has been developed to deal with them. In past 30 years, probabilistic concepts were used to consider uncertainties in size, location and rate of recurrence of earthquake in evaluation of seismic hazards. Probabilistic seismic hazard analysis (PSHA) provides framework that can identify these uncertainties.

Uncertainties in liquefaction resistance can be considered in two ways. First group of methods are based on probabilistic characterization of the parameters shown by laboratory tests which are effective in pore pressure generation. Second group of methods are based on in situ based characterization of liquefaction resistance. These methods use various statistical classification and regression analyses to assign

probabilities of liquefaction to different combination of loading and resistance parameters.

2.5 Liquefaction Induced Deformations

Liquefaction has catastrophic effects on buildings, bridges, buried pipelines and other structure facilities in many different ways. Effects of liquefaction can be understand well by studying the case histories. Increasing the positive excess pore pressure causes sand stiffness to decrease during earthquake. Very stiff liquefiable sand deposit at the beginning of earthquake may be come a softer sand.

2.5.1 Sand boils

Liquefaction is sometimes coupled with sand boils. During or after earthquake shaking, excess pore pressure dissipates by upward flow of pore water. When the hydraulic gradient reaches to critical value vertical effective stress will reach to zero. In this case water velocity will be sufficient to carry sand particles to the surface. Sometimes force can be loosen the upper portion of the deposits and leave it in a situation that is susceptible to liquefaction in future earthquake(Youd, 1984). It should be considered that development of sand boil is hard. It depends on magnitude of excess pore pressure, thickness, density, permeability, and other parameters.

2.5.2 Settlement

Tendency of sand to densify under earthquake shaking loading is well known fact. Dry sand densifies very quickly. Settlement of saturated sand deposits requires more time. Settlement of saturated sand can occur only when induced pore pressure dissipates. Time required for this settlement depends on permeability and compressibility of sand. Estimation of earthquake induced settlement of sand is difficult. Settlement error is large value even for static settlement prediction. It will be more complicated for seismic loading. But there are some procedures that produce the results which that agree with observed field behavior.

2.5.2.1 Settlement of dry sand

Densification of dry sand subjected earthquake, depends on density of the sand, amplitude of the cyclic shear strain in the sand and number of cycles(Seed, H.B and Idriss, 1971). Settlement can be estimated by using detailed ground response analysis

or simplified procedure. Simplified procedure uses effective cyclic shear strain which is mentioned in previous part as equation 2.8(Tokimatsu, K and Seed, 1987).

γ_{cyc} can be estimated when G_{max} is known by using diagrams that are prepared by Tokimatsu and Seed (1987). Effective cyclic shear strain can be used for estimating the volumetric strain by using relative density and SPT resistance with some diagrams which were prepared by Tokimatsu and Seed (1987). By using height of the sand layer and estimating the volumetric strain, settlement can be calculated.

2.5.2.2 Settlement of saturated sands

The post earthquake settlement of sand is influenced by density of sand, maximum shear strain induced in the sand and excess pore pressure generated. Experimental results shows that volumetric strain after initial liquefaction depends on relative density and maximum shear strain. A chart (figure 2.6) was prepared by Tokimatsu and Seed (1987) to allow volumetric strain after liquefaction when magnitude of earthquake is 7.5 to be estimated directly from CSR and SPT resistance.

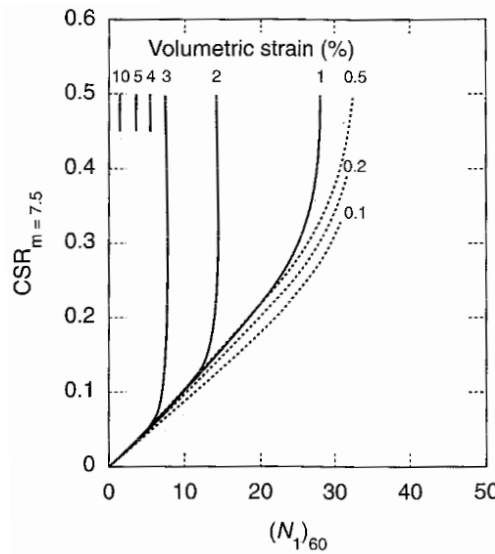


Figure 2.6 : Chart for estimation of volumetric strain in saturated sand from cyclic stress ratio (Tokimatsu, K and Seed, 1987).

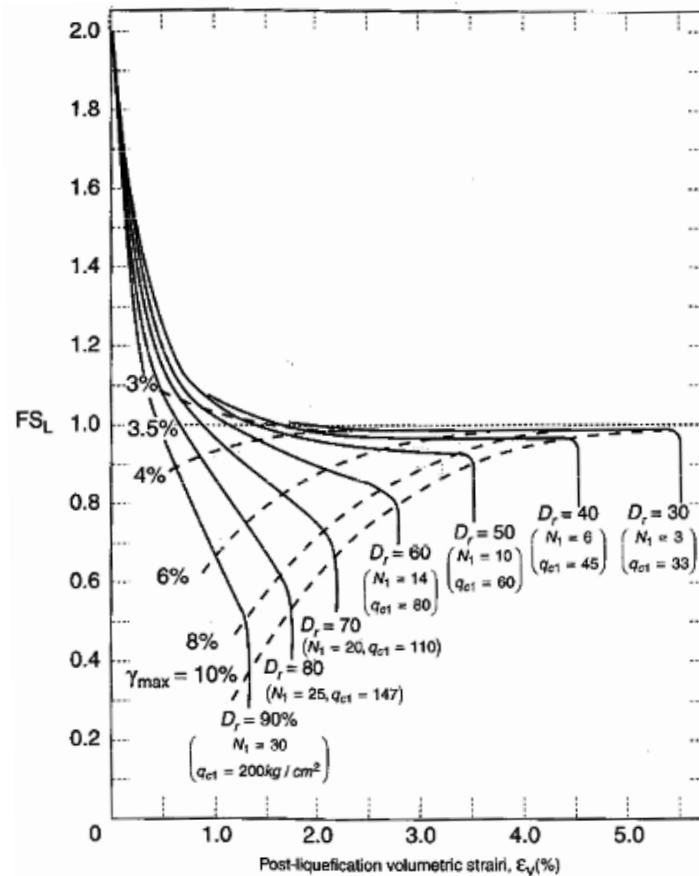


Figure 2.7 : Estimating the post liquefaction volumetric strain of clean sand as function of factor of safety (Ishihara, 1992).

An alternative approach, is used to estimate post liquefaction volumetric strain by factor of safety or maximum cyclic shear strain and relative density, SPT resistance or CPT resistance as it is obvious in figure 2.7. By considering the thickness of sand and volumetric strain settlement can be calculated.

2.6 Liquefaction Mitigation Methods

There are numbers of ways to decrease the hazard of liquefaction. Relocating or abandoning the structure, structural solutions of improving sand by using pile beneath building and other structural systems that decrease the damage, controlling the undesirable pore-water pressure by using relief wells and drain systems and improving the sand of the site are some of these methods. Economical parameters and practicality of the method is focused in choosing liquefaction mitigation techniques.

Improvement of sand and pore-water pressure controlling are most popular ways for decreasing the hazards of liquefaction. Numbers of sand improvement techniques are

available to mitigate sand liquefaction. Mechanism of all these methods is improving the engineering properties of the sand. The most common of these methods can be divided into four major categories: densification techniques, reinforcement techniques, grouting/mixing techniques, and drainage techniques. Each of these methods are going to be discussed briefly.

Densification is one of the most effective and commonly used means of improving sand properties against liquefaction. At the same time, it should be recognized that the increased stiffness of densified sand deposit will cause it to respond differently to earthquake motion. The most common approaches to densification include vibro techniques, dynamic compaction, blasting, and compaction grouting. First three techniques are useful for granular and cohesion less sand to densify when subjected to vibrations.

In some cases it is possible to improve the strength and stiffness of an existing sand deposit by installing discrete inclusions that reinforce the sand. These inclusions may consist of structural materials, such as steel, concrete, or timber and geomaterials such as densified gravel (Kramer, 1996).

The engineering characteristics of many sand deposits can be improved by injecting or mixing cementations materials into the sand. These materials both strengthen the contacts between sand grains and fill the void space between the grains. Grouting techniques involve the injection of cementations materials into the voids of the intact sand. Mixing techniques is implemented by mixing the cementation materials by sand. Mixing technique completely disturb the particle structure of the sand (Kramer, 1996).

Unacceptable movements of slopes, embankments, retaining structures, and foundations can frequently be eliminated by lowering the groundwater. Generation of excess pore water pressure during seismic movement can be reduced by using drainage techniques. (Kramer, 1996). Another approach of decreasing the pore water pressure is inducing air bubbles in water. This method makes the water compressible. Consequent of compressibility of water is decrement in pore water pressure generation.

2.7 New Mitigation Method for Liquefaction (IPS Method)

Eseller-Bayat (2004) and Yegian et al (2007) explored to use induced partial saturation (IPS) as technique to mitigate liquefaction risk. The concept of this technique is to

reduce degree of saturation of sand by entrapping gas bubbles in sand skeleton. With experimental tests, it was observed that with small reduction in degree of saturation, possibility of liquefaction decreases effectively and air entrapped specimens never liquefied. Sustainability of entrapped air was also checked by Eseller-Bayat (2007) and results were satisfactory. By using the results of experimental setup a mathematical model was conducted that was named RuPSS by Eseller-Bayat (2009) for calculating the pore-water pressure ratio (r_u).

2.7.1 Experimental setup of IPS

An experimental research program was conducted to investigate the excess pore water pressure generations in gas-entrapped specimens prepared by IPS and to understand the effect of various parameters on the excess pore water pressures generated in partially saturated sand specimens. Cyclic simple shear strain tests were performed on fully saturated and gas-entrapped specimens prepared in CSSLB. Experimental tests demonstrated that gas/air entrapped within saturated sand remains in the sand even under large horizontal and vertical hydraulic gradients, as well as large horizontal vibrations similar to earthquake ground motions.

According to the cyclic simple shear strain tests, excess pore water pressures generated in partially saturated sands never reaches to the level of initial liquefaction. In other words, maximum excess pore water pressure ratio ($r_{u\max}$) never reaches 1, which is the case in fully saturated sands. Excess pore water pressure generated in a partially saturated sand reaches a maximum value and remains steady under shear strain cycles.

Cyclic Simple Shear Liquefaction Box (CSSLB) was designed and manufactured at Northeastern University to diminish the undesirable effects and limitations of the NUBL and allows testing fully and partially saturated tests specimen under controlled drainage conditions.(Eseller-Bayat, Gokyer, Yegian, Ortakci, & Alshawabkeh, 2013)

After the preliminary design of the cyclic simple shear liquefaction box (CSSLB) was completed, the degree of the boundary disturbance and the homogeneity of the shear strains were investigated by using a computer model(Eseller-Bayat et al., 2013).

For this purpose, two-dimensional computer models of the test setup were generated using finite difference analysis software and the displacement patterns within a sand specimen placed in the CSSLB were investigated by applying forces on the tops of the

rotating sidewalls to cause their rotations. The software that was used for the computer analyses was FLAC 5.0 (Itasca Consulting Group, Inc. 2005) which is a two-dimensional explicit finite difference program for engineering mechanics calculation.

The computer model consisted of elastic grid elements and interface elements. Interface elements are special elements of a grid that are used to simulate distinct planes along which slip and/or separation can occur. Two two-dimensional models were generated for the evaluation of the boundary effects on the displacement patterns within a specimen: 1) A plan view model that represented a horizontal cross section across the CSSLB, and 2) An elevation model that represented a vertical cross section of the CSSLB (Eseller-Bayat et al., 2013).

An initial analysis of the plan view model using average material properties was made and displacements in x direction along three lines within the sand were computed. The grid consists of 23 elements in the x direction and 34 elements in the y direction. Each grid element is 1cm x 1cm in size.

Locations of these lines corresponded to nodes $i = 6, 13,$ and 20 , along $4/21, 11/21,$ and $18/21$ of the total distance within the sand specimen from the left rotating sidewall. As it is obvious in figure 2.8 the results confirm that the two fixed sidewalls have negligible effect on the displacement pattern within the sand specimen.

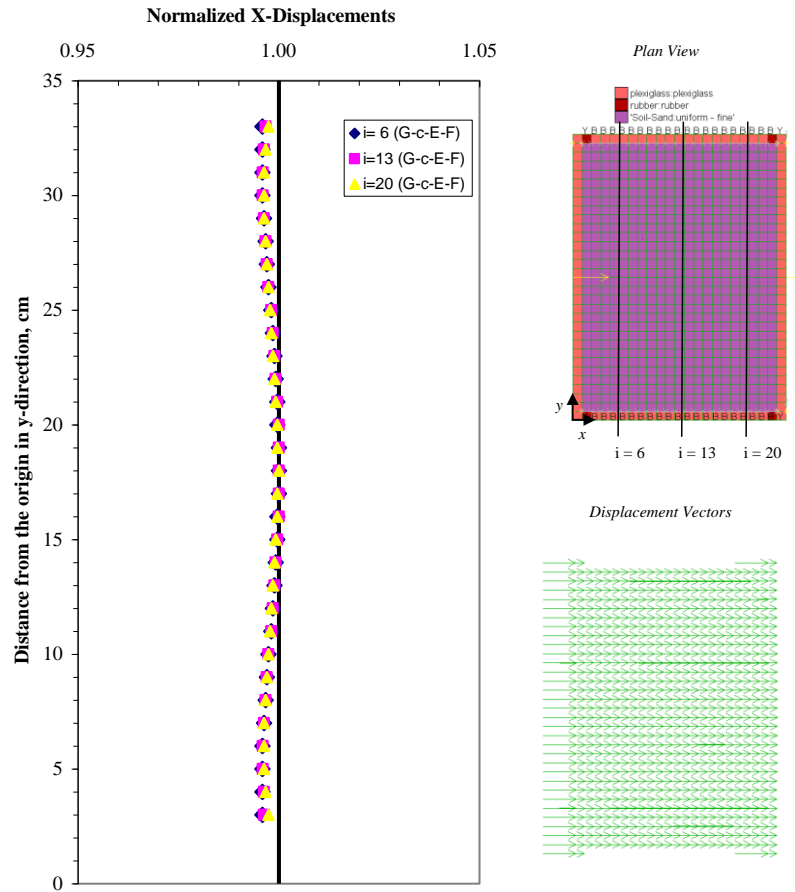


Figure 2.8 : X-Displacements for the Plan View Model Normalized by the X-Displacements of the Mid-Points of Three Lines at $i = 6, 13,$ and 20 (Ortakci,2007).

Then analysis of a vertical cross section through the CSSLB was made to determine the effect of the vertical rotating sidewalls on the displacement patterns. The mesh consists of 25 grid elements in the x direction and 49 grid elements in the y direction. Each grid element is 1cm x 1cm in size.

Displacements, with depth of the sand specimen, were computed and along three vertical lines passing at $4/21, 11/21,$ and $18/21$ of the total distances within the sand specimen, from the left rotating sidewall (nodes $i = 6, 13,$ and 20) were plotted. Figure 2.9 shows the shear strains normalized with the shear strain within the sand element at the top of the specimen. It can be seen from the figure 2.9 that specimen does not have uniform shear strain up to 10 cm from bottom. It is concluded that the CSSLB can induce uniform shear strains extending from 10cm from the base to the top of the specimen.

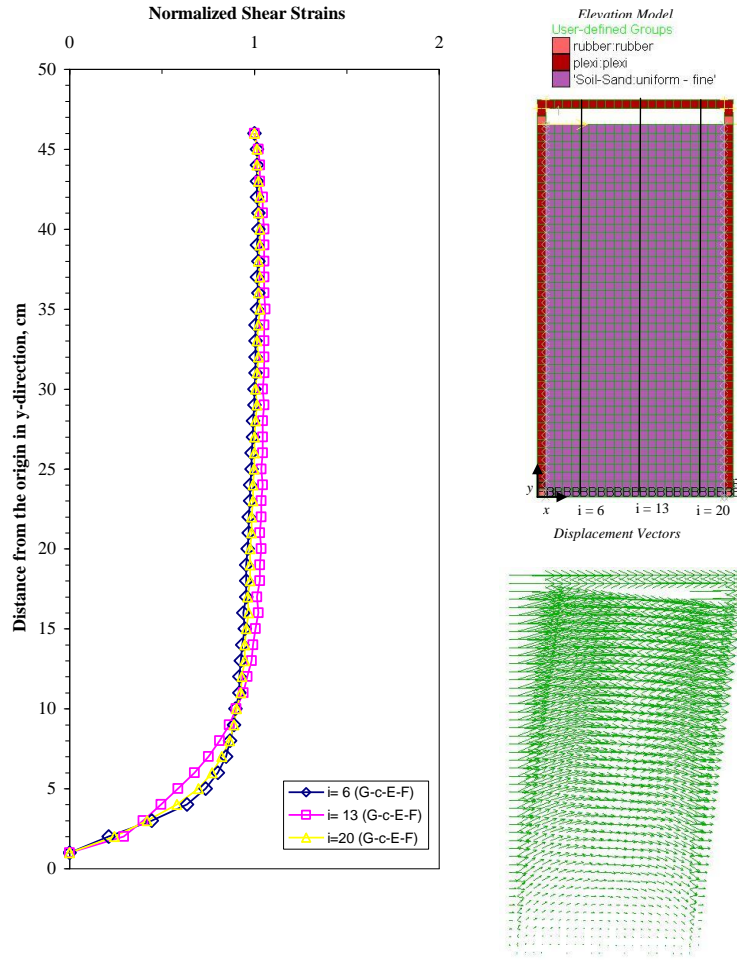


Figure 2.9 : X-Displacements for the Plan View Model Normalized by the X-Displacements of the Mid-Points of Three Lines at $i = 6, 13,$ and 20 (Ortakci,2007).

2.7.2 Mathematical model for prediction of pore water pressure ratio in IPS

A mathematical model was developed to predict excess pore water pressure ratio (r_u) in partially saturated loose to medium dense sands under different earthquake magnitudes and shear strain histories. (Eseller-Bayat, 2009). This model is initial effort based on experimental data that is named RuPSS (r_u for partially saturated sand). Parameters which are effective in prediction of r_u are degree of Saturation in the field (S), relative density of the sand (D_r), maximum shear strain that the sand profile experiences due to a particular earthquake (γ_{max}), magnitude of the earthquake(M) and effective stress (σ'_v).

The model has two stages. In the first stage, a function was developed to estimate the maximum excess pore water pressure ratio ($r_{u_{max}}$). In the second stage, the effect of

earthquake magnitude or number of cycles of strain application was introduced to estimate r_u .

In the first stage, it was observed that maximum excess pore pressure ratio ($r_{u\max}$) that water would experience is related to degree of saturation (S), relative density (D_r) and shear strain amplitude (γ). It was also observed that most dominant parameter for determining the $r_{u\max}$ is degree of saturation S .

A total of 96 tests were performed on partially saturated sand specimens. Initially 24 cyclic shear tests were performed on specimen with degree of saturation ranging from 50% to 90%, relative densities between 20% and 53% and shear strain amplitude of 0.1% and 0.05%. Maximum excess pore pressure ($r_{u\max}$) was first developed for sand with relative density about 20% and shear amplitude equal to 0.1% and it was named f function. The first 24 tests were defined as preliminary tests which led to the development of a preliminary model to predict excess pore water pressure ratio (r_u). The remaining 72 tests were defined as secondary tests which were conducted to improve and validate the preliminary model.

Then scaling factors was used to make relationship between f function and tests results with other relative densities and shear strains, which are named F_D and F_γ for calculating $r_{u\max}$. This procedure is done by equation 2.13 thru 2.16

$$r_{u\max} = f(S, D_r = 20\%, \gamma = 0.1\%) * F_D(S, D_r) * F_\gamma(S, \gamma) \quad (2.13)$$

$$f = S^{0.5} * e^{-\left[\frac{1-S}{0.54}\right]^4} \quad (2.14)$$

$$F_D = 1 - 8.75 * (D_r - 0.2) * (1 - S) * e^{\left[-\frac{(1-S)^2}{2 * \left(1 - 0.84 * \left(\frac{0.2}{D_r}\right)^{0.25}\right)^2}\right]} \quad (2.15)$$

$$F_\gamma = 1 - 1.75 * \left(-\log \frac{\gamma}{0.001}\right) * (1 - S) * e^{[-3.1 * (1-S)^2]} \quad (2.16)$$

where S is degree of saturation, D_r is relative density and γ is shear strain.

Earthquake-induced irregular strain histories are represented by uniform strain cycles with an equivalent uniform cyclic strain amplitude (γ_{cyc}) and equivalent number of cycles (N_γ). In the second stage, excess pore water pressure ratio (r_u) is going to be calculated as a function of (N_γ / N_{\max}). Number of cycles required to reach $r_{u\max}$ (N_{\max})

was found to be dependent on parameters S , D_r , γ and σ'_v that are mentioned through equations 2.17 to 2.19 . Since $r_{u\max}$ includes the effects of S , D_r and γ , for simplicity purposes, N_{\max} was directly correlated to $r_{u\max}$ in mathematical modeling.

$$\frac{N_{\max}}{N_L} = (20 \times e^{-3r_{u\max}}) \quad (2.17)$$

$$N_L = (5.33 \times e^{-2011\gamma})\sigma'_v \quad (2.18)$$

$$N_{\max} = 107 * e^{-(3r_{u\max}+2011\gamma)} * \sigma'_v \quad (2.19)$$

where σ'_v is effective stress in kPa. Eseller-Bayat feel the necessity of more research at this step of mathematical model to get an accurate relation between N_L at different effective stresses. This research is going to focus on numerical modeling of cyclic simple shear condition under higher effective stress. Also the formulation between N_L and σ'_v is going to be modified with numerical results.

N_γ is related to the earthquake magnitude (M) in ground response analysis that is shown in equation 2.20.

$$N_\gamma = 0.0065 * e^{\left[\left(\frac{10}{M-1}\right)^{1.8} + 0.72M\right]} \quad (2.20)$$

The rate of excess pore water pressure ratio ($r_u/r_{u\max}$) is function of N_γ/N_{\max} , which is mentioned in equation 2.21 and 2.22(Eseller-bayat, Yegian, & Alshawabkeh, 2013)

$$\frac{r_u}{r_{u\max}} = v\left(\frac{N_\gamma}{N_{\max}}\right) = \left[\frac{\sin\left[\left(\frac{N_\gamma}{N_{\max}} - 0.5\right) * \pi\right] + 1}{2}\right]^{0.54} \quad for \quad \frac{N_\gamma}{N_{\max}} < 1 \quad (2.21)$$

$$\frac{r_u}{r_{u\max}} = 1 \quad for \quad \frac{N_\gamma}{N_{\max}} \geq 1 \quad (2.22)$$

3. NUMERICAL MODELING OF GEOTECHNICAL PROBLEM IN FLAC^{3D}

Fast Lagrangian Analysis of Continua in 3Dimensions which is abbreviated to FLAC^{3D} is three dimensional explicit finite-difference program. In fact FLAC^{3D} extends the calculation of FLAC into three dimensions and simulate the three dimensional behavior of soil, rock and other materials. Materials are represented by polyhedral elements which respond to the applied force according to stress/strain laws that are known as constitutive models. By using the explicit lagrangian calculations, FLAC^{3D} models the plastic collapse and flow very accurately. FLAC^{3D} uses fully dynamic equation for solving any problem. Dynamic problems are problems with high frequency and short duration. In FLAC^{3D} dynamic solution is optional.

Both finite element and finite difference methods convert differential equations into matrix equations for each element, and find the displacement at nodes by considering the force, but in this procedure there are some differences between these two methods. FLAC^{3D} do the calculation by using fully dynamic equation of motion even for static systems.

Explicit solution which is used in FLAC^{3D}, calculate the nonlinearity in stress/strain law in time intervals same as linear.

FLAC^{3D} can handle any constitutive model with no adjustment to solution algorithm. In the finite element codes different solution technique is necessary for different constitutive models.

FLAC^{3D} also contains a powerful programming language which is named as FISH that enables the user to define new functions or variables.

FLAC^{3D} is more effective for nonlinear and large-strain problems.

Nomenclature used if FLAC^{3D} is consistent with that used in other finite elements and finite difference programs for stress analysis. The basic definitions of some terms are reviewed in this part.

“Zone” is the smallest geometric domain that change of phenomenon is evaluated. Different shapes of zones are used to create models.

“Gridpoint” are corners of the finite difference zone. Number of gridpoints in a zone depends on shape of it.

Finite difference “grid” or mesh is assemblage of one or more finite difference zones across the physical region that is being analyzed.

The periphery of finite difference grid is named “boundary”. Boundary conditions is prescription of a constraint or controlled condition along model boundary.

“Initial condition” is the state of all variables in the model before any loading change or disturbance.

“Constitutive models” shows the deformation and strength behavior prescribed to zone in FLAC^{3D}.

“Static solution” is the default calculation in FLAC^{3D}. At the end of the static calculation model will be either be at state of equilibrium or at state steady flow of material.

“Unbalanced force” indicates when mechanical equilibrium state is reached for static analysis. The exact equilibrium is reached when nodal force at each grid point reaches zero. Maximum nodal forces are called unbalanced forces but it should be considered that it will never exactly reach to zero for a numerical analysis. Model is considered to be in equilibrium when maximum unbalanced force is small compared to total forces in model. When unbalanced force approaches a constant nonzero value, this probably indicates that failure and plastic flow are occurring.

“Dynamic solution” uses a full dynamic equation of motion for solving the problems involving high frequency and short duration loads.

“FISH” is programming language embedded within FLAC^{3D} that enables the users to define new variables and functions. These functions may be used to extend FLAC^{3D} usefulness or add user defined features.

3.1 Grid Generation

Grid generation in FLAC^{3D} can be distorted to fit complicated volumetric regions. FLAC^{3D} has powerful grid generator to manipulate the grid to fit various shapes of three dimensional problem domains. The purpose of grid generator is to facilitate creation of all required physical shapes in the model. Grid generation involves patching together grid shapes of specific connectivity to form a complete model with desired geometry. Grid generation is invoked with GENERATE command. Different primitive shapes are available in FLAC^{3D} that can be performed with GENERATE ZONE command to create complex three-dimensional geometries. This command actually access a library of primitive shapes. Some of the primitive shapes that are available in FLAC^{3D}, are going to be summarized with their associated keywords. Table 3.1 shows the available mesh shapes in FLAC^{3D}.

Table 3.1 : Primitive mesh shapes available with the GENERATE zone command.

Keyword	Definition
Brick	Brick-shaped mesh
Wedge	Wedge-shaped mesh
pyramid	Pyramid -shaped mesh
cylinder	Cylinder-shaped mesh
radbrick	Radially graded mesh around brick
radcylinder	Radially graded mesh around cylindrical-shaped tunnel
Cshell	Cylindrical shell mesh

Primitive can also be applied individually or connected together. The keyword SIZE defines the number of zones in the grid. In addition to SIZE there are several different keywords available to define characteristics of primitive shapes.

For sizing the grids for accurate results some factors should be considered. Firstly finer meshes lead to more accurate results because they provide a better representation of high-stress gradient then as zone ratio tends to unity accuracy of calculation increases.

Different corner points of the shape can be defined in zone generation command. By use of this corner points desired shape can be generated. For a brick shaped zone, eight corner points should be defined to create positive zone volume.

3.2 Boundary Conditions

Boundaries of the model will influence the results of calculation, so it is necessary that boundary condition be defined for the model. After grid generation, boundary conditions are going to be applied. Boundary conditions in numerical model are consist of two categories: real boundary and artificial boundary. Real boundaries exist in the physical object being modeled. Artificial boundaries do not exist in reality.

Mechanical condition can be applied to the model in two main types: prescribed displacement and prescribed stress. By default, the boundaries of FLAC^{3D} grid are free from stress and any constraint. Forces or stresses may be applied to any boundary. Displacement cannot be applied directly in FLAC^{3D} and they play no part in the calculation process. For giving displacement to a boundary, it is necessary to prescribe boundaries velocity.

A deep underground excavation is surrounded by infinite medium. The surface and near surface structures are assumed to be half space. The effect of these infinite mediums should be considered for modeling. Use of large models can be a solution for this problem because in large model the material will absorb the energy in the reflection of wave from the boundary. The disadvantage of this solution is large computation.

The alternative solution is using the quiet boundaries. It is based on the use of independent dashpots for normal and shear directions (figure 3.1). Quiet boundaries are best suited when the dynamic source is inside the grid. When the dynamic source is boundary condition at top or base the free field boundaries should be used. These boundary conditions are applied to the large scale models that are affected by surrounds. For simple shear test on shaking table because of small size, it is not necessary to use these boundary conditions. The boundaries of the box are the walls of cyclic simple shear liquefaction box.

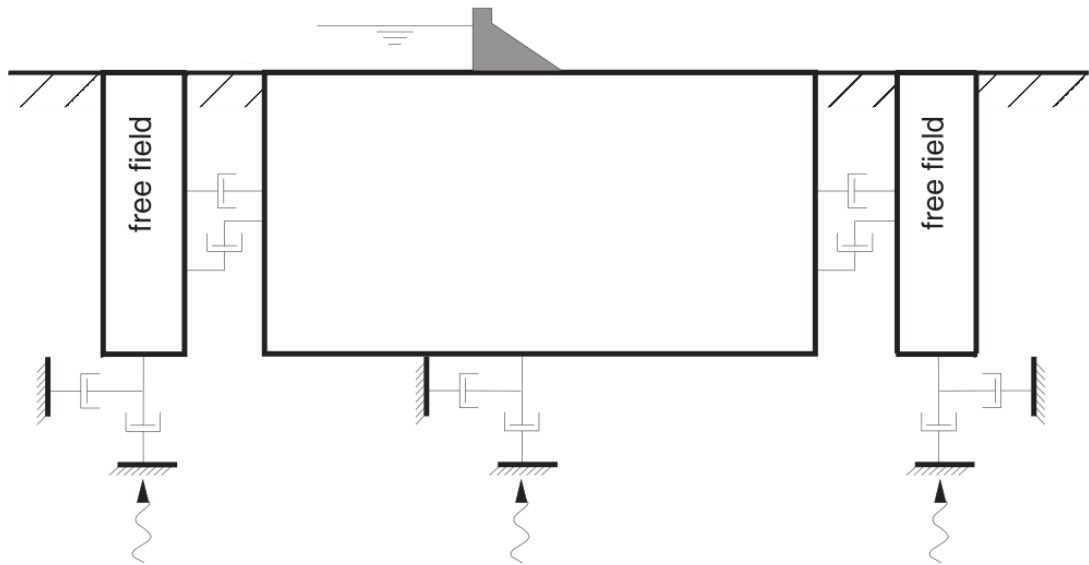


Figure 3.1 : Dynamic boundary conditions in FLAC^{3D}.

CSSLB has four sidewalls that are made of rigid Plexiglass. Walls in z direction are rotating walls (larger walls) that constrain the soil sample to have uniform shear strain. The other two walls are fixed walls (in x direction). Fixed walls have shorter length. This will help to minimize the boundary effect in shaking direction. Walls are modeled in FLAC^{3D} by using elastic constitutive model. The properties of Plexiglass material is so assigned that bending or any other deformation is prevented under applied load. Rotating walls are connected to bottom and fixed walls by joint sealant.

It may be necessary to alter the values of applied stresses during the course of a FLAC^{3D}. For example, the load on a footing may change. To effect a sudden change in an existing applied stress or load, a new APPLY command is given, with the range and stress component given exactly as in the original command, but with different value or variation.

3.3 Initial Conditions

In all engineering projects, there is some insitu state of stress in the ground before any construction started. This in-situ state can be reproduced by FLAC^{3D} by field measurement, information about initial state comes. In uniform layer of soil or rock with free surface, vertical stress usually is equal to $\gamma \cdot z$. Where γ is unit weight of soil or rock and z is depth below the surface. It is very difficult to estimate horizontal stress. If enough knowledge is known about the history of particular volume of material,

simulating the whole process numerically to arrive the initial condition can be done but this procedure is not feasible most of the times.

By using SET GRAVITY command gravitational acceleration operates on grids. This command does not directly cause stress to appear in the grid. Near the depth or on free fields, variation of stress with depth can not be ignored. For describing effect of depth, gradient parameters are going to be defined. The gradient parameters on the initial condition must be given in a way that stress gradient matches the gravitational gradient. Gradient is specified with grad keyword in FLAC^{3D}. Equation 3.1 shows the way of applying gradient in FLAC^{3D}

$$S = S^{(0)} + g_x x + g_y y + g_z z \quad (3.1)$$

Where the $S^{(0)}$ is value at coordinate origin and g_x , g_y and g_z specify the variation of the value in x, y and y directions. The stress contour plot interpolates the zone stress from the centroid to boundary. So it should be considered that FLAC^{3D} does not show stress in a point exactly.

Displacement cannot be applied directly in FLAC^{3D}. In order to apply a given displacement to a boundary it is necessary to prescribe the boundary velocity for given number of steps.

3.4 Soil Models

Constitutive Modelling is the mathematical description of how materials respond to various loadings. Major proposes of considering the constitutive model is behavior of deformable bodies. Experimental evidences for various phenomena are used as the basis for construction theories. Important factor of constitutive modelling is properties of strain tensor which impact directly to the stress tensor. (Niels Saabye, 2005).

There are 15 basic mechanical constitutive models provided in FLAC^{3D} that are arranged into null, elastic and plastic model groups. Some of these mechanical constitutive models are going to be noted in this part briefly. Null model is a material model that is used to represent material which is excavated or removed. Elastic isotropic model provides the simplest representation of material behavior. This model is only usable for homogenous, isotropic and continuous materials where the relation between stress and strain is linear. Elastic transversely isotropic model gives the ability

to simulate layered elastic media where there are difference between elastic moduli in direction normal and parallel to the layers. Mohr-Coulomb model is the conventional model used to represent shear failure is soil and rocks. Mohr-Coulomb model match well with laboratory tests results for sand and concrete. The strain hardening softening model allows representation of nonlinear material and softening and hardening behavior based on the Mohr-coulomb model properties. Modified cam clay model maybe used to represent soft clay behavior when the influence of volume change on the bulk modulus is considered and resistance to shear is needed to be taken in consideration.

In this part firstly the algorithm used for calculation in constitutive models is going to be discussed. In this research two of above mentioned models are used. These two models are Elastic and Mohr-Coulomb models which are going to be discussed in the next part.

3.4.1 Algorithm Used in Constitutive Models in FLAC^{3D}

All the constitutive models have the same numerical algorithm in FLAC^{3D}. Constitutive model gets the stress state at the time t and strain increment for Δt as input. The purpose is determining the new stress at time $t+\Delta t$. In plasticity theory the total strain increment is decomposed to into elastic and plastic parts. (FLAC^{3D} manual, constitutive models). Most of the mechanical constitutive models in FLAC^{3D} are calculating the plastic deformation. General steps for determining the new stress at time $t+\Delta t$ is mentioned below.

- 1) Yield function (f) is function that shows where the plastic flow takes places. This function represents a surface, where all the points below it are characterized by elastic behavior and points on the surface show the plastic behavior.
- 2) Equation 3.2 shows the strain increment, which is decomposing of elastic and plastic strain

$$\Delta \varepsilon = \Delta \varepsilon^e + \Delta \varepsilon^p \quad (3.2)$$

where $\Delta \varepsilon$ is strain increment, $\Delta \varepsilon^e$ is elastic strain increment and $\Delta \varepsilon^p$ is plastic strain increment.

3) The relationship between elastic strain increment and stress increment is going to be calculated by using a linear function named U. As it was mentioned in equation 3.3 only the elastic part of the strain contributes to the stress increment.

$$\Delta\sigma = U(\Delta\varepsilon^e) \quad (3.3)$$

4) The flow rule (g) is specifying the direction of plastic strain increment vector in equation 3.4. λ is constant number which shows the quantity of the plastic strain increment.

$$\Delta\varepsilon^p = \lambda * \frac{dg}{d\sigma} \quad (3.4)$$

5) The new stress vector should satisfy the failure criterion, so as it is mentioned in equation 3.5

$$f(\sigma + \Delta\sigma) = 0 \quad (3.5)$$

According to equations 3.1 and 3.2 and by reminding the fact that only the elastic part of the strain contributes to the stress increment, and considering S as a function which relates strain and stress, equation 3.6 can be written as

$$\Delta\sigma = S(\Delta\varepsilon) - S(\Delta\varepsilon_p) \quad (3.6)$$

New stress (σ_N) which is mentioned in equation 3.7 is calculated by adding the initial stress (σ_i) to equation 3.4

$$\sigma_N = \sigma - \lambda S\left(\frac{dg}{d\sigma}\right) \quad (3.7)$$

3.4.2 Elastic model

The elastic models are characterized by reversible deformation after unloading. The relation between strain and stress is linear in these models. The elastic models include both isotropic and anisotropic elastic models. In isotropic elastic models the strain increment generates stress increment by using reversible Hook law which is mentioned in equation 3.8.

$$\Delta\sigma = stiffness * \Delta\varepsilon \quad (3.8)$$

When the isotropic elastic models are used in FLAC^{3D} the inputs are bulk modulus and shear modulus. The walls of the CSSLB are modeled by using elastic models. The assigned material properties for Plexi-glass, the material which is used for walls, is 2e11 Pa assigned for bulk modulus and 1e11 Pa assigned for shear modulus.

3.4.3 Mohr-Coulomb model

All plastic models involves some degrees of permanent deformations. Different plastic model in FLAC^{3D} are characterized by their yield function, hardening/softening function and flow rule. These functions represents one or more limiting surfaces in a stress space where the points below surface has elastic behavior and points on the surface has plastic behavior. The plastic flow formulation in FLAC^{3D} rests on the basic assumptions of plasticity theory. For considering the dynamic behavior of sand samples in CSSLB dynamic analysis where done by Mohr-coulomb model. Major scope of dynamic analysis is observing the same shear strain in the height of sample and confirming simple shear behavior of model. One of the most general models in geotechnical engineering is Mohr-Coulomb model. Mohr-coulomb criterion is expressed in terms of principal stresses σ_1 , σ_2 and σ_3 . Mohr-Coulomb model considers the plastic behavior material. This model can be applied to loose and cemented granular materials, soils, rocks and concrete.

Yield function used in FLAC^{3D} for Mohr-Coulomb model is consisting of two parts, shear failure criterion f^S and tensile failure criterion f^t .

The shear failure criterion is stated in equation 3.9.

$$f^S = \sigma_1 - \sigma_3 N_\phi + 2C \sqrt{N_\phi} \quad (3.9)$$

Where C is the cohesion of the soil and the ϕ is frictional angle. N_ϕ is satted in equation 3.10.

$$N_\phi = \frac{1 + \sin \phi}{1 - \sin \phi} \quad (3.10)$$

Tension failure criterion is mentioned in equation 3.11.

$$f^t = \sigma_3 - \sigma^t \quad (3.11)$$

where σ^t is tensile strength.

Figure 3.2 shows the failure criterion used for Mohr-Coulomb model in FLAC^{3D}.

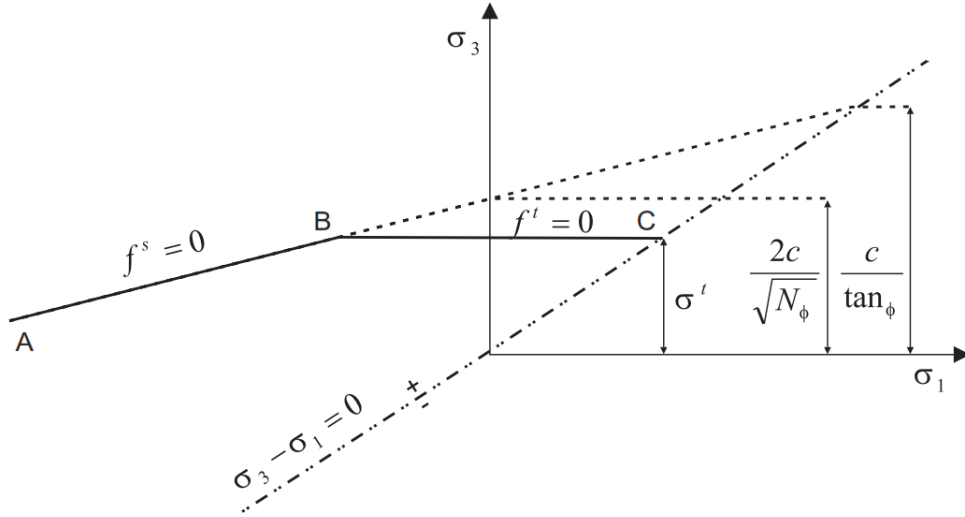


Figure 3.2 : Mohr-Coulomb failure criterion

The flow rule of Mohr-Coulomb model is also described by two functions, shear plastic flow (g^s) and tensile plastic flow (g^t) that are mentioned in equations 3.12 and 3.13.

$$g^s = \sigma_1 - \sigma_3 N_\psi \quad (3.12)$$

$$g^t = -\sigma_3 \quad (3.13)$$

$$N_\psi = \frac{1 + \sin \psi}{1 - \sin \psi} \quad (3.14)$$

3.5 Dynamic Loading and Damping

In the experimental setup done by (Eseller-Bayat, 2009) specimen is affected by sinusoidal uniform dynamic loading. Dynamic input in FLAC^{3D} can be applied in following ways.

- 1) An acceleration history
- 2) A velocity history
- 3) A stress history
- 4) A force history

These histories can be applied to the model in two forms. In the first form the history is going to be applied by a defined table. The table has multiplier values and corresponding time values that are entered as individual pairs of numbers. In the second form the load is going to be applied with a FISH function. When the FISH function is used to provide a dynamic motion, the function must access to dynamic time which is used scalar variable and is known as dytime. Equation 3.15 shows the relationship between uniform sinusoidal wave and frequency and time

$$V = ampl_V * Sin(2 * \pi * freq * t) \quad (3.15)$$

where V is velocity, $ampl_V$ is amplitude of velocity uniform wave, freq is frequency of the motion and t shows the dytime

As it was mentioned, the dynamic history can be applied in four types. By considering these four types the displacement cannot be applied to the model. So the amplitude of displacement which is taken from experimental test should be converted to the amplitude of velocity. This conversion is stated in equation 3.16.

$$ampl_V = ampl_D * 2 * \pi * freq \quad (3.16)$$

where $ampl_D$ is amplitude of displacement.

Natural dynamic systems have some degree of damping in vibration. Without damping the system will oscillate indefinitely. Damping is in fact the energy loss as the result of friction in the material. FLAC^{3D} uses damping in solution of both static and dynamic problems. The natural damping of soil and rock is mainly hysteretic and it is independent of frequency but it is hard to reproduce it numerically. Figure 3.3 shows the energy losses because of damping in stress-strain graph.

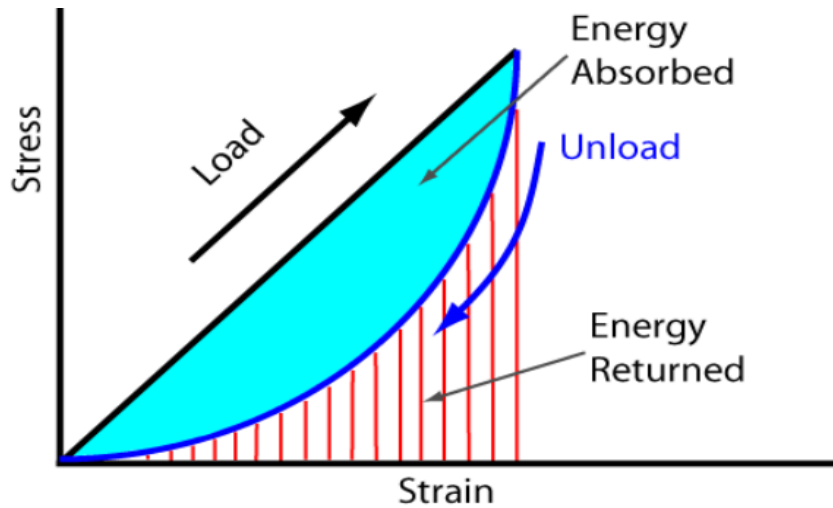


Figure 3.3 : Loss of energy under loading (damping)

In FLAC^{3D} when the plasticity models such as Mohr-Coloumb is used two kinds of damping are preferred to be applied to the model, Rayleigh damping and Hysteretic damping.(FLAC^{3D} version 5, 2012)

Rayleigh damping uses an equation which is expressed in matrix form and it uses with components proportional to the mass and stiffness. This kind of damping is specified in FLAC^{3D} with two parameters f_{min} (minimum frequency) and ξ_{min} (damping ratio). For geological materials the ξ_{min} is 2% to 5%.

Some times in the modeling small amount of stiffness proportional Rayleigh damping (0.05% at 2 Hz) may be added along with other kinds of damping to remove the noise. This small damping does not affect the deformation of the model. In this model hysteretic and Rayleigh damping are both used.

Rayleigh damping is not popular with the users because it increases the time solution. Hysteretic damping is described which may be used by its own or along with other kinds of damping such as Rayleigh damping. The hysteretic damping is not intended as complete model and it should be in conjunction with constitutive models.

When damping occurs, shear modulus of soil decreases. Some experimental research were done for calculating shear modulus degradation. Shear modulus degradation curve for sand is mentioned in figure 3.4.

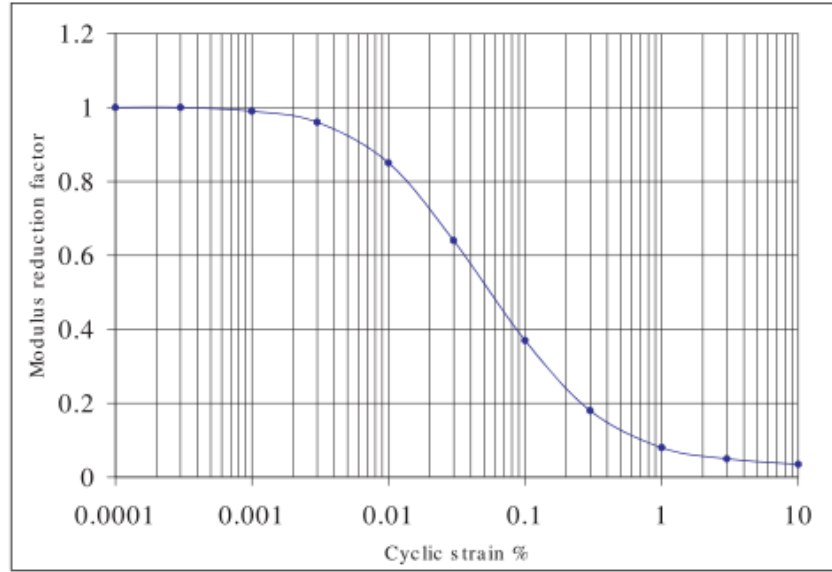


Figure 3.4 : Modulus Reduction curve for sand (Seed and Idriss, 1970).

For hysteretic damping different continuous functions are used to represent the modulus-reduction curve. When the hysteretic damping is used in FLAC^{3D}, the name of the function should be stated in the command. Various functions represent shear modulus reduction factor G/G_{\max} with cyclic strain.

- 1) Default model
- 2) Sigmoidal models (sig3, sig 4)
- 3) Hardin/Drnevich model

Each of these models has some inputs to fit with the Seed & Idriss data for sand or clay. Table 3.2 shows the inputs of these functions.

Table 3.2 : Numerical fits to Seed & Idriss data for sand(FLAC 3D version 5, 2012).

Data set	Default	Sig3	Sig4	Hardin
Sand	$L_1 = -3.325$	$a = 1.014$	$a = 0.9762$	$\gamma_{ref} = 0.06$
	$L_2 = 0.823$	$b = -0.4792$	$a = -0.4393$	
		$x_0 = -1.249$	$x_0 = -1.285$	
			$y_0 = 0.03154$	

3.6 Numerical Modeling of Liquefaction

Liquefaction is loss of shear strength of loose fully saturated sands under monotonic or cyclic loading due to momentarily undrained conditions. When saturated cohesionless sand is exposed to monotonic or cyclic loading, sand tendency for densification causes the pore-water pressure increment and effective stress decreases. This process leads to sand liquefaction. Constitutive models in FLAC^{3D} cannot model the liquefaction directly. It is necessary to do coupled dynamic-ground water analysis for this purpose. Most of the coupled models are referred to specific laboratory tests so they do not do calculation accurately for all conditions. FLAC^{3D} can model ground water flow, pore-pressure dissipation and coupling between porous solid and viscous fluid flowing within the pore space. There are several types of fluid/solid interaction in FLAC^{3D}. By setting the flow calculation on or off, FLAC^{3D} can consider or neglect pore pressure dissipation. Liquefaction can be modeled in FLAC^{3D} by accounting irreversible volume strain in constitutive model. The modeling of liquefaction can be done in FLAC^{3D} by Finn model which is provided by dynamic option.

During application of cycling loading to saturated sand if drainage is restricted volume reduction cannot occur and that causes increment of pore-water pressure. Pore-water pressure increment reduces the effective stress that may reach zero. This is definitions of initial liquefaction and in this research it is used as liquefaction triggering point. The relation between pore-water pressure increment during undrained cycling loading and volume reduction under drained cycling loading is considered by Finn et al. For this relationship it is necessary to have analysis which is coupled with dynamic response.

Simple shear test is used for calculating the relationship between pore water pressure increment during undrained cyclic loading and volume changes in drained cyclic tests. Simple shear test conditions simulate best field deformation induced in horizontal sand deposits by earthquake excitation (Martin, Seed, & Finn, 1975).

3.6.1 Relationship between the volume reduction and pore-water pressure increment

If a specimen of saturated sand under drained conditions is subjected to one cycle of loading with specific shear strain amplitude in simple shear condition, volumetric strain increment corresponding to decrease in volume occurring during cyclic loading is named $\Delta\varepsilon_{vd}$. If one cyclic loading with same shear strain amplitude is applied under undrained condition the volumetric deformation is going to convert to pore-water pressure increment.

By considering the changes in volume of voids ($\frac{\Delta u \cdot n}{K_w}$) equal to changes in volume of sand structure, equation 3.17 can be written.

$\frac{\Delta u}{E_r}$ is recoverable increment of volume in sand structure that is mentioned as equation 3.17.

$$\frac{\Delta u \cdot n}{K_w} = \Delta\varepsilon_{vd} - \frac{\Delta u}{E_r} \quad (3.17)$$

where Δu is increase in residual pore pressure of the cycle, K_w is bulk modulus of water, n is porosity of sample, E_r is rebound modulus of one dimensional unloading curve and $\Delta\varepsilon_{vd}$ is reduction in volume of sand

The above mentioned equation can be written as equation 3.18

$$\Delta u = \frac{\Delta\varepsilon_{vd}}{\frac{1}{E_r} + \frac{n}{K_w}} \quad (3.18)$$

For fully saturated samples, bulk modulus of water is $K_w = 2.2 \times 10^6 \text{ kPa}$. Water may be considered to be effectively incompressible so under conditions of zero volume change equation 3.19 is going to be written (Martin, Seed, & Finn, 1975).

$$\Delta u = E_r \cdot \Delta\varepsilon_{vd} \quad (3.2)$$

For induced partially saturated soil (air and water mixture) bulk modulus of water K_w decreases rapidly for relatively small reduction in degree of saturation. As the result water becomes more compressible, so the pore-water pressure increment will reduced.

For predicting pore water pressure it is necessary to have knowledge about recoverable deformation characteristic of sand under one dimensional unloading from initial vertical effective stress. Volumetric strain after unloading has two parts: (1) No recoverable strain component (2) Recoverable strain component. It is necessary to evaluate E_r from effective stress unloading process (equation 3.20). This process has been gotten from curves of experimental tests and analytical process.

$$E_r = \frac{(\sigma'_v)^{1-m}}{mk_2} * (\sigma'_{v0}{}^{m-n}) \quad (3.20)$$

In which σ'_{v0} is initial value of effective stress and k_2 , m and n are experimental constants for given sand.

3.6.2 Volumetric strain increment calculation

It was vital to introduce a method for computing the volume changes of dry sand under dynamic loading. After computing the volume changes, pore-water pressure generation can be calculated. Two simple formulation which are considered for volumetric strain changes are named Martin equation and Byrne equation. These two methods are going to be discussed briefly.

3.6.2.1 Martin equation

Martin considered that the volumetric strain increment depends on volumetric strain and cyclic shear strain amplitude. Martin also noticed that volumetric strain and cyclic shear strain are independent of confining stress. By using the curves that was plotted from experimental tests and some analytical functions which fits to the curves, equation 3.21 was introduced for calculating the volumetric strain increment (Martin et al., 1975).

$$\Delta\varepsilon_{vd} = C_1(\gamma - C_2\varepsilon_{vd}) + \frac{C_3 + \varepsilon_{vd}^2}{\gamma + C_4\varepsilon_{vd}} \quad (3.21)$$

There are four constants in the equation that the values of them are $C_1=0.80$, $C_2=0.79$, $C_3=0.45$ and $C_4=0.73$ for the plots of the samples with relative density equal to 45%.

3.6.2.2 Byrne equation

Byrne defined an alternative and simpler equation to show the relationship between the volumetric strain increment, shear strain amplitude and volumetric strain. (Liam

Finn, Lee, & Martin, 1977). In equation 3.22 prepared by Byrne also effective stress do not contribute in volumetric strain calculation.

$$\Delta\varepsilon_{vd} = \gamma C_1 e^{\left(-C_2 \left(\frac{\varepsilon_{vd}}{\gamma}\right)\right)} \quad (3.3)$$

C_1 and C_2 mentioned in equations 3.24 and 3.25 are constants, that can be calculated for different relative densities using equation 3.23.

$$C_1^C = 7600(D_r)^{-2.5} \quad (3.23)$$

$$C_1 = \frac{C_1^C}{2} \quad (3.24)$$

$$C_2 = \frac{0.4}{C_1^C} \quad (3.25)$$

The above mentioned equations can be written using standard penetration test results (equation 3.26 and 3.27).

$$D_r = 15(N)_{60}^{0.5} \quad (3.26)$$

$$C_1^C = 8.7(N)_{60}^{1.25} \quad (3.27)$$

$(N)_{60}$ is SPT blow count when 60 percent of theoretical free-fall hammer energy is used in the test. In addition to C_1 and C_2 a third coefficient C_3 , is assigned which sets the threshold shear strain where the strain below it does not produce volumetric strain. In this thesis Byrne model was used for liquefaction calculations. Data used in numerical modeling have various relative densities. For this reason Byrne equation realized more appropriate.

4. NUMERICAL MODEL OF CYCLIC SIMPLE SHEAR STRAIN TESTS ON SHAKING TABLE

4.1 Overview of Cyclic Simple Shear Liquefaction Box (CSSLB)

Simple shear apparatus has been designed by number of researchers. Norwegian Geotechnical Institute Simple Shear Apparatus (NGISSA) uses cylindrical specimens. The specimen that is used in this apparatus is 8 cm in diameter and 2 cm in height. Shear strain is applied from top plate which moves parallel to fixed bottom plate. Because of small size of this apparatus it is not suitable for using in research on liquefaction of partially saturated soil.

The Cambridge University Simple Shear Apparatus Mk7 (CUSSA Mk7) uses square shaped specimens with dimensions 10cm x 10cm x 2cm. The sidewalls parallel to the direction of shaking are fixed relative to the base and sidewalls perpendicular to the direction of shaking are attached to the base by hinges. Again, because of the small size of the box, it was decided that this box would not be adequate for preparing and testing partially saturated sand specimens.

The Northeastern University Liquefaction Box (NULB) is a larger testing apparatus. It has two fixed sidewalls and two rotating sidewalls. The rotating sidewalls are fixed to the base by hinges. The base is fixed to a shaking table at the bottom. Top of the rotating sidewalls are connected to each other by a rigid metal bar. Movement of shaking table causes rotation of hinged walls of the box. In the NULB, the two rotating sidewalls are attached to the plane surfaces of the two fixed sidewalls by a flexible joint sealant. At these connections, the sand is prevented from shearing and thus causing non-uniform shear strains along the fixed sidewalls. The results of tests have shown that boundary effects are obvious in the NULB apparatuses.

The existing apparatus are almost capable for testing small soil samples and they are not suitable for preparing and testing large partially saturated sand specimens under cyclic or earthquake type excitations.

Cyclic Simple Shear Liquefaction Box (CSSLB) was designed and manufactured at Northeastern University to diminish the undesirable effects and limitations of the NUBL and allows testing fully and partially saturated tests specimen under controlled drainage conditions.(Eseller-Bayat et al., 2013)

The CSSLB enclose the soil sample with four walls that are made of rigid Plexiglass. Walls also make the sample water tight over the four related sides. For making the shear box water tight a flexible joint sealant is necessary between the rotating and fixed walls that could compress and elongate.

Figure 4.1, shows the idea of manufacturing the CSSLB. There are two rotating walls that are perpendicular to shaking motion and hinged to the bottom of plate on the shake table. Two other side walls are fixed to the bottom of plate on the shake table. Flexible sealant is used between the fixed and rotating walls and bottom of the box to make the CSSLB watertight. These flexible material are also used to allow free turning of rotating walls. At the top of the box two rotating walls are fixed by connecting to beam, these connections do not allow any movement at the top of the walls but they are free for rotating. Schematic figure of simple-shear box is demonstrated in figure 4.1.

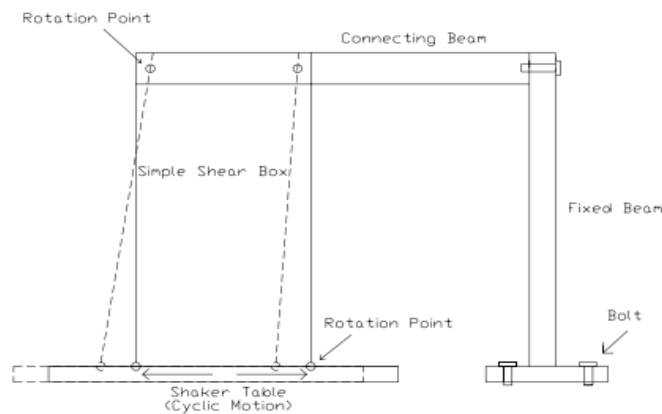


Figure 4.1 : Schematic Drawing of the Simple-Shear Test Setup

The inside plane of CSSLB is 19cm×30cm. Preparing the sample with different degrees of partial saturation should be considered for estimating the height. As the consequences, 49cm was considered as the optimum height. This height minimizes the boundary effects. Shape and dimensions of the box are important parameters for minimizing the boundary effects. By making the smaller wall (19cm) parallel to shaking direction the boundary effects are minimized

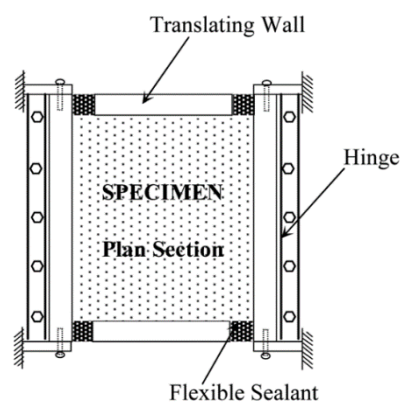
Shaking table which was used in the experimental test is uniaxial and it is connected to a computer-based data acquisition system which applies any kind of movement. Shaking table is obvious in the figure 4.2



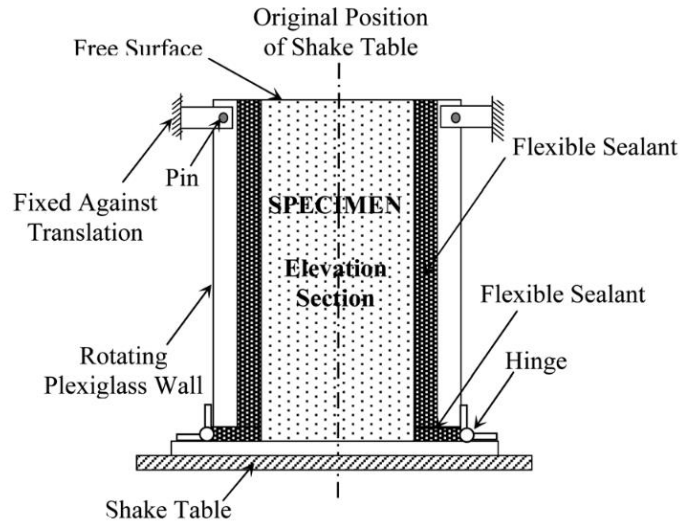
Figure 4.2 : Shaking Table of Northeastern University and CSSLB box.

The CSSLB has four walls that are made of rigid Plexiglass and make the sample water tight over the four related sides. For making the shear box water tight a flexible joint sealant is necessary that could compress and elongate along the rotating walls. The connection between the cover plates are made of flexible joint sealant. The sealant which is used can compress or elongate up to 5cm.

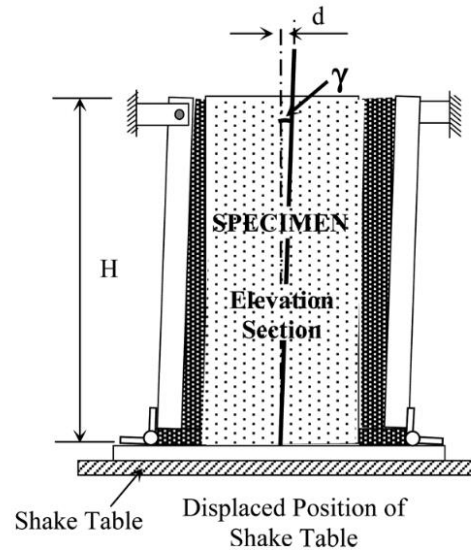
The box is capable to measure the pore pressure by Pore Pressure Transducers (PPT). Shear strain of the soil is equal to the lateral displacement, divided by height of the specimen. CSSLB has capability of applying simple shear to the sample. Plan section of CSSLB and the sketches of original and displaced positions of CSSLB are shown in figure 4.3.



(a)



(b)



(c)

Figure 4.3 : Simple shear mechanism for the CSSLB: (a) plan section before shearing, (b) elevation section before shearing, and (c) elevation section after shearing by displacing shaking table.(Eseller-Bayat et al., 2013).

Elastic model was used for modelling the walls of cyclic simple shear liquefaction box (CSSLB). The elastic models are characterized by reversible deformation after unloading . Parameters which are going to be assigned to material in elastic model are shear modulus (G), bulk modulus (K) and density (ρ). Behavior of the side walls of the CSSLB, bottom of the box and flexible sealant material (rubber) are considered elastic. Properties of the material used in CSSLB for numerical modelling are mention

in table 4.1. In the numerical modelling of laboratory scaled apparatus it is not necessary to define dynamic boundaries which are used for infinite environments.

Numerical simulation of cyclic simple shear liquefaction box and simple shear direction is shown in figure 4.4.

Table 4.1 : Material properties used for numerical modelling of CSSLB

Material	Bulk modulus (K) in Pa	Shear modulus (G) in Pa	Poisson ratio (ν)
Plexi-glass	2.00E+11	1.00E+11	0.3
Flexible sealant (rubber)	8.333E+5	8.62E+4	0.45

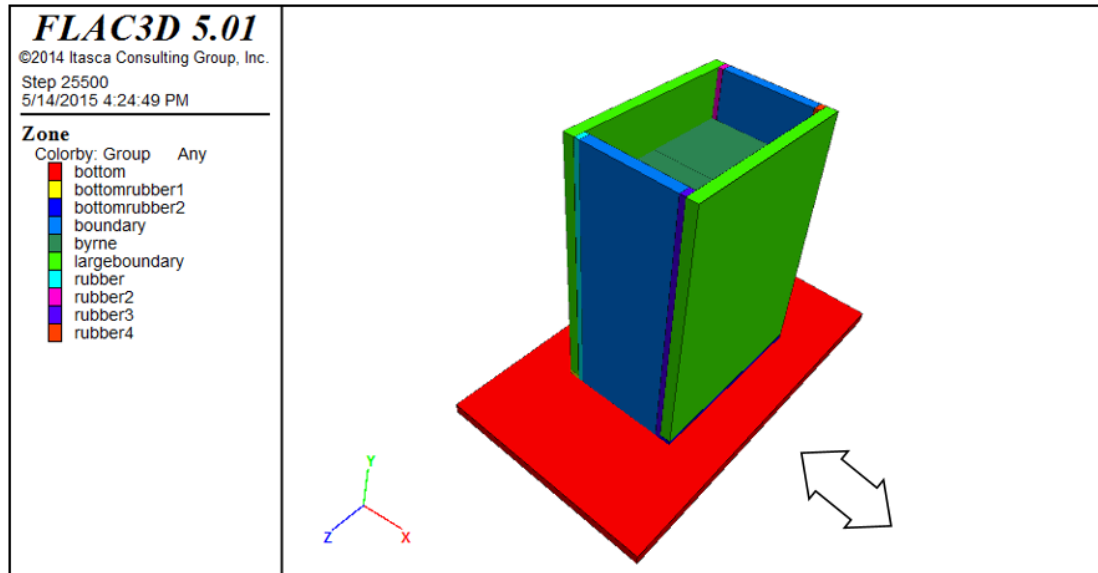


Figure 4.4 : CSSLB and simple shear direction.

4.2 Material Properties

Because of high uncertainty in database, selecting the material properties is one of the most important steps of generating a numerical model. For geomechanics problems, field data will never be known completely. By appropriate selection of material properties based on available database important view of problem can be solved. The material properties required in FLAC^{3D} are categorized in two groups. First group consider the deformability properties of material and second group discusses the strength properties. This part provides guidelines of selecting properties of material

used for given model. Before discussing the deformability and strength properties of sand mass density should be chosen.

Material properties are conventionally derived from laboratory testing setups. In absences of complete properties of material, some approximate number are used which are gained from experimental setups. Sometimes these experimental setups only do not consider the exact circumstance of real data. It is obvious that these numbers do not express the exact material properties.

4.2.1 Mass density

In FLAC^{3D} calculation, mass density is only required when the gravity is specified. Mass density has the units of mass divided by volume ($\frac{\text{Kg}}{\text{m}^3}$). If the unit weight is defined with units of force divided by volume, this value should be divide by gravitational acceleration. Direction of gravitational acceleration should also be defined in FLAC^{3D}. Density of Ottawa sand which is used in experimental setup done by Eseller-Bayat is calculated by equation 4.1.

$$\gamma = \frac{G_s + S * e}{1 + e} * \gamma_w \quad (4.1)$$

where γ is soil density in ($\frac{\text{Kg}}{\text{m}^3}$), S is degree of saturation, e is void ratio of soil, γ_w is water density ($1000 \frac{\text{Kg}}{\text{m}^3}$) and G_s is specific gravity of sand which is considered 2.65 for Ottawa sand.

In the experimental setup which was done by Eseller-Bayat relative density (D_r) of the soil sample was known. Before calculating the density of soil, void ratio should be computed. For this purpose relationship between D_r and e is going to be used. Maximum void ratio (e_{\max}) and minimum void ratio (e_{\min}) of the Ottawa sand is assumed for what was recommended for C109 soil at ASTM. In this gradation system $e_{\max}=0.85$ and $e_{\min}=0.5$.

4.2.2 Deformability properties of sand

All the constitutive models in FLAC^{3D} except for the transversely isotropic elastic and orthotropic elastic models assume an isotropic material behavior in elastic range. Elastic constants which are preferred in FLAC^{3D} are bulk modulus (K) and shear

modulus (G). It is believed that bulk modulus and shear modulus correspond to more fundamental aspects of material behavior. Young's modulus (E) and Poisson's ratio (ν) can also be considered as elastic constants of material. Elastic constants can be converted to each other. For this scope equations 4.2, 4.3 and 4.4 are used.

$$K = \frac{E}{3(1 - 2\nu)} \quad (4.2)$$

$$G = \frac{E}{2(1 + \nu)} \quad (4.3)$$

$$K = \frac{E \cdot G}{3(3G - E)} \quad (4.4)$$

4.2.2.1 Shear modulus of sand

As it was mentioned in previous section shear modulus (G) is one of the elastic components, which is necessary for numerical modeling. Backbone curve shows locus of secant shear modulus (G_{sec}) vs. shear strain (γ) as it is shown in the figure 4.5. Soil stiffness depends on different parameters such as cyclic strain amplitude, void ratio, number of loading cycles etc. By increasing the amplitude of cyclic strain the secant shear modulus reduces. Slope of back bone curve at zero cyclic strain amplitude shows the maximum shear modulus G_{max} . (Kramer, 1996).

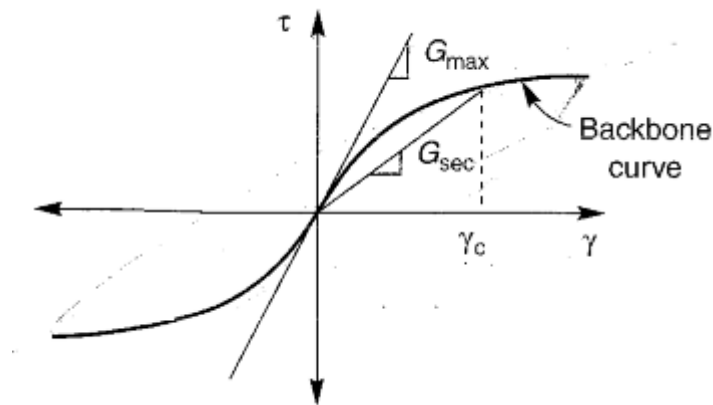


Figure 4.5 : Shear stress vs. Shear strain (Kramer, 1996).

There are two general equations for G_{\max} calculation. First equation for maximum shear modulus calculation is developed by Seed and Idress (1970). This method uses effective stress and soil relative density for shear modulus calculation instead of shear wave velocity. Equations 4.5, 4.6, 4.7 shows the shear modulus calculation.

$$G_{\max}(PSF) = 1000K_{2\max}\sqrt{\sigma'_m}(PSF) \quad (4.5)$$

$$K_{2\max} = 20(N_1)_{60}^{\frac{1}{3}} \quad (4.6)$$

$$K_{2\max} = 20\left(\frac{D_r}{15}\right)^{\frac{2}{3}} \quad (4.7)$$

There is also another way for soil maximum shear modulus calculation. Use of measured shear wave velocity is a general way for evaluating the G_{\max} in particular soil deposits. Seismic geophysical tests are commonly used for this purposes. Equation 4.8 is introduced for calculating the maximum shear modulus for tests with small shear strains with using the shear wave velocity. Seismic geophysical tests are commonly used for measuring the shear wave velocity.

$$G_{\max} = \rho \cdot V_s^2 \quad (4.8)$$

Shear wave velocity measurement which is used in this research were performed by Eseller-Bayat in fully and partially saturated sand prepared in CSSLB. Shear wave velocity was measured for specimen prepared in CSSLB at lower and middle depth by bender elements which are located in the box as shown in Figure 4.6.

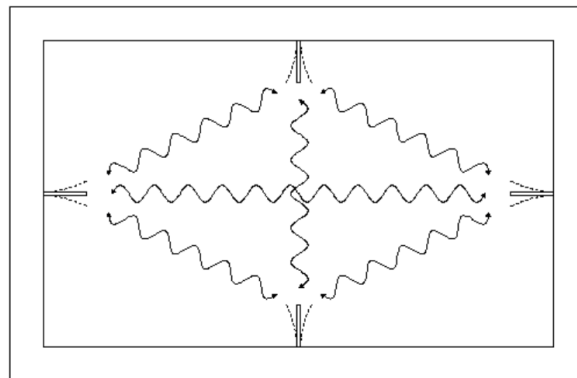


Figure 4.6 : Bender elements locations in plan view (Eseller-Bayat, 2009).

Good coupling is necessary between soil and bender elements to provide enough disturbances to soil particles. The bender elements are able to measure wave velocity for short and long distances. Measurement of shear wave velocity were done for samples with different relative densities and compared with theoretical correlations. For relative densities 20% and 70% shear wave velocity was measured 52.5 m/s and 70 m/s as it is obvious in the figure 4.7 and figure 4.8.

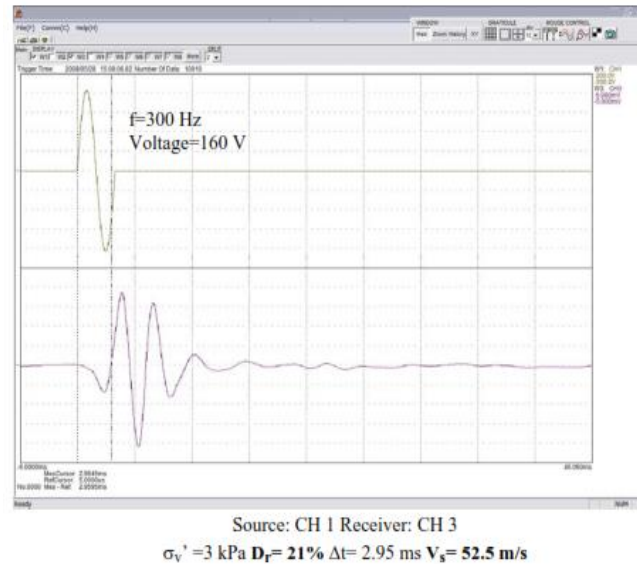


Figure 4.7 : Shear wave velocity for $D_r=21\%$ (Eseller-Bayat, 2009).

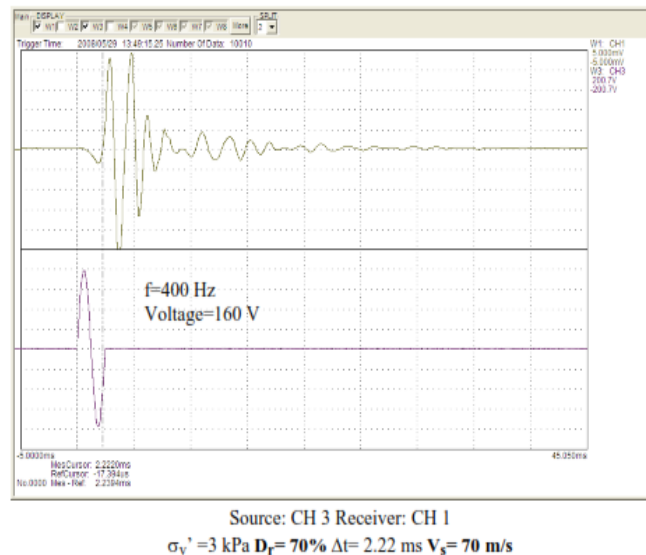


Figure 4.8 : Shear wave velocity for $D_r=70\%$ by (Eseller-Bayat, 2009).

The above mentioned results was compared with theoretical results which are presented by (Seed and Idriss 1970) as equation 4.5.

According to (Braja . Das 2006.)

$(N_1)_{60}$ for $D_r = 21\%$ is between 6 – 8

$(N_1)_{60}$ for $D_r = 70\%$ is 36

From equation 4.5 and 4.6

$$\frac{[(K_2)_{\max}]_2}{[(K_2)_{\max}]_1} = \sqrt[3]{\frac{36}{7}} \frac{(G_{\max})_2}{(G_{\max})_1}$$

From equation 4.8

$$\frac{V_{S2}}{V_{S1}} = \sqrt{\frac{(G_{\max})_2}{(G_{\max})_1} * \frac{\rho_1}{\rho_2}} = 1.28$$

So shear velocity at sample with $D_r=70\%$ is 1.28 times of the shear velocity at looser sample with $D_r=20\%$. This ratio between the two shear wave velocities corresponds with experimental results done by Eseller-Bayat. By using the above mentioned equations shear wave velocity (V_s) can be calculated for the other relative densities. Table 4.2 shows the relation between corrected $(N_1)_{60}$ and Relative Density.

Table 4.2 : Relation between corrected $(N_1)_{60}$ and Relative Density (D_r)(Das, n.d.).

Standard penetration number, $(N_1)_{60}$	Approximate relative density, D_r (%)
0-5	0-5
5-10	5-30
10-30	30-60
30-50	60-95

$(N_1)_{60}$ for $D_r=50\%$ is 20

$$\frac{V_{S2}}{V_{S1}} = \sqrt{\frac{(G_{\max})_2}{(G_{\max})_1} * \frac{\rho_1}{\rho_2}} = 1.1$$

By considering the $\rho_1 = 1.994 \text{ g/cm}^3$ and $\rho_2 = 2.03 \text{ g/cm}^3$

V_s is calculated for $D_r=20\%$, $D_r=50\%$ and $D_r=70\%$ so the shear modulus is calculated by equation 4.8.

4.2.2.2 Bulk modulus of sand

An important content which is categorized as one of the deformability properties in FLAC^{3D} is Bulk modulus. Bulk modulus was not measured directly in experimental setup done by Eseller-Bayat. As it was mentioned previously behavior of material is considered elastic under small shear strain amplitude. By using relationship between elastic contents, bulk modulus of sand can be specified. Equation 4.9 is used for this purpose.

$$K = \frac{2G(1 + \nu)}{3(1 - 2\nu)} \quad (4.9)$$

For calculating the bulk modulus, Poisson ratio of sand should be specified. Poisson ratio is the fraction of expansion in perpendicular directions to the compression in vertical direction as it can be seen in Figure 4.9.

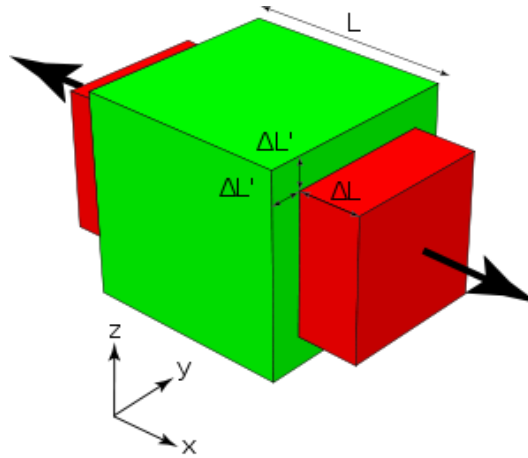


Figure 4.9 : Expansion of element in load perpendicular direction and compression in load vertical direction

Materials have the Poisson ratio between the 0.0 and 0.5. When the Poisson ratio is 0.5 the material is perfectly incompressible. Most specific example of incompressible materials is water.

Poisson ratio of sand is going to be considered by Skoglund studies. Skoglund et al suggest Poisson ratio as a factor which depends on confining pressure.

Table 4.3 : Poisson ratio for uniform sand (Skoglund, G. R. Marcuson III, W.F and Cunny, 1976)

Effective confining pressure (kPa)	Poisson Ratio ν
10.7	0.35
21.4	0.31
42.8	0.26

As it is obvious in table 4.3 by increasing the effective confining pressure, Poisson ratio decreases. The Poisson ratio can even be large values for the samples with smaller confining pressure. Poisson ratio used in this research is 0.35.

4.2.3 Strength properties of sand

The criteria of material failure in Mohr-Coulomb relation is a linear failure surface. Two strength constants which are used in this failure criteria are cohesion (c) and angle of friction (ϕ). These constants are conventionally derived from laboratory tests (Triaxial or direct and/or simple shear). Cohesion (c) and friction angle (ϕ) for soil specimen are given in table 4.4.

Table 4.4 : Friction angle of different material (Rc Chaney, Demars, Santamarina, & Cho, 2001).

Material	Friction Angle ϕ
ASTM graded sand	30°
Blasting sand	34°
Glass beads	21°
Ottawa 20-30	28°
Ottawa F-110 sand	31°
Sandboil sand	33°
Ticino sand	33°

For Ottawa sand which was used in this numerical modeling, cohesion (c) is considered zero and angle of friction (ϕ) is assumed 30°.

4.3 Dynamic Analysis of Numerical Model

Before considering the pore-water pressure generation, effective stress decrement and triggering the liquefaction, dynamic behavior of the sand is going to be observed. This behavior does not consider the effects of pore water pressure since FLAC^{3D} solves the dynamic response of the soil without considering the reduction in effective stresses due to liquefaction-induced pore water pressure generation

An equation is used for applying the uniform shear strain to all the zones. As 0.49 m is height of the box equation 4.10 is going to be multiple to velocity

$$\text{Local } V = V * \frac{0.49 - gp}{0.49} \quad (4.10)$$

where Local V is velocity of each grid point and gp show the position of each grid point. Figure 4.10 shows the applied velocity wave graphically.

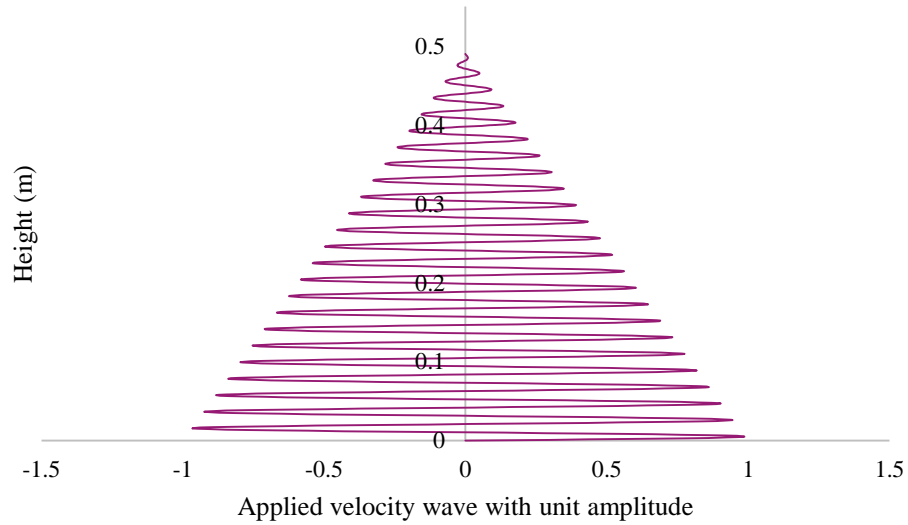


Figure 4.10 : The applied velocity wave to the model.

Choosing the maximum zone size is going to be discussed firstly in this section. A static equilibrium calculation precedes a dynamic results, so maximum unbalanced force of the dynamic numerical model is going to be considered in the next step. Simple shear condition controlling is going to be discussed in fifth section named numerical analysis results in FLAC^{3D}. Simple shear condition means observing same shear strain throughout the height of the sample. At the end shear stress-shear strain graphs will be stated in this part. The constitutive model used for dynamic model of

sand is Mohr-Coulomb model. Properties of material that were used in Mohr-Coulomb model was considered in the previous section.

Numerical distortion of the propagating wave may occur in a dynamic analysis. Frequency content of the input wave and speed of the wave will affect the numerical accuracy of wave transmission. For accurate representation of wave transmission through a model element size (Δl) must be smaller than approximately one-tenth to one eighth of the wave length associated with highest frequency component of input wave (Kuhlemeyer, R.L., 1973). Equation 4.11 shows the minimum element size relation

$$\Delta l \leq \frac{\lambda}{10} \quad (4.11)$$

where λ is the wave length associated with highest frequency components. Based on elastic properties for this problem p-wave and s-wave speeds are given by equation 4.12 and 4.13

$$C_P = \sqrt{\frac{K + 4G/3}{\rho}} \quad (4.12)$$

$$C_S = \sqrt{\frac{G}{\rho}} \quad (4.13)$$

By using equations 4.12 and 4.13 smallest wave velocity can be used for calculating wavelength if experimental results are not available. In this research experimental results prepared by Eseller-Bayat is used for wave speed. By considering the experimental efforts results, minimum value of C_S is equal to 50m/s. Highest frequency which is going to be applied is 15 Hz. Equation 4.14 is used for calculating highest frequency.

$$f = \frac{C_S}{\lambda} = \frac{C_S}{10 \cdot \Delta l} \quad (4.14)$$

By considering equation 4.14 max zone size should be smaller than 33 cm. In this model 19 cm is largest zone size that satisfies above mentioned suggestion.

4.3.1 Maximum unbalanced force

Before considering the dynamic analysis, initial equilibrium is going to be considered. When nodal force at each grid point reaches zero, equilibrium situation is obtained. As it was discussed at the beginning of section 3, maximum nodal forces are called unbalanced forces. Unbalanced force specifies time, when mechanical equilibrium state is reached for static analysis. Figure 4.11 shows the unbalanced force obtained from dynamic analysis of CSSLB.

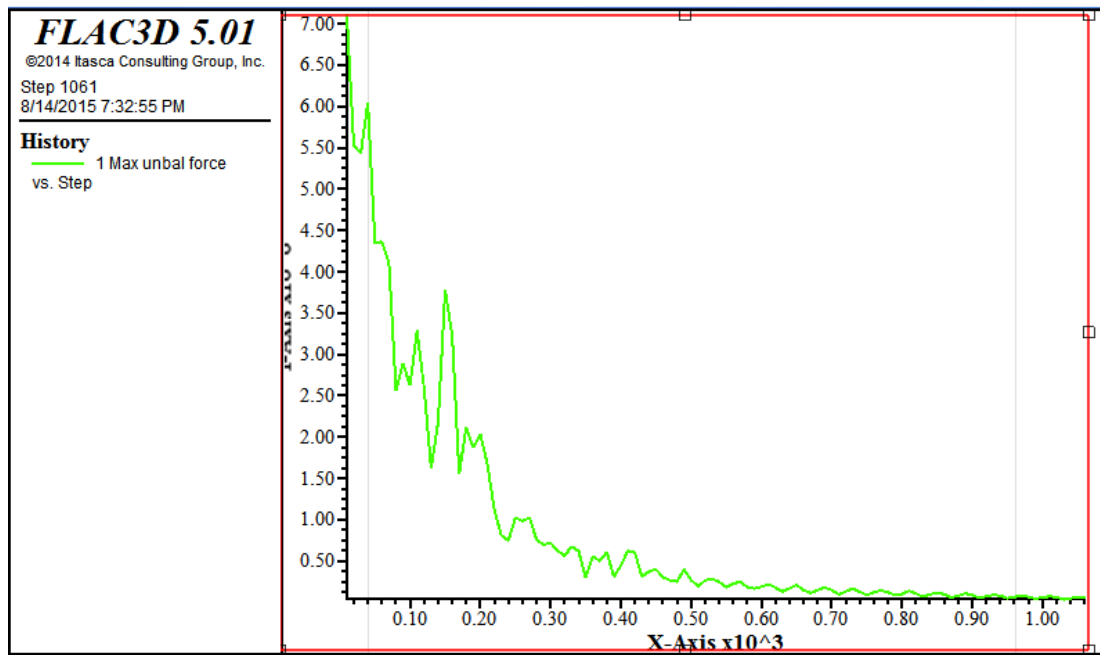


Figure 4.11 : Maximum unbalanced force when $D_r=42\%$ and $\gamma = 0.052\%$ for dynamic model

From figure 4.11. the maximum unbalanced force decreases abruptly and reaches to zero and static equilibrium is observed in the numerical model.

4.3.2 Shear stress-shear strain behavior

Soil stiffness is influenced by cyclic strain amplitude, void ratio, mean principal effective stress, plasticity index, over consolidation ratio and number of loading cycles. When the confining pressure is higher, linear cyclic threshold shear strain is greater. Figure 4.12 shows the shear stress-shear strain diagram for a dynamic numerical model. From the Figure 4.12 it was observed, under strain controlled condition degradation of the shear modulus occurs by increasing the number of cycles. As it is noticeable in the figure, the zone located at the lowest position have the higher values

of shear stress. Shear stress-shear strain graph of this zone is shown by yellow color. As elevation of zone increases in y direction (direction parallel to gravity) shear stress decreases. Damping that is used for this numerical modelling is sig3-Hysteretic damping but a small Rayleigh damping is add to decrease the noises.

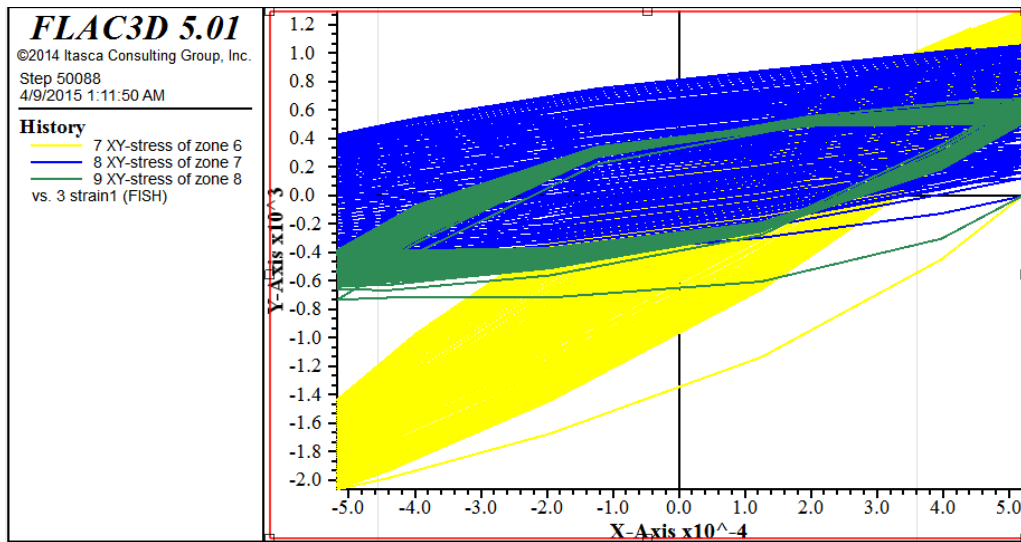


Figure 4.12 : Shear stress and strain relationship

4.4 Liquefaction Analysis of Numerical Model

This section considers the fully saturated and partially saturated sand numerical analysis. In the first part of this section liquefaction numerical modelling method is reminded briefly and initial liquefaction definition is stated. This definition is used as the liquefying point in numerical analysis. In the second part compressibility of air and water mixture which is used partially saturated sand in mentioned.

4.4.1 Fully saturated sand analysis

The primary effect of the cyclic loading is the irrecoverable volume contraction of the matrix of grains. If the voids are fully filled with fluid then the pore pressure of fluid increases and the effective stress decreases. Transfer of externally applied pressure from the grain to fluid cause the pore-water pressure increases. Pore pressure increment is not the main cause of liquefaction. In fact the decrement of the contact forces between the particles is responsible to liquefaction. The standard constitutive models in FLAC^{3D} do not model the liquefaction process directly.

Pore-pressure generation that is related to liquefaction can be modeled by accounting for irreversible volume strain in constitutive model. This mechanism is described by

Martin (1975) and Byrne (1991) which was stated at section 3. They noted that the relation between irrecoverable volume strain and cyclic shear-strain amplitude is independent of confining stress. The FINN built in model incorporates the Martin and Byrne relation into Mohr-coulomb plasticity model. By using the Finn and Byrne equation discussed in Chapter 3, pore pressure generation and effective stress decrement was considered for the soil. Initial liquefaction is defined as the point where the increment of pore pressure is equal to initial effective stress. Initial liquefaction is defined as the point where r_u reaches to one. By using the equations 4.15, 4.16, 4.17 and 4.18 it can be concluded that when r_u reaches one, effective stress is zero.

$$r_u = \frac{u - u_0}{\sigma_0} \quad (4.15)$$

where u is pore pressure in a specified stage, u_0 is initial pore pressure and σ_0 is initial effective stress.

$$\sigma'_0 = \sigma - u_0 \quad (4.16)$$

$$\sigma'_f = \sigma - u_f \quad (4.17)$$

where σ is total stress, σ'_f is final effective stress and u_f is final pore pressure.

If pore pressure ratio is equal to one at the final stage then $\sigma_0 = u_f - u_0$. It should be remembered that value of total stress is constant.

$$\sigma'_f = \sigma - (\sigma_0 + u_0) = 0 \quad (4.18)$$

Although there is no such thing in reality as an incompressible fluid, this term is used where the change in density with pressure is so small as to be negligible. The compressibility of a liquid is known as the bulk modulus. The bulk modulus is a property of the fluid and for liquids is a function of temperature and pressure. In most engineering problems, the bulk modulus at or near atmospheric pressure is the one of interest. Bulk modulus of water under different pressure and temperature is mentioned in table 4.5.

Table 4.5 : Bulk modulus of water under different pressure and temperature

Pressure kPa	Temperature °C		
	0°	20°	50°
100	2.02×10^9	2.2×10^9	2.3×10^9
10000	2.07×10^9	2.28×10^9	2.36×10^9
30000	2.19×10^9	2.4×10^9	2.5×10^9

As it is obvious in the table, compressibility of water do not change effectively at different temperature and pressure. Bulk modulus considered in the fully saturated numerical modelling is the one at the 20°C under 100 kPa. All these values are great enough to consider water incompressible.

4.4.2 Partially saturated sand analysis

In FLAC^{3D}, pore pressure is considered zero if degree of saturation at any point is less than 1. The effect of dissolved and trapped air may be allowed by reducing the fluid modulus while keeping the saturation at 1. It should be noticed that the compressibility of the fluid (C) is the reciprocal of bulk modulus (K).

Fluid compressibility is defined in two ways in FLAC^{3D} 1) Biot coefficient and Biot modulus are specified 2) Fluid bulk modulus and porosity are specified. The first case considers the compressibility of the solid grains. In the second case, solid grains are assumed to be incompressible. When the grain compressibility is neglected, the user has the choice to either use the default value of Biot coefficient which is equal to one and assign a value equal to bulk modulus over porosity ($\frac{K}{n}$) to Biot modulus, or give the fluid bulk modulus K as input.

High compressibility of air and water mixture is the main reason of increment of IPS resistance against liquefaction. Gas bubble in partially saturated sand is obvious in figure 4.13. What makes the numerical modeling of fully and partially sand different is the high compressibility of air and water mixture. The increment of compressibility is assigned to the numerical model by fluid bulk modulus.

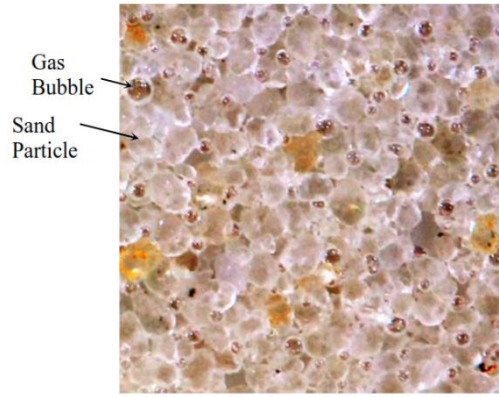


Figure 4.13 : Micro picture of partially saturated sand (S=80%) (Eseller-Bayat, 2009).

The compressibility of air and water mixture is calculated in different ways by the researchers. Boyle's and Henry's law are mostly used in these calculations. Some of the calculations take into account the surface tension between water and air while others ignored it by considering the same air and water pressures in the mixture. Boyle law is an experimental fluid law which describes how pressure of fluid increases as the volume decreases. Equation 4.19 and 4.20 show the Boyle law.

$$P.V = A \quad (4.19)$$

$$P_1.V_1 = P_2.V_2 \quad (4.20)$$

where A is a constant value. P_1 and P_2 are the pressures of fluid in first and second conditions and V_1 and V_2 are the volumes for the first and second conditions.

Henry's law says the amount of gas which dissolves in a given volume of liquid at a constant temperature, is proportional to the pressure of gas which is in equilibrium with liquid.

Bishop, Alan W, 1950 and Skempton and Bishop 1954 did their calculation based on Boyle's and Henry's laws. The surface tension and differences between air and water tension were disregarded by them. Koning 1963 calculated the compressibility of air water mixture by using Boyle's law. His formula is sufficient for practical proposes where pressure changes are small.

General definition of volume compressibility of a liquid is as in equation 4.21.

$$C = \frac{-1}{V} \times \frac{dV}{du} \quad (4.21)$$

where C is volume compressibility and V is volume of the air and water mixture that is equal to $V_a + V_w$ and it depends on pressure (u).

Water is incompressible material and volume change is zero. So the above mentioned equation can be written as in equation 4.22 for air and water mixture.

$$C_{wa} = \frac{-1}{V_w + V_a} \times \frac{dV_a}{du} \quad (4.22)$$

By considering the Bulk modulus or modulus of compressibility (K) as the factor that measures the resistance of material to uniform compression, K is the reverse of C . Koning 1963 did not take into account the influence of surface tension. The equation 4.23 was given by him for calculating the bulk modulus of water and air mixture.

$$\frac{1}{K_{wa}} = \frac{1}{K_w} \left(1 - \frac{V_a}{V}\right) + \frac{1}{K_a} \times \frac{V_a}{V} \quad (4.23)$$

Bulk modulus of air K_a is equal to water absolute pressure u_w and $\frac{V_a}{V}$ is equal to $1 - S$.

So the above mentioned equation can be written as in equation 4.24 (Koning, 1963)

$$\frac{1}{K_{wa}} = \frac{S}{K_w} + \frac{1 - S}{u_w} \quad (4.24)$$

Where S is the degree of saturation, K_w is water bulk modulus, K_{wa} is air and water mixture bulk modulus and u_w is absolute pore water pressure.

Schuurman did the first attempt to take into account all the factors on compressibility of air and water mixture in 1964. The calculations were done based on some simplifications. Temperature and volume of water remain constant and no free or dissolved air escapes from the water mixture. The compressibility of water can be disregarded in compression with compressibility of air and water mixture. The dimension of bubbles are assumed to be the same. (Schurmaan, 1967)

For numerical modelling of partially saturated sand, compressibility of the air and water mixture is defined by Koning equation. Possibility of numerical modelling of partially saturated sand with Koning equation will be known in section 5.

5. NUMERICAL ANALYSIS RESULTS IN FLAC^{3D}

5.1 Dynamic Analysis Results

This chapter discusses the dynamic analysis results of the sand specimen tested in CSSLB model. At the first part of this section simple shear condition is verified. Velocity time history is applied to the model in FLAC^{3D} at the bottom of the CSSLB, so it is necessary to verify the uniform simple shear strains condition throughout the specimen. In the second part of this section, dynamic settlement of the sand is mentioned.

5.1.1 Simple shear condition verification

CSSLB is an apparatus for applying simple shear condition to the soil. Before considering pore-water pressure generation in the numerical model, validity of simple shear condition should be confirmed. As it was mentioned at the beginning of the chapter 3, dynamic input in FLAC^{3D}, can be applied by acceleration history, velocity history, stress history and force history. Application of velocity was used in this modeling, therefore it is important to control simple shear condition. Constitutive model used for dynamic numerical modelling is Mohr-Coulomb model. Mohr-Coulomb model is a conventional model used to represent shear failure in soils and rocks. Material parameters that are assigned in Mohr-Coulomb model are shear modulus and bulk modulus of the sand, friction angle and soil density that were discussed in Part 4.2. In the numerical modeling of CSSLB in FLAC^{3D}, one directional sinusoidal wave is applied in the X-direction so no movement is expected at the perpendicular direction (Z-direction).

Different shear strains ($\gamma = 0.05\%$, $\gamma = 0.1\%$, $\gamma = 0.2\%$) were applied to the dynamic numerical model for checking the simple shear condition. By considering the X- displacement and elevation of the point, shear strain can be calculated. Shear strain is the ratio of X-displacement of a point to elevation from the source of movement

($\gamma = x_{\text{disp}}/\text{height}$). Figure 5.1 shows the location of A-A section view at CSSLB. A-A section views in figures 5.2, 5.3 and 5.4 shows the X-displacement of CSSLB under different velocity amplitudes.

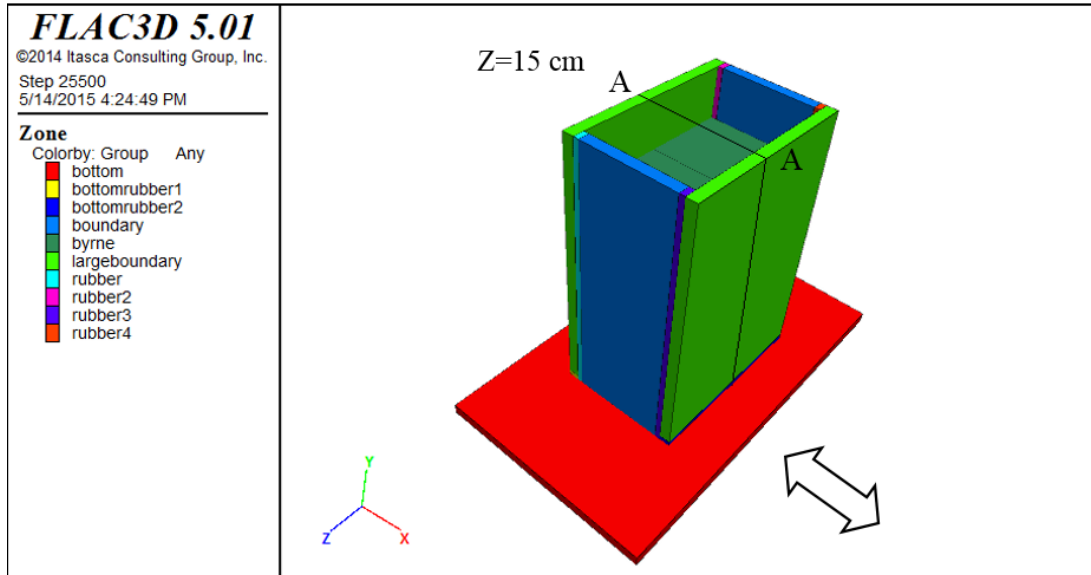


Figure 5.1: Middle section view of the CSSLB in Z-direction (A-A section view)

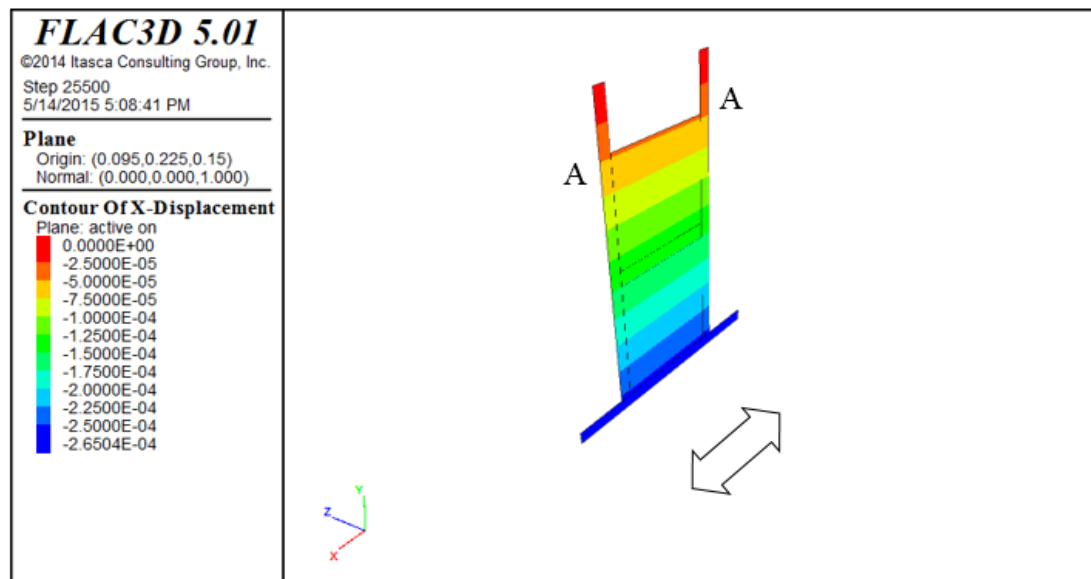


Figure 5.2: X-Displacement of specimen in section view when $\gamma = 0.05\%$.

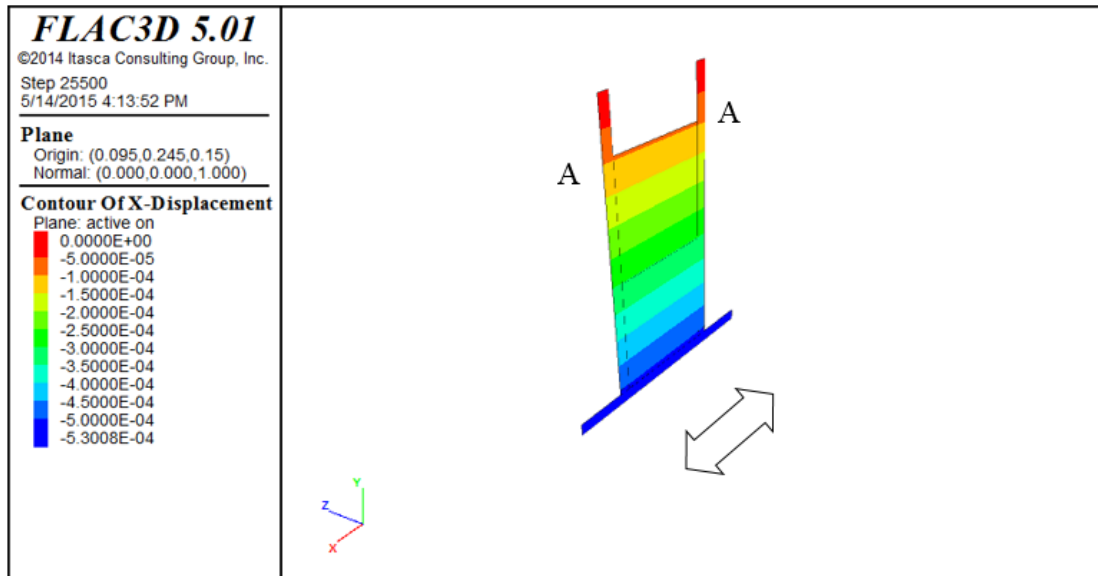


Figure 5.3: X-Displacement of specimen in section view when $\gamma = 0.1\%$.

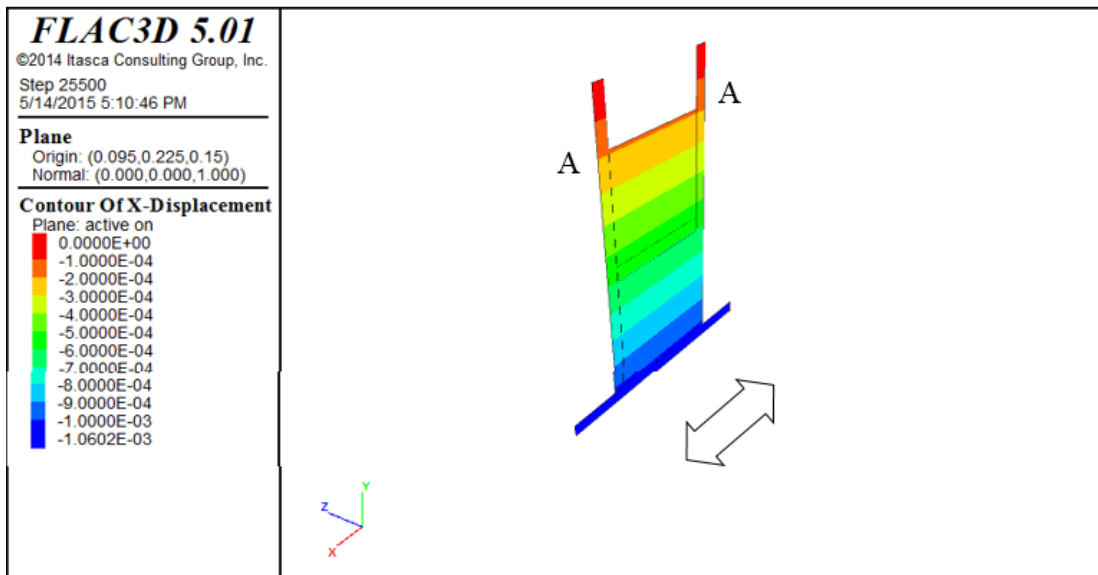


Figure 5.4: X-Displacement of specimen in section view when $\gamma = 0.2\%$.

As it is mentioned in Figures 5.2, 5.3 and 5.4, X-displacement induced by sinusoidal velocity waves with different amplitudes, can be observed. The displacements are in meter. Displacement of sand in X-direction for different shear strains can be seen in figure 5.5. As it is obvious, by increasing the elevation of the point, X-displacement increases linearly. This fact can confirm the simple shear condition. However shear strain is going to be calculated and compared in different heights.

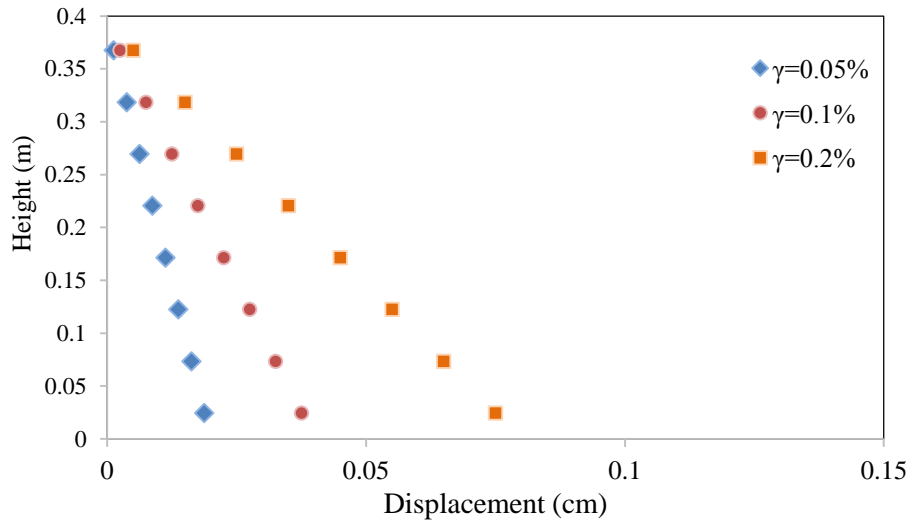


Figure 5.5: Displacements of the specimen in X-direction for different shear strains

Figure 5.6 confirms the uniformity of the shear strains throughout the depth of the sample for different strain amplitudes.

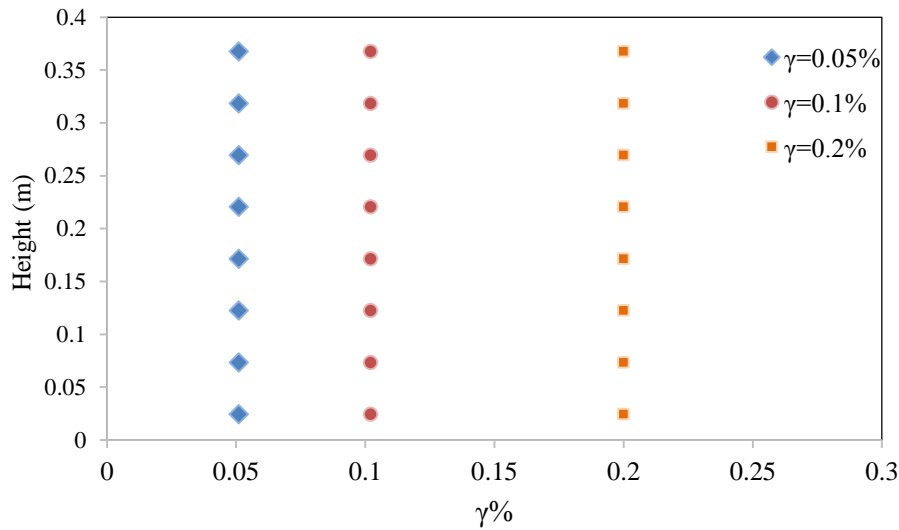


Figure 5.6: Uniform simple shear strains throughout the depth of specimen.

Shear strains are also executed in FLAC^{3D} by using a FISH function which is shown in figure 5.7. Shear strains of different zones at height of the model was considered for checking the simple shear condition. Shear strain was acquired by using a FISH which calculates the ratio of difference displacement in zones to height of the zone. Same shear strain was observed at the height of the sand specimen. By confirming simple shear condition, pore pressure generation and liquefaction calculations can be completed.

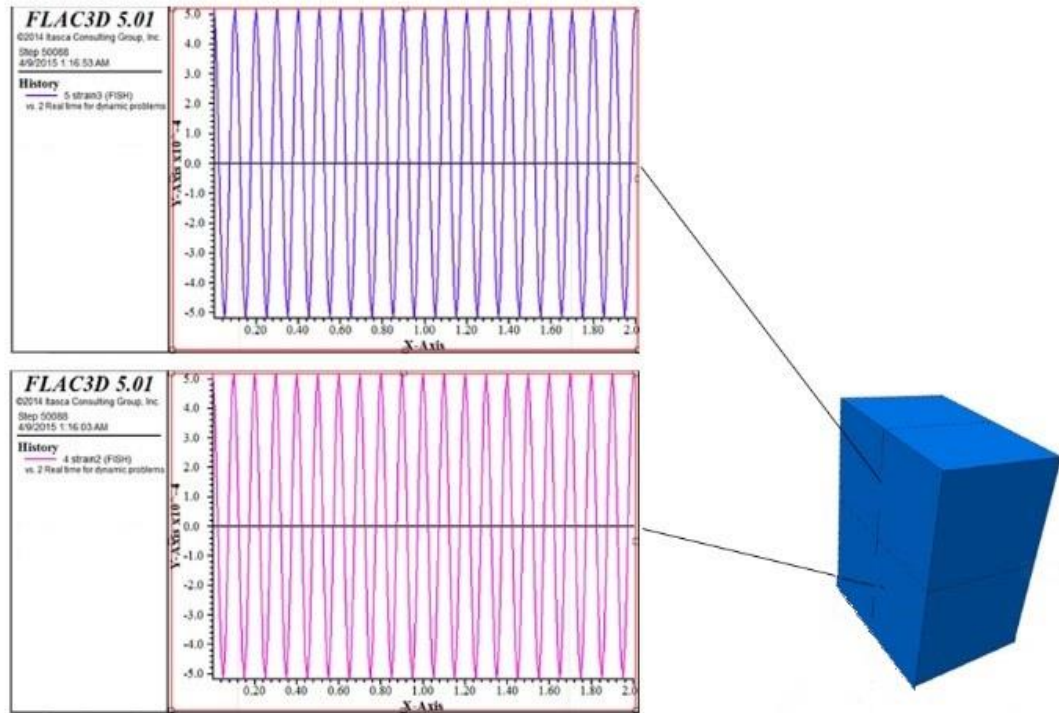


Figure 5.7: Observed shear strain for different zones of the specimen from FISH

Simple shear condition in different cross sections of CSSLB is also considered. Shear strain in cross sections near the walls should be studied to see the boundary effects in X-displacement. Same X-displacements in the cross sections confirms minimum boundary effects in the sand.

Figure 5.9 and figure 5.10 compare different shear strains, in different cross sections. As it can be seen in figure 5.9, same shear strain is obtained in all cross sections in Z-direction. Same shear strains, confirm the zero boundary effects. Also Figure 5.10 confirms the same conclusion for cross sections in X-direction. Boundaries in both directions do not have effect in X-displacement. This result confirm the uniform displacement of the sample at any point at a constant elevation.

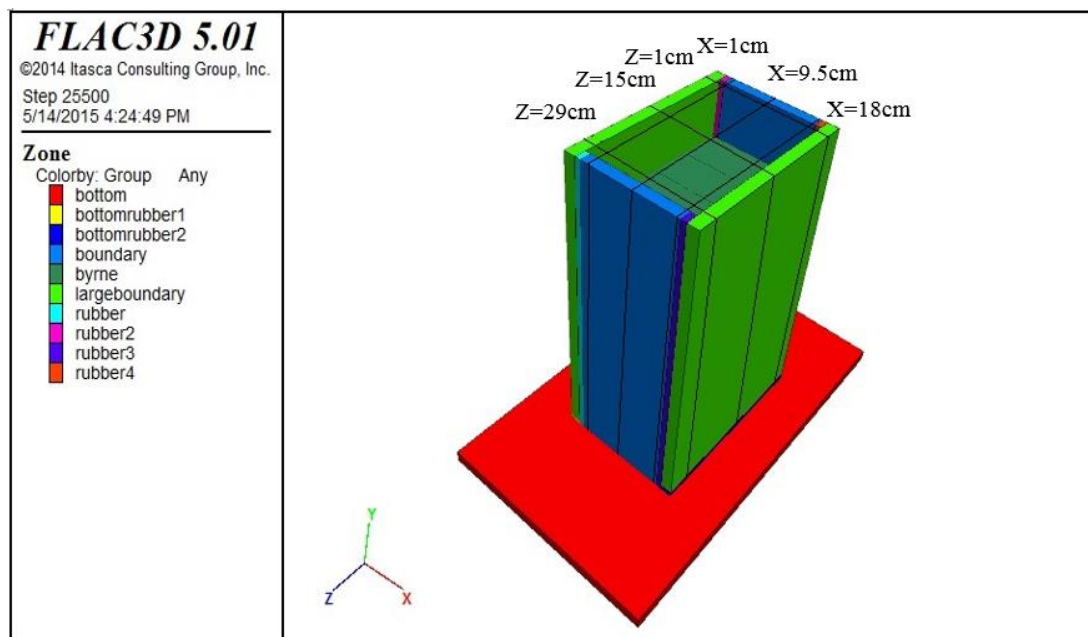


Figure 5.8: Different cross sections studied for X-displacement

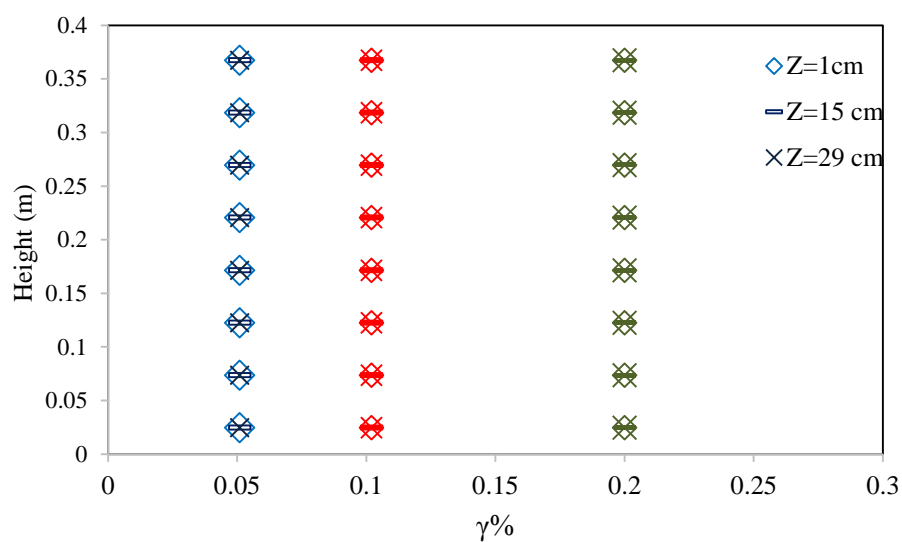


Figure 5.9: X-displacement at different cross sections in Z-direction

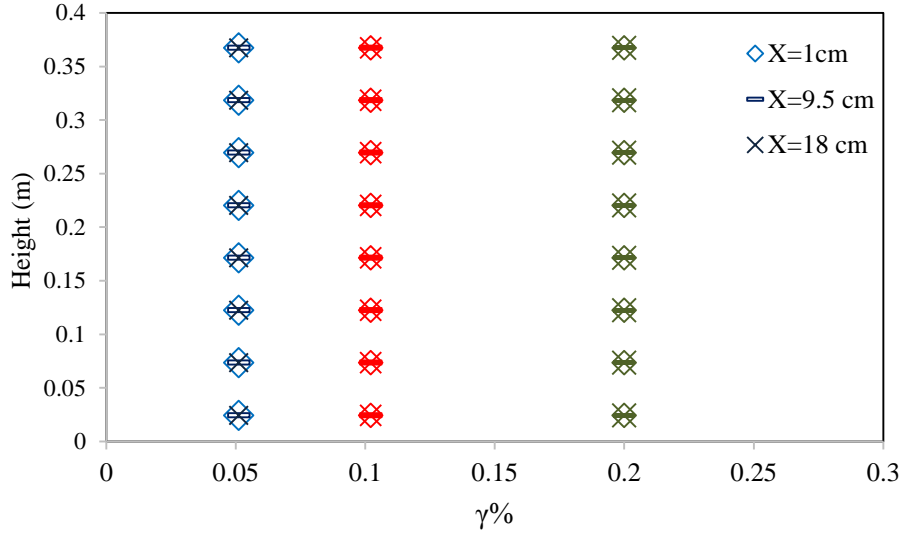


Figure 5.10: X-displacement at different cross sections in X-direction

5.1.2 Settlement of sand under dynamic loading

In this part, the settlement of sand in CSSLB due to only dynamic effect is calculated using FLAC^{3D} dynamic analysis. Shear modulus (G_{max}) of the sand was estimated using the equation from wave propagation theory and the empirical equation by seed 1970. The results obtained from these two equations are compared at the end.

As it was mentioned in chapter 4, there are two general ways for shear modulus calculation. Equation 5.1 obtained from wave propagation theory uses density (ρ) and shear wave velocity (V_s) as inputs. Shear modulus depends to the total density of the soil linearly, so for sand with higher density, bigger shear modulus is obtained. By considering the equation 5.1, fully saturated sand will have higher shear modulus and smaller settlement in compared in dry sand. Figures 5.11 thru 5.14 show the settlement of sand under 10 kPa vertical load when equation 5.1 is considered as maximum shear modulus.

$$G_{max} = \rho \cdot V_s^2 \quad (5.1)$$

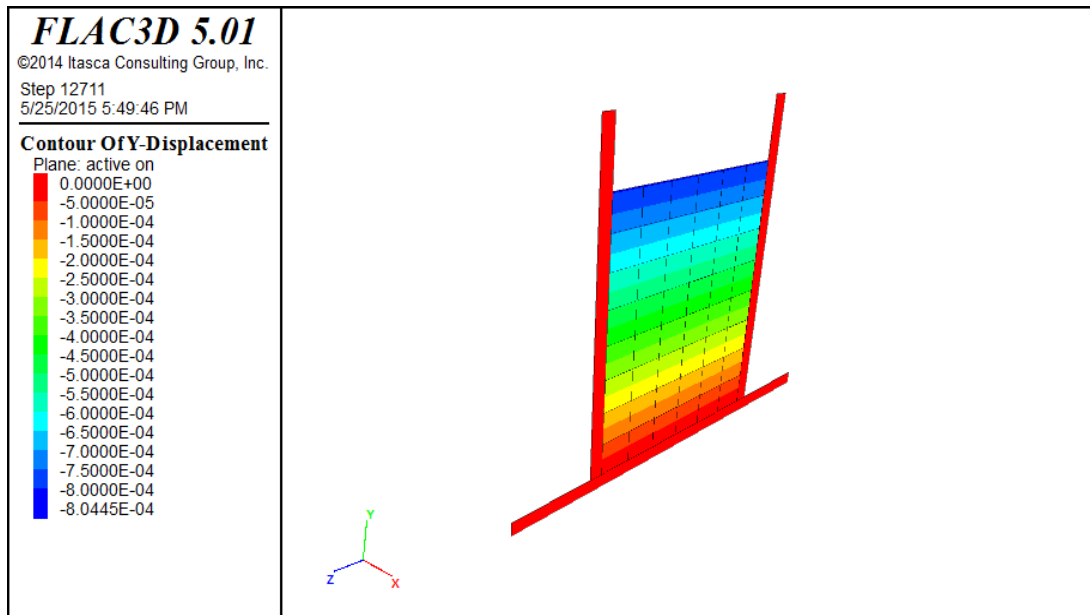


Figure 5.11: Settlement of fully saturated sand with $D_r=20\%$ under 10 kPa load under cyclic simple shear strain tests with $\gamma=0.052\%$ (using G_{\max} from eqn 5.1).

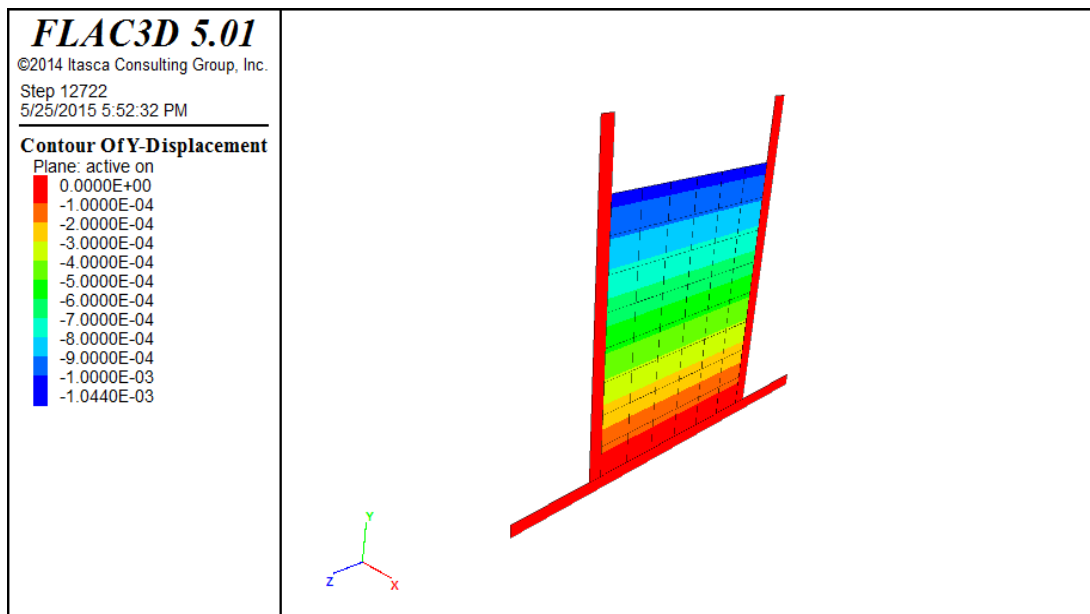


Figure 5.12: Settlement in dry sand with $D_r=20\%$ under 10 kPa load under cyclic simple shear strain tests with $\gamma=0.052\%$ (using G_{\max} from eqn5.1).

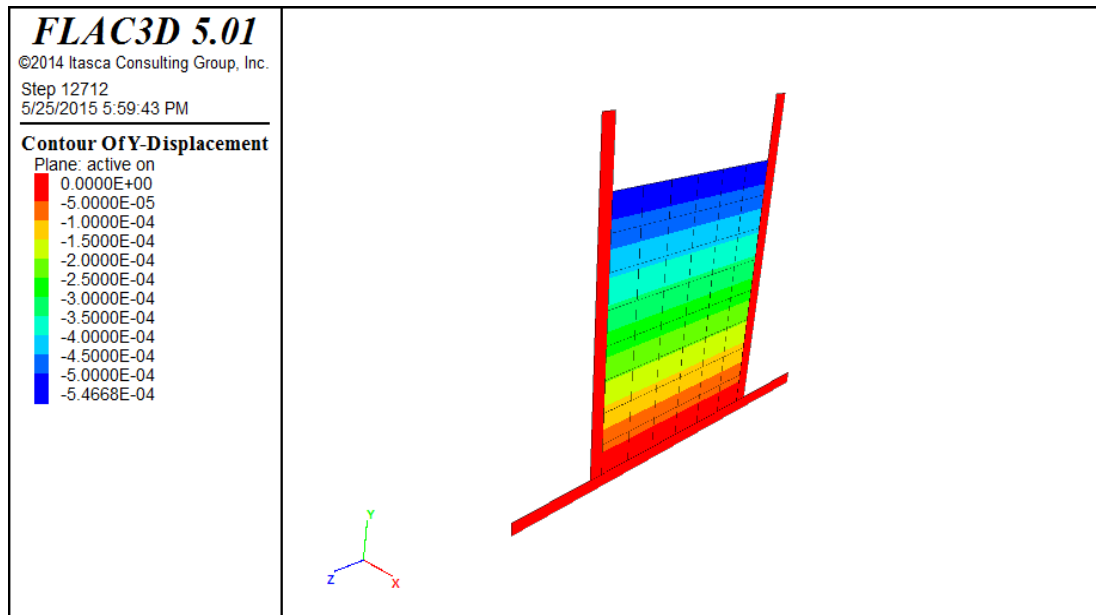


Figure 5.13: Settlement in fully saturated sand with $D_r=40\%$ under 10 kPa load under cyclic simple shear strain tests with $\gamma=0.052\%$ (using G_{max} from eqn 5.1).

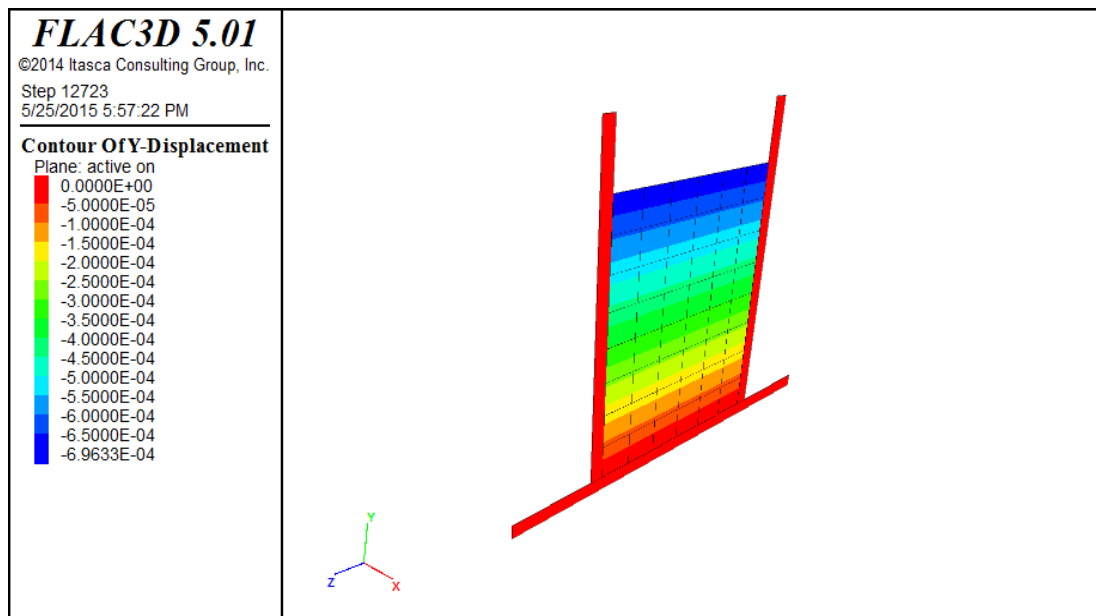


Figure 5.14: Settlement in dry sand with $D_r=40\%$ under 10 kPa load under cyclic simple shear strain tests with $\gamma=0.052\%$ (using G_{max} from eqn 5.1).

Equation 5.2 developed for small strain modulus calculation is dependent on effective stress and relative density or SPT number of drops. By considering the equation 5.2, dry sand will have larger shear modulus because of higher effective stress. Unlike the

equation 5.1, settlement for dry sand is smaller in comparison with fully saturated sand as it is mentioned in table 5.1.

$$G_{max}(PSF) = 1000K_{2max}\sqrt{\sigma'_m}(PSF) \quad (5.2)$$

$$K_{2max} = 20(N_1)_{60}^{\frac{1}{3}} \quad (5.3)$$

$$K_{2max} = 20\left(\frac{D_r}{15}\right)^{\frac{2}{3}} \quad (5.4)$$

It should be considered that units of G_{max} and σ'_m are in PSF in above mentioned equation and should be converted to Pa to be used in FLAC^{3D}. (1 PSF = 49 Pa = 0.049 kPa). Figures 5.15 to 5.18 show the settlement of sand under 10 kPa vertical load when equation 5.2 is considered as maximum shear modulus.

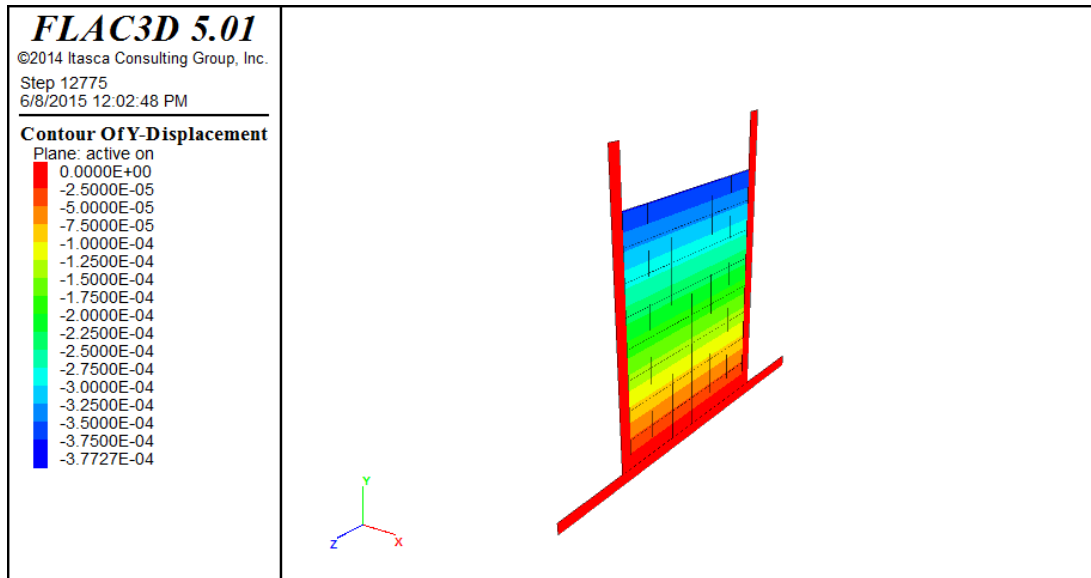


Figure 5.15: Settlement in fully saturated sand with $D_r=20\%$ under 10 kPa load under cyclic simple shear strain tests with $\gamma=0.052\%$ (using G_{max} from eqn 5.2).

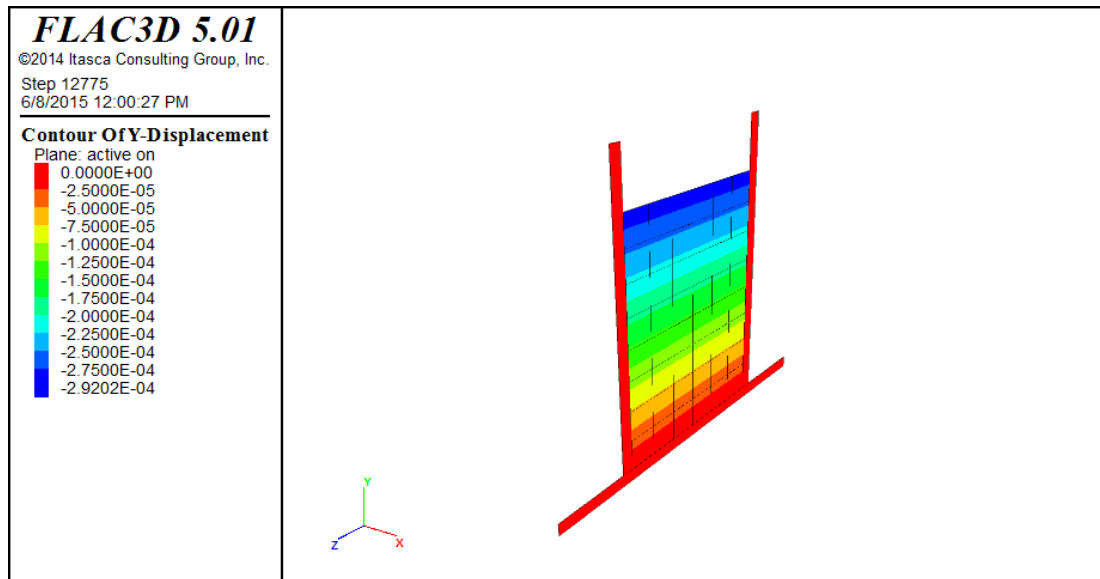


Figure 5.16: Settlement in dry sand with $D_r=20\%$ under 10 kPa load under cyclic simple shear strain tests with $\gamma=0.052\%$ (using G_{max} from eqn 5.2).

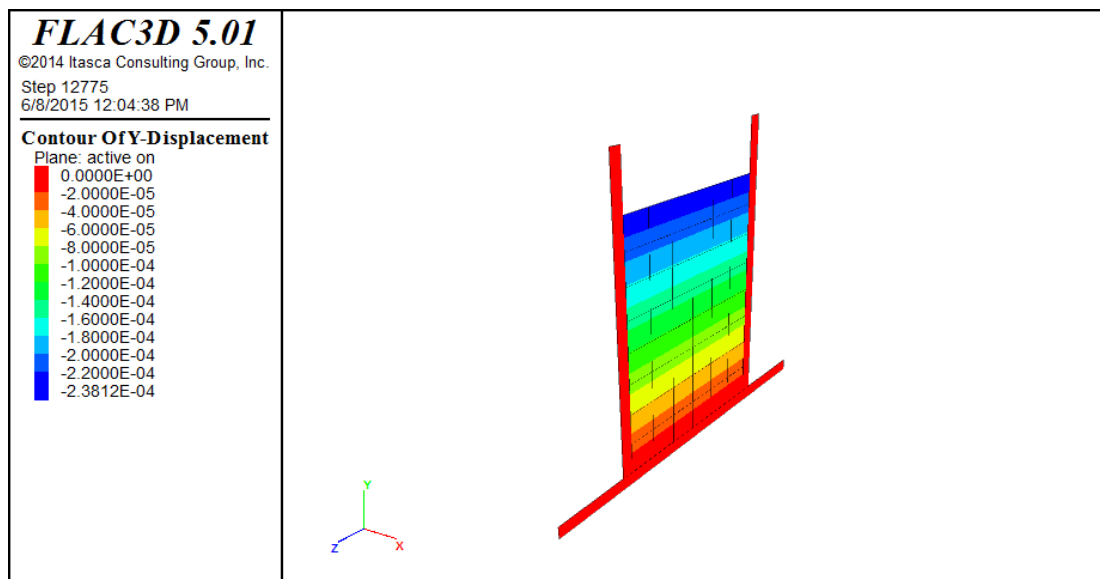


Figure 5.17: Settlement in fully saturated sand with $D_r=40\%$ under 10 kPa load under cyclic simple shear strain tests with $\gamma=0.052\%$ (using G_{max} from eqn 5.2).

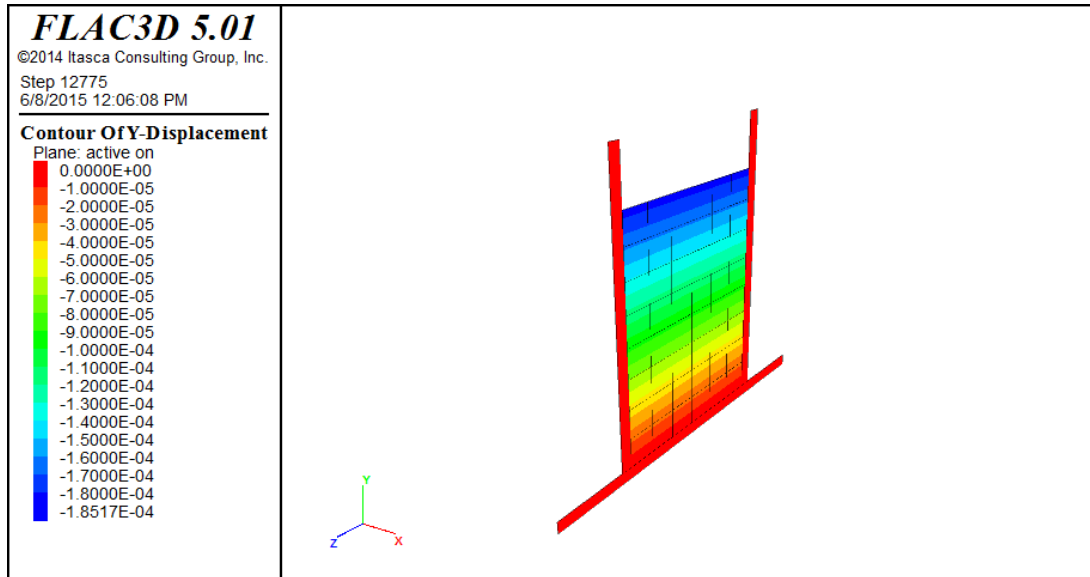


Figure 5.18: Settlement in dry sand with $D_r=40\%$ under 10 kPa under cyclic simple shear strain tests with $\gamma=0.052\%$ (using G_{\max} from eqn 5.2).

Table 5.1 shows the settlements in dry and fully saturated sands for two different relative densities using the two different G_{\max} equations. In the above mentioned figures sand is under 10 kPa vertical stress. As relative density increases, settlement decreases in both fully saturated and dry sands. Also for dry and fully saturated sands, different settlement results are gained from different equations. When equation 5.1 is used as maximum shear modulus, shear modulus for fully saturated sand is higher in comparison with dry sand so settlement is smaller for fully saturated sand. Equation 5.2 which uses effective stress, gives higher shear modulus for dry sand in comparison with saturated sand and smaller settlement as the results.

Table 5.1 : Dynamic settlement of sand in CSSLB under cyclic simple shear strain tests ($\gamma=0.052\%$)

Saturation state	D_r (%)	G_{\max} (Pa) Eqn 1	Settlement (cm) when $G_{\max} = \rho \cdot V_s^2$	G_{\max} (Pa) Eqn 2	Settlement (cm) when $G_{\max} = 1000K_{2\max}\sqrt{\sigma'_m}$
Fully Sat	20	3.8×10^7	0.08	7×10^7	0.038
Dry	20	3×10^7	0.1	8×10^8	0.029
Fully Sat	40	7×10^7	0.055	8.5×10^7	0.024
Dry	40	5.6×10^7	0.07	10.1×10^7	0.0185

Equation 5.2 seem to give more logical results for sand settlement. This equation is recommended for settlement analysis.

5.2 Liquefaction Analysis Results

In this section, the liquefaction analysis results of the numerical model preformed using FINN model built-in in FLAC^{3D} are presented. The results are compared with the experimental results by Eseller-Bayat (2009) and direct and/or simple shear tests results by other authors for higher effective stresses. Code that is used for liquefaction numerical analysis is mentioned as Appendix C.

5.2.1 Comparison of experimental and numerical model results for fully saturated sand

A series of cyclic simple shear tests were performed in specimens prepared in CSSLB box by Eseller-Bayat (2009). Loose to very dense sand specimens were tested under shear strain levels ranging from 0.01% to 0.2%. Pore pressure transducers (PPTs) were calibrated and inserted in the CSSLB through the instrumentation holes on the side walls in the center of the specimen at three different depths. Fully saturated sand specimens were prepared in the CSSLB through wet pluviation technique with Ottawa sand. With wet pluviation technique, loosest condition can be obtained with relative density of around 20%. Eseller-Bayat observe $\gamma=0.005\%$ as threshold shear strain for liquefaction in experimental setup. Figure 5.19 which shows the pore pressure ratio generation for sand with $D_r=60\%$ under $\gamma=0.005\%$, confirm the threshold strain considered by Eseller-Bayat. Results of numerical model and experimental setup are compared graphically in figure 5.20 and 5.21 for sands with $D_r=31\%$ and $D_r=62\%$ when $\sigma'_v=2.4$ kPa and $\gamma=0.0525\%$. As seen in the figures, liquefaction of fully saturated sand specimen was achieved ($r_u=1$) and number of cycles to liquefaction (N_L), which is an important parameter describing the resistance of fully saturated sand to liquefaction, in numerical modelling and experimental setup are fitted well. Comparison of numerical model and experimental results for other tests is presented in Appendix A. For total of 18 tests, number of cycles to liquefaction N_L values were close to each other confirming that the numerical model of CSSLB specimens developed in FLAC^{3D} is accurately simulated the cyclic simple shear tests.

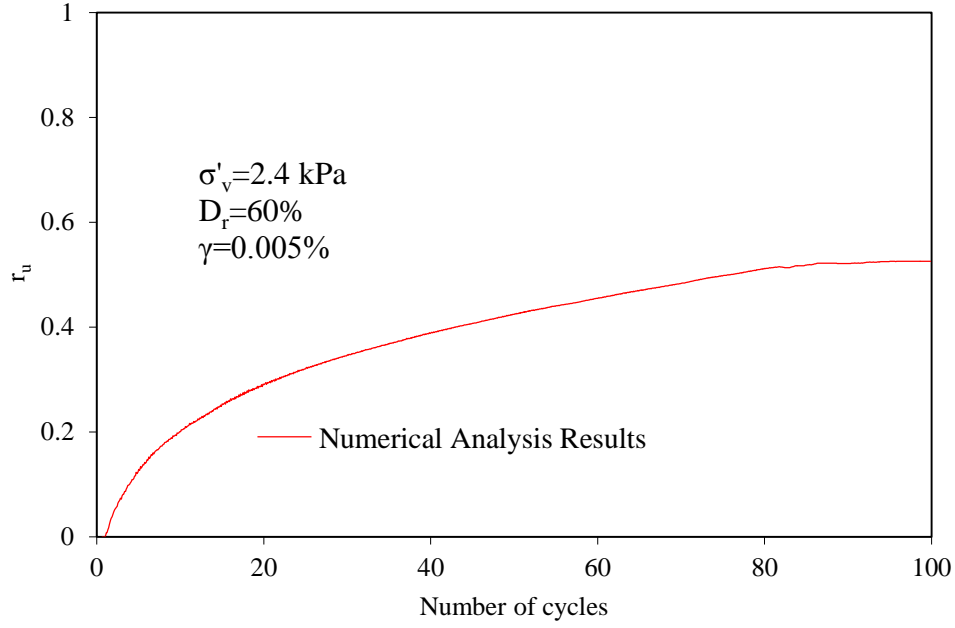


Figure 5.19: Excess pore water pressure generations in numerical analysis when $\sigma'_v = 2.4$ kPa, $D_r = 60\%$ and $\gamma = 0.005\%$.

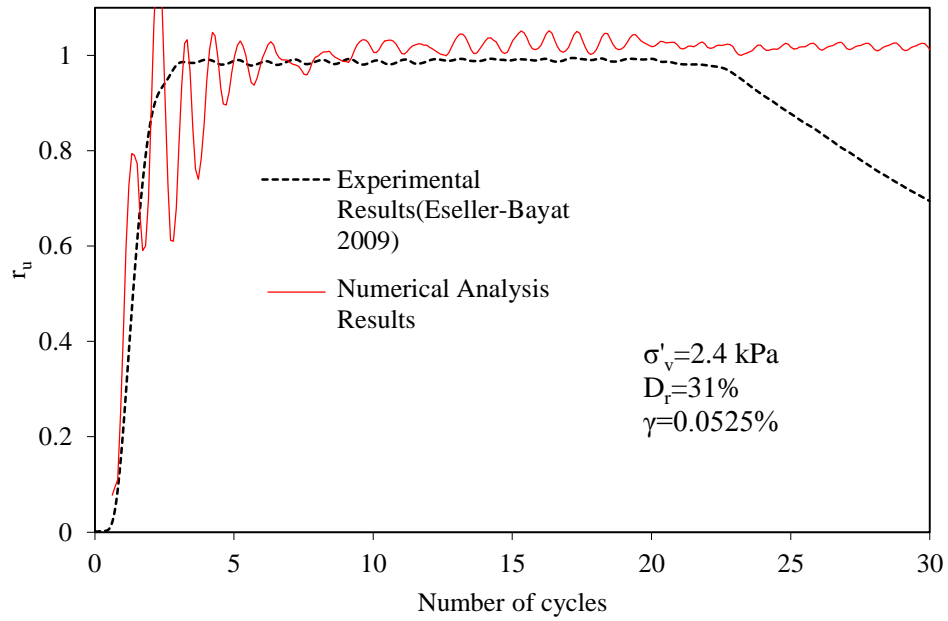


Figure 5.20: Comparison of excess pore water pressure generations in numerical analysis and experimental tests when $\sigma'_v = 2.4$ kPa, $D_r = 31\%$ and $\gamma = 0.0525\%$.

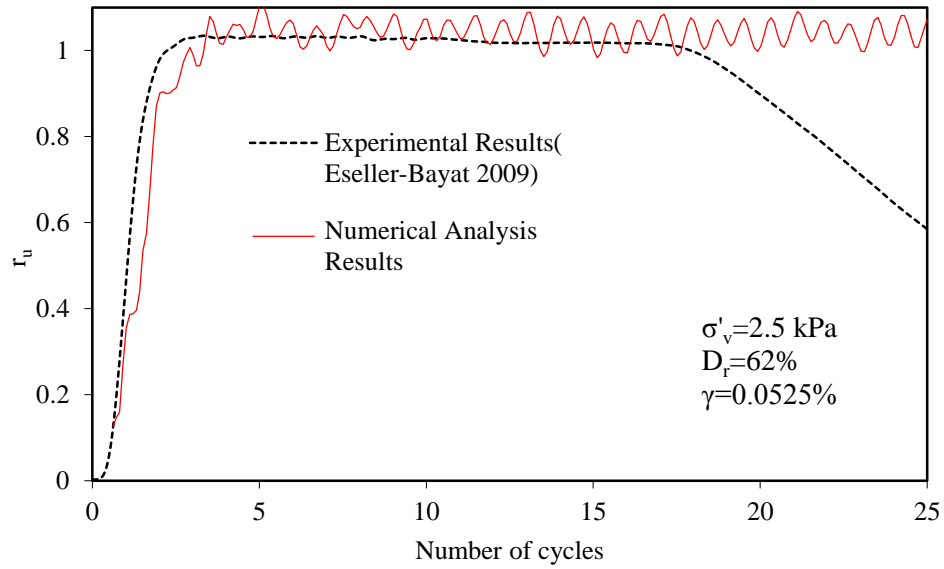


Figure 5.21: Comparison of excess pore water pressure generations in numerical analysis and experimental tests when $\sigma'_v=2.5$ kPa, $D_r=62\%$ and $\gamma=0.0525\%$..

One disadvantage of CSSLB setup on shaking table was the limitation in testing specimens under higher effective stresses. The maximum effective stress in CSLLB was 2.5 kPa without load and 9 kPa by adding lead weights on top of the specimen. Therefore, one of the primary objectives of this research was after confirming the proper numerical model, the results were obtained at higher effective stresses. The numerical results were compared with the experimental data in the literature obtained from cyclic direct simple shear test (CDSS) for higher effective stress. Hazirbaba et al. considered the effect of effective stress on number of cycles necessary to reach liquefaction (N_L) with cyclic direct simple shear test (CDSS), which is different than CSSLB, however which applies simple shear at higher effective stresses Numerical and experimental results for sand under higher effective stress are close however they don't perfectly fit due to the differences in the testing setup. Figures 5.22 thru 5.25. show the comparison between numerical analysis results and experimental results obtained by Hazirbaba.

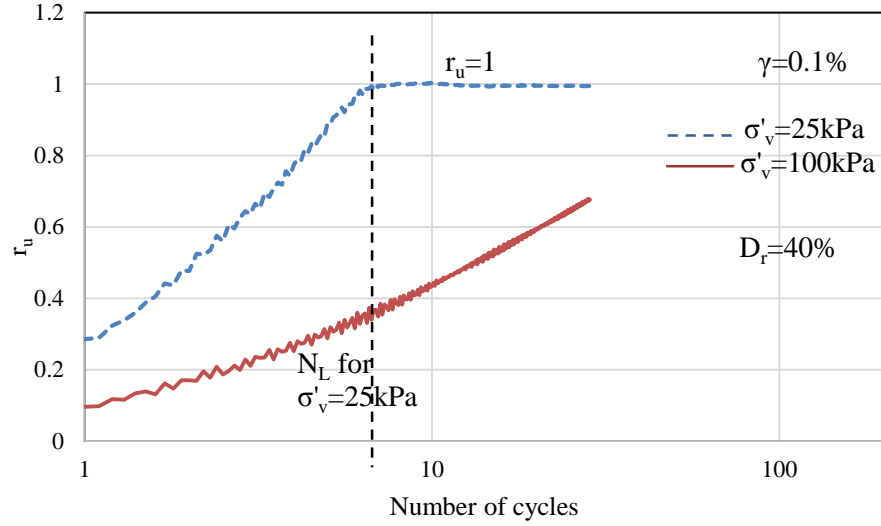


Figure 5.22: r_u vs. Number of cycles when $\gamma=0.1\%$, $D_r=40\%$, $\sigma'_v=25\text{kPa}$ and 100kPa

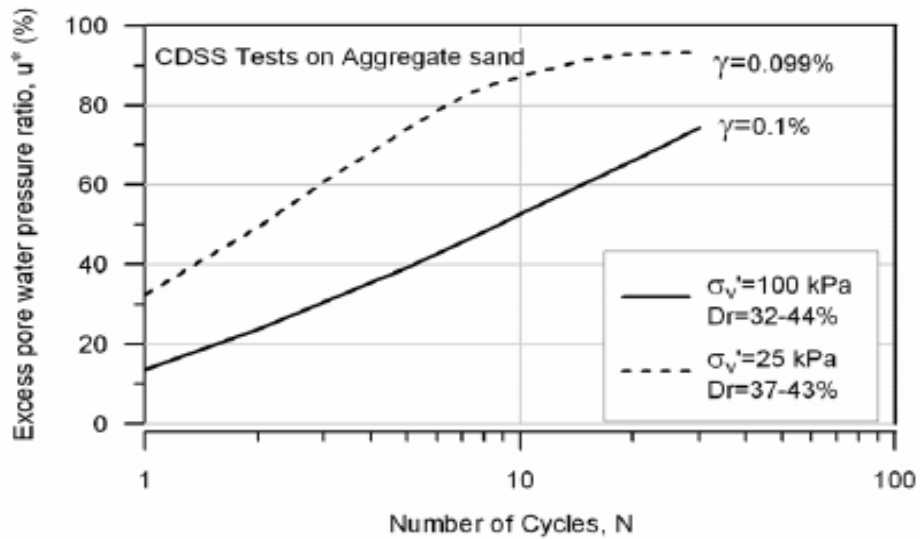


Figure 5.23: Cyclic Direct Shear Strain (CDSS) test results for sand when $\gamma=0.1\%$, D_r is 40% in average and $\sigma'_v = 100\text{ kPa}$ and 25 kPa (Hazirbaba, 2005).

Number of cycles to reach liquefaction (N_L) for $\gamma=0.1\%$ is eight in numerical analysis. For the experimental setup prepared by Hazirbaba, $r_{u\max}$, which is close to one, is observed at twelfth cycle.

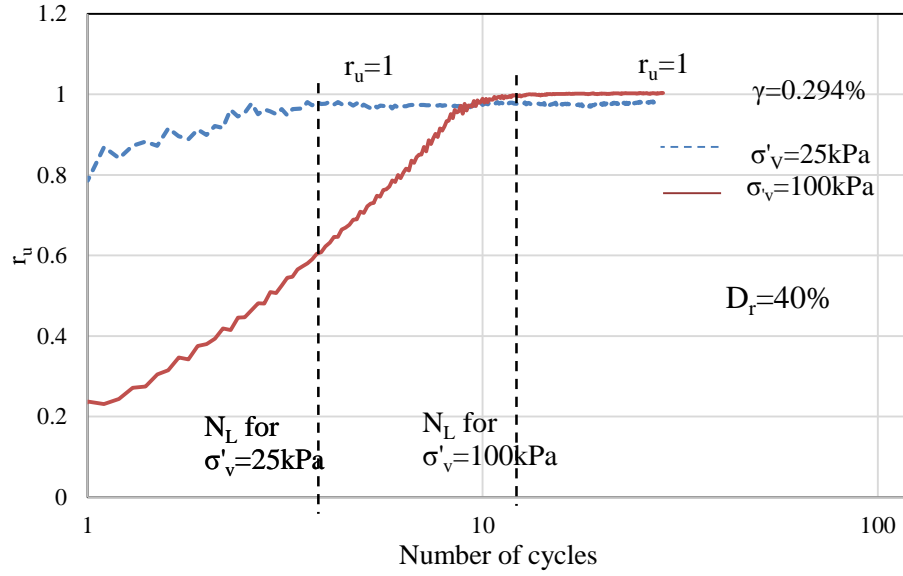


Figure 5.24: r_u vs Number of cycles when $\gamma=0.294\%$, $D_r=40\%$ and $\sigma'_v=25\text{kPa}$ and 100kPa

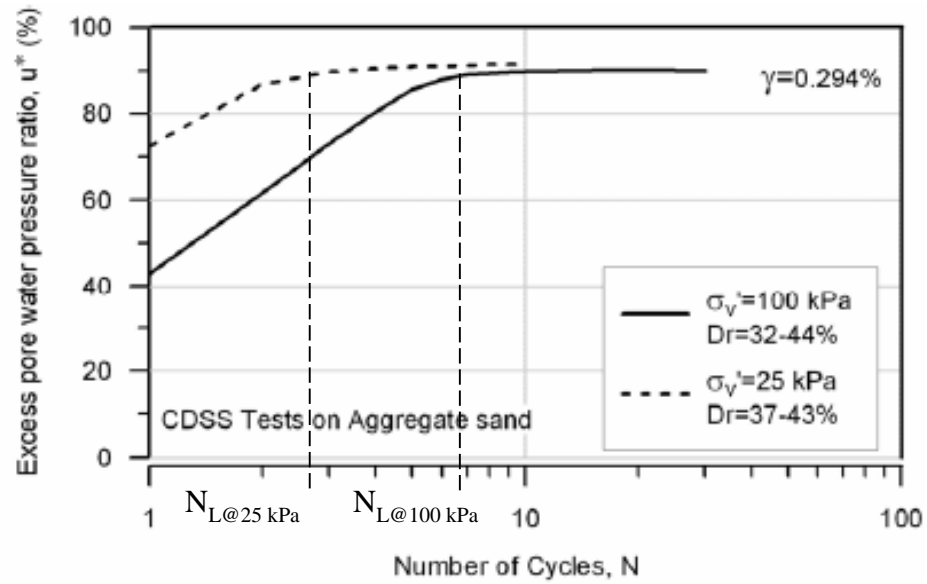


Figure 5.25: Cyclic Direct Shear Strain (CDSS) test results for sand when $\gamma=0.3\%$, D_r is 40% in average and $\sigma'_v = 100\text{ kPa}$ and 25 kPa (Hazirbaba, 2005).

Number of cycles to reach liquefaction (N_L) in numerical analysis for $\gamma=0.3\%$ is three when σ'_v is 25kPa and approximately ten when σ'_v is 100kPa. In the experimental setup, $r_{u\max}$, which is close to one, is observed at second cycle when σ'_v is 25kPa and seventh cycle when σ'_v is 100kPa. Numerical analysis results do not match completely with experimental test results, but by considering the difference between cyclic simple shear strain test, which is used in numerical modelling, and cyclic direct shear strain setup,

which is used by Hazirbaba, numerical results seems to be acceptable and results of numerical model can be used for sand under high effective stress.

5.2.2 Settlement of sand due to liquefaction

After liquefaction occurs, excess pore water pressure dissipates and settlement occurs in the sand, that can be named as post liquefaction reconsolidation settlement. If all the excess pore water pressure dissipates, post liquefaction reconsolidation settlement will be equivalent to sand settlement under drained conditions. Post liquefaction settlement can be calculated by multiplying the volumetric strain by the height of the specimen, which is 40cm (by accepting the area remains the same). The liquefaction-induced settlement can't be achieved in the analysis outputs in FLAC^{3D}, since the analysis is performed without flow (undrained). The liquefaction-induced settlement is calculated here using the volumetric strain equation defined by Byrne (equation 2.12), where the incremental drained volumetric strain $\Delta\epsilon_{vd}$ per half cycle is related to the shear strain amplitude (γ) and the total drained volumetric strain (ϵ_{vd}). The Sum of the volumetric strain increments in all the half-cycles until N_L gives the total volumetric strain.

Volumetric strain calculations are performed for different relative densities and shear strain amplitudes. The following shows the calculation steps for $D_r=40\%$ and $\gamma=0.1\%$.

$$C_1^c = 7600(D_r)^{-2.5} = 7600(40)^{-2.5} = 0.45$$

$$C_1 = \frac{C_1^c}{2} = 0.23$$

$$C_2 = \frac{0.4}{C_1^c} = 0.89$$

At the first step ϵ_{vd} is considered zero.

$$\Delta\epsilon_{vd} = \gamma C_1 e^{\left(-C_2 \left(\frac{\epsilon_{vd}}{\gamma}\right)\right)} = 0.001 * 0.23 * e^{\left(-0.89 \left(\frac{0}{0.001}\right)\right)} = 0.00023$$

In the next step ϵ_{vd} is 0.00023. At the end of N_L Total volumetric strain is obtained by equation 5.5.

$$\epsilon_{vd} = \sum_{i=1}^{2N_L} (\Delta\epsilon_{vd})_i \quad (5.5)$$

One approach was developed by Ishihara and Yoshimine (1992), who observed that the volumetric strains that occur during post-liquefaction reconsolidation of sand samples were directly related to the maximum shear strains that developed during undrained cyclic loading and to the initial relative density of the sand. Figure 5.19 shows the relationship between post liquefaction volumetric strain and maximum shear strain during undrained loading of sand. The recommended relationships can be reasonably approximated by using the equation 5.6 (Yoshimine et al. 2006).

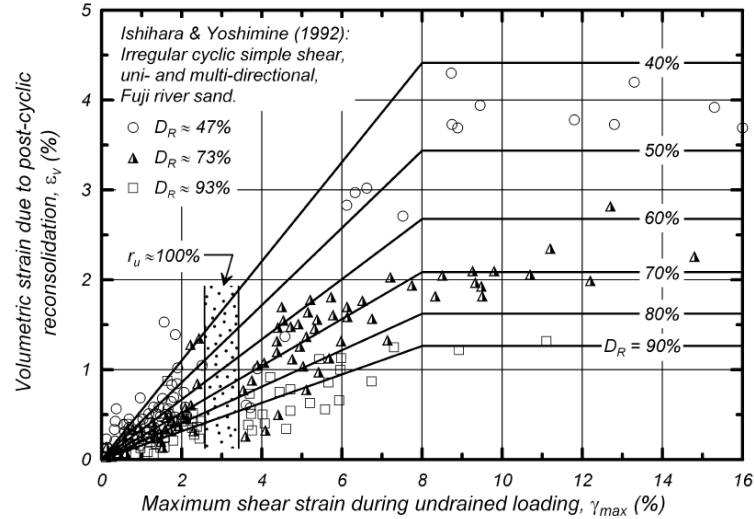


Figure 5.26: Relationship between post liquefaction volumetric strain and maximum shear strain during undrained loading of sand (Ishihara, Yoshimine 1992)

$$\varepsilon_v = 1.5 * \exp(-2.5 * D_r) * \min(0.08, \gamma_{\max}) \quad (5.6)$$

Table 5.2 shows the comparison of volumetric strains obtained from the equations by Byrne and by Ishihara and Yoshimine. Liquefaction-induced settlement of sand is also presented. The results demonstrate that the volumetric strains obtained by Byrne equation are usually higher than the ones obtained from the equation 5.6. This difference may be contributed to the empirical uncertainty existing in both formulations. Also, Byrne equation can be only applied for uniform shear strain levels whereas the equation 5.6 is obtained from irregular cyclic simple shear.

Table 5.2 : Volumetric strain for different γ and D_r .

$\gamma(\%)$	$D_r(\%)$	ε_{vd} from Byrne equation	ε_v from Ishihara equation	Settlement from Byrne equation (cm)
0.052	40	0.0009	0.00028	0.036
0.1	40	0.0013	0.00055	0.052
0.2	40	0.0019	0.0011	0.076
0.052	60	0.00038	0.00017	0.0152
0.1	60	0.0005	0.00033	0.02
0.2	60	0.0011	0.00067	0.044

5.2.3 Liquefaction analysis of fully saturated sand at high effective stresses

Liquefaction analysis was performed in fully saturated sand specimens in CSSLB under several cyclic simple shear strain amplitudes, at loose and dense states under high effective stresses. High effective stresses were obtained in the numerical CSSLB model by applying vertical load by using APPLY command. Then, the formulation developed to predict N_L for fully saturated sands by Eseller-Bayat (2009) using limited experimental data is modified here by using the numerical analysis results.

The second goal of this study is also to improve the number of cycles to maximum r_u (N_{max}) in RuPSS model. In RuPSS model, N_{max} was obtained from the shaking table tests applied on partially saturated sand specimens prepared in CSSLB at limited effective stresses. A normalized N_{max}/N_L function was obtained for $\sigma'_v = 2.5$ kPa (equation 2.18). Due to the lack of data, N_{max} at high effective stresses were estimated by using the normalized function and N_L formulation. Therefore when N_L formulation is modified with the numerical analysis results, the RuPSS model will be also modified by improving the N_{max} estimation.

5.2.3.1 Numerical model results under high effective stress

Numerical results of the sand behavior under higher effective stress in CSSLB is studied in this part. As it was discussed in section 4.5.1, when r_u reaches to one, effective stress is zero. So by using the diagram that shows σ'_v vs. time, number of cycles to reach liquefaction can be obtained at the point where $\sigma'_v = 0$. It should be noticed that the frequency of the sinusoidal cycle is 10 Hz in all the analysis of this part, so there are 10 cycles in each second. Figures 5.27, 5.28, 5.29 shows the σ'_v vs.

time diagrams for different effective stresses that are obtained from FLAC^{3D} analysis. Numerical model results for other σ'_v , γ and D_r are tabulated in Appendix B.

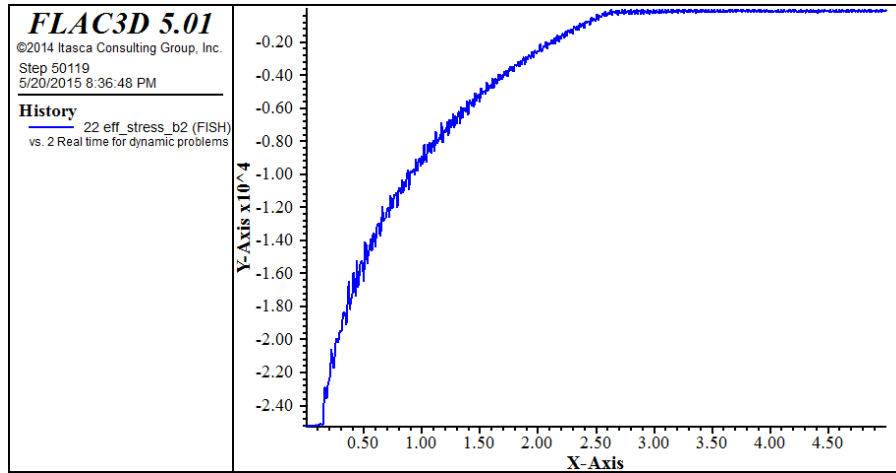


Figure 5.27: σ'_v (Pa) vs. time (sec) when $\sigma'_v = 25\text{kPa}$, $\gamma = 0.05\%$, $D_r = 40\%$

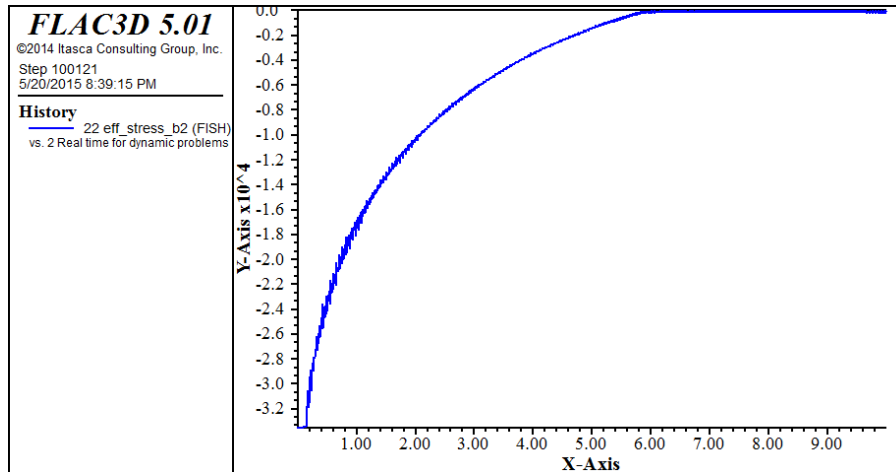


Figure 5.28: σ'_v (Pa) vs. time (sec) when $\sigma'_v = 35\text{kPa}$, $\gamma = 0.05\%$, $D_r = 40\%$

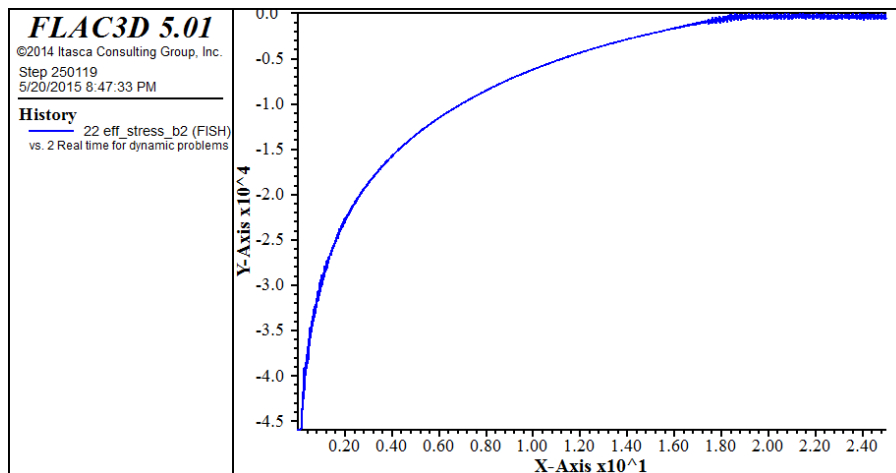


Figure 5.29: σ'_v (Pa) vs. time (sec) when $\sigma'_v = 45\text{kPa}$, $\gamma = 0.05\%$, $D_r = 40\%$

By using the numerical analysis, it is possible to observe N_L at different number of cycles for sand with different relative densities. It is clear that more compact sand, will not liquefy easily, in the other words N_L increases by increasing the D_r . By results of numerical analysis, relationship between N_L and γ , D_r and σ'_v can be prepared more accurately. Figures 5.30, 5.31 and 5.32 show the r_u vs. Number of cycles for sands with different D_r at specific γ and σ'_v . By considering the differences between N_L 's for sand with $D_r=60\%$ and $D_r=40\%$ and differences between N_L 's for sand with $D_r=40\%$ and $D_r=20\%$ (Figure 5.30, 5.31, 5.32), it can be concluded that the relationship between N_L and D_r is not linear.

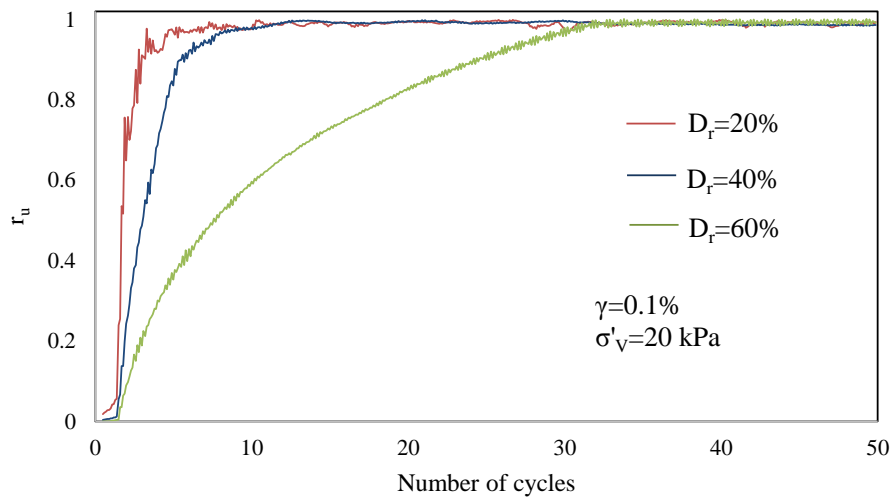


Figure 5.30: Comparison of r_u vs N_L for fully saturated sand with $D_r=20\%$, $D_r=40\%$ and $D_r=60\%$ under $\gamma=0.1\%$ and $\sigma'_v=20$ kPa

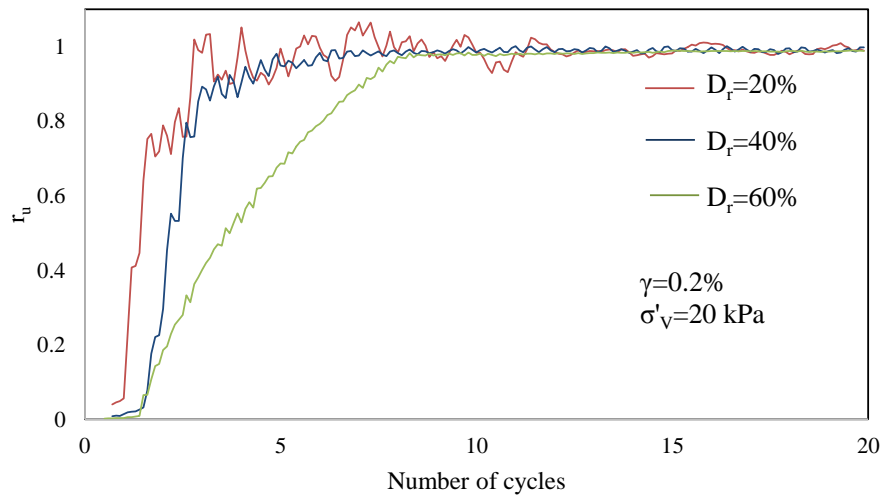


Figure 5.31: Comparison of r_u vs N_L for fully saturated sand with $D_r=20\%$, $D_r=40\%$ and $D_r=60\%$ under $\gamma=0.2\%$ and $\sigma'_v=20$ kPa.

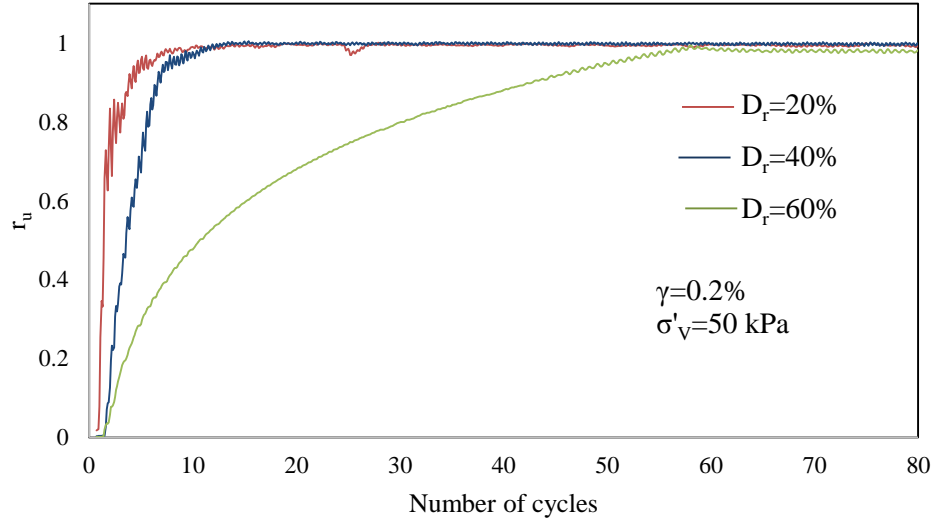


Figure 5.32: Comparison of r_u vs N_L for fully saturated sand with $D_r=20\%$, $D_r=40\%$ and $D_r=60\%$ under $\gamma=0.2\%$ and $\sigma'_v=50$ kPa.

Figures 5.33, 5.34, 5.35 shows the relationship between N_L and σ'_v at different shear strains and a specific D_r . As it can be inferred from the figures, for a specific γ , N_L increases more rapidly in particular σ'_v . Relationship between them seems to be exponential. All these figures confirm that, N_L increases faster than σ'_v . This fact confirms the nonlinear relationship between N_L and γ . Eseller–Bayat efforts shows the exponential relationship between N_L and γ .

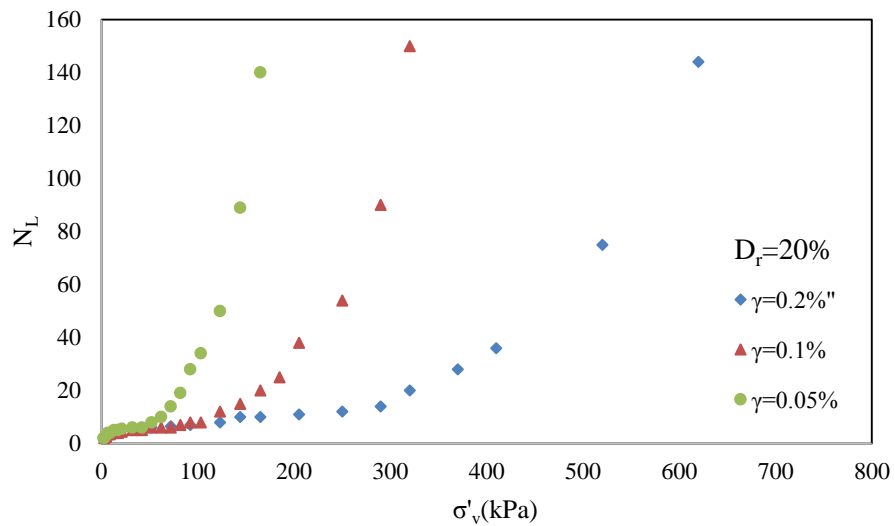


Figure 5.33: N_L vs. σ'_v (kPa) when $D_r=20\%$ and $\gamma=0.05\%$, $\gamma=0.1\%$, $\gamma=0.2\%$.

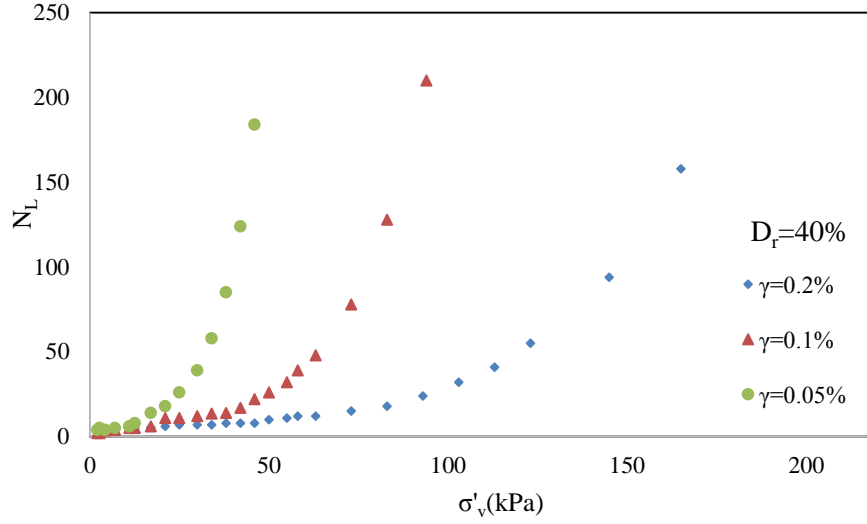


Figure 5.34: N_L vs. σ'_v (kPa) when $D_r=40\%$ and $\gamma=0.05\%$, $\gamma=0.1\%$, $\gamma=0.2\%$.

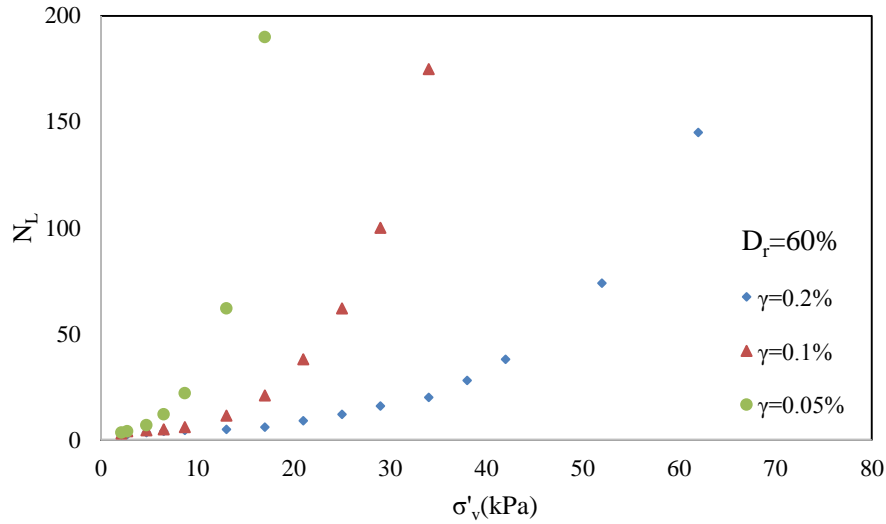


Figure 5.35: N_L vs. σ'_v (kPa) when $D_r=60\%$ and $\gamma=0.05\%$, $\gamma=0.1\%$, $\gamma=0.2\%$.

Figures 5.36, 5.37, 5.38 show the relationship between N_L and σ'_v at different relative densities in a specific γ . Higher cycles are required to reach liquefaction for sands with higher D_r .

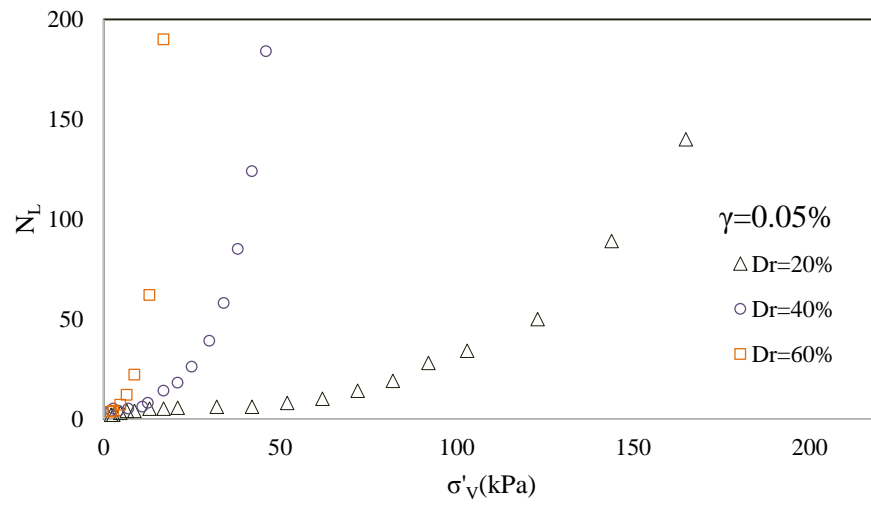


Figure 5.36: N_L vs. σ'_v (kPa) when $\gamma=0.05\%$ and $D_r=20\%$, $D_r=40\%$, $D_r=60\%$.

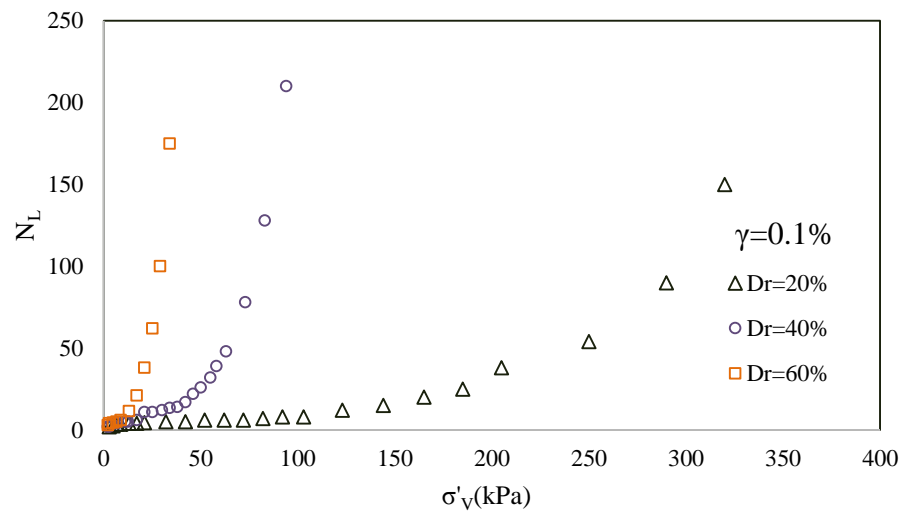


Figure 5.37: N_L vs. σ'_v (kPa) when $\gamma=0.1\%$ and $D_r=20\%$, $D_r=40\%$, $D_r=60\%$.

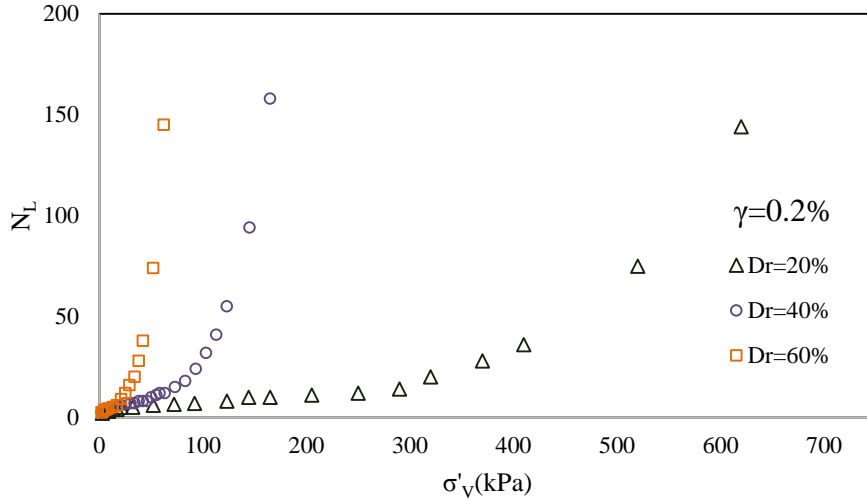


Figure 5.38: N_L vs. σ'_v (kPa) when $\gamma=0.2\%$ and $D_r=20\%$, $D_r=40\%$, $D_r=60\%$.

5.2.3.2 Empirical formulation for number of cycles to reach liquefaction (N_L)

In CSSLB experimental setup, effective stresses could be applied only up to 9 kPa. Eseller-Bayat (2009) used extrapolation for finding a relationship between N_L and σ'_v . Many researchers have investigated the effect of initial effective stress on number of cycles to initial liquefaction. The effect of effective stress on N_L was determined using the experimental data from strain based liquefaction tests available in the literature (Dobry et al. 1982, Hazirbaba et al. 2005, Chang et al. 2007).

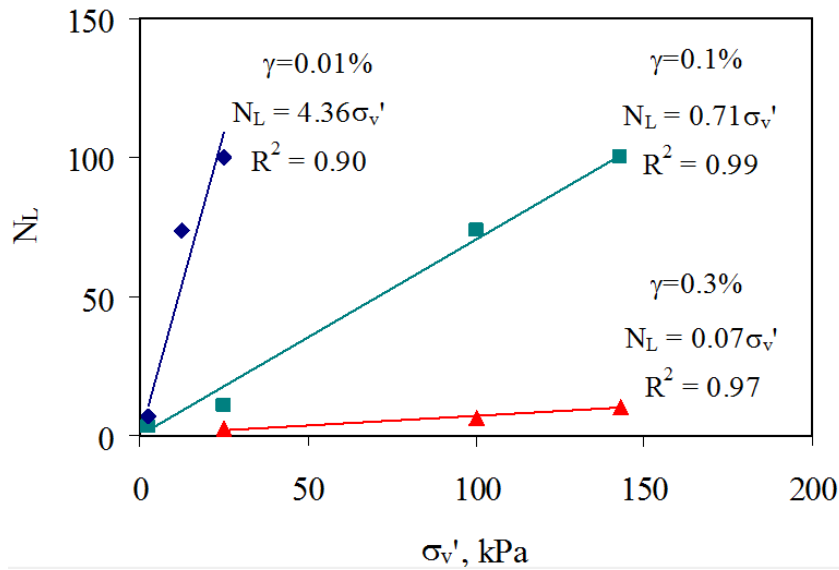


Figure 5.39: N_L as a function of vertical effective stresses for different shear strains for $D_r=40\%$ (Eseller-Bayat, 2009).

Figure 5.39 demonstrates a linear relationship between N_L and σ'_v for a specific strain level developed by Eseller-Bayat. This linear relationship is mentioned as equation 5.7 which fits good for all three shear strains.

$$N_L = 5.33 * e^{-2011*\gamma} * \sigma'_v \quad (5.7)$$

FLAC^{3D} analysis results for higher effective stresses are compared with linear equation results in figures 5.40, 5.41, 5.42. FLAC^{3D} results are fitted with linear equation in smaller effective stresses but after a specific σ'_v , N_L increases more rapidly and linear equation and FLAC^{3D} results keep away from each other.

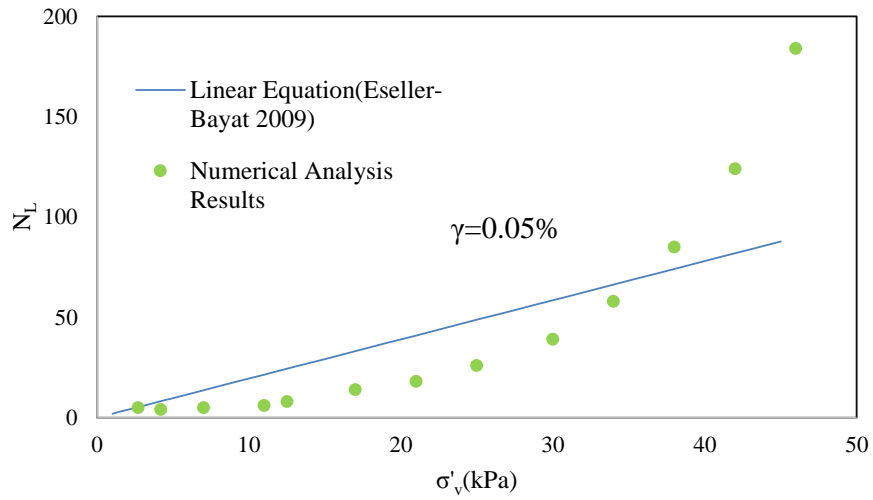


Figure 5.40: Comparison between FLAC^{3D} and linear equation results when $\gamma=0.05\%$ and $D_r=40\%$.

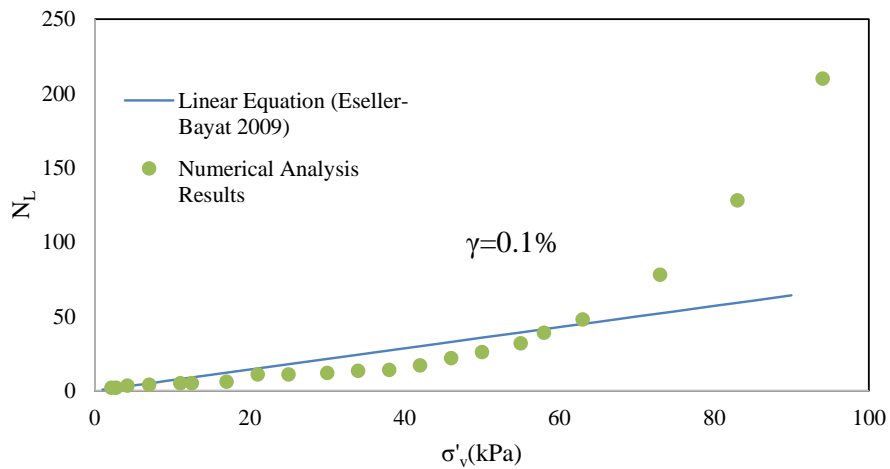


Figure 5.41: Comparison between FLAC^{3D} and linear equation results when $\gamma=0.1\%$ and $D_r=40\%$.

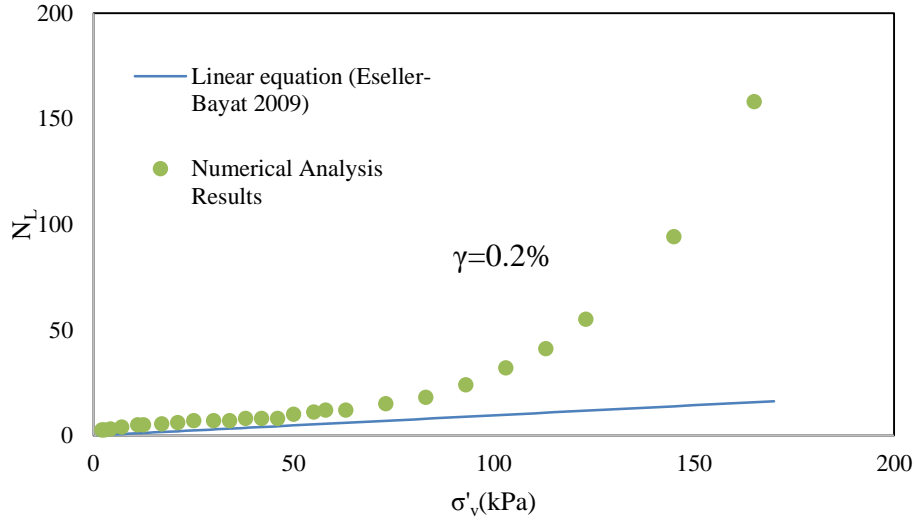


Figure 5.42: Comparision between FLAC^{3D} and linear equation results when $\gamma=0.2\%$ and $D_r=40\%$.

As it is obvious from the above mentioned figures, relationship between number of cycles to reach liquefaction (N_L) and effective stress, for specific shear strain (γ) and relative density (D_r) is not linear. By considering the FLAC^{3D} results, by increasing the σ'_v , number of cycles to reach liquefaction increases exponentially, so it is necessary to modify the N_L equation. Also the equation prepared by Eseller-Bayat was limited only for sand with $D_r=40\%$. New equation is prepared in this research relating N_L to σ'_v , D_r and γ .

Several numerical analysis were preformed in FLAC^{3D} using different results at different σ'_v , D_r and γ and the N_L results are tabulated in Appendix B. By using CURVE-FITTING tool in MATLAB program, equation 5.6 is developed for relating N_L to D_r , σ'_v and γ .

$$N_L = 2.4 * e^{\frac{0.00035 * D_r^2 * \sigma'_v}{\gamma}} \quad (5.8)$$

By substituting the equation 5.8 in RuPSS model (equation 2.17), new equation for calculating number of cycles necessary to reach maximum excess pore water pressure in partially saturated sands (N_{max}) is introduced. N_{max} becomes as in equation 5.9

$$\frac{N_{max}}{N_L} = (20 * e^{-3r_{u\ max}})$$

$$N_{max} = 48 * e^{\left(\frac{0.00035 * D_r^2 * \sigma'_v}{\gamma} - 3r_{u\ max}\right)} \quad (5.9)$$

where r_{umax} is the maximum pore pressure ratio. For sand with different relative densities at a specific shear strain, results obtained from FLAC^{3D} program is compared with equation 5.8 results in Figures 5.43, 5.45, 5.47. Two factors that are considered for controlling the goodness of fit, are coefficient of determination (R^2) and residuals diagram (ϵ). In statistics, the coefficient of determination, denoted R^2 , is a parameter that indicates how well data fit a model. When R^2 is close to one, regression line perfectly fits the data.

Figures 5.44, 5.46, 5.48 show the residuals taken from statistical analysis between the results of numerical analysis and equation 5.8. These figures confirm goodness of fit, while the residuals are minimal and symmetrically distributed around the zero residual.

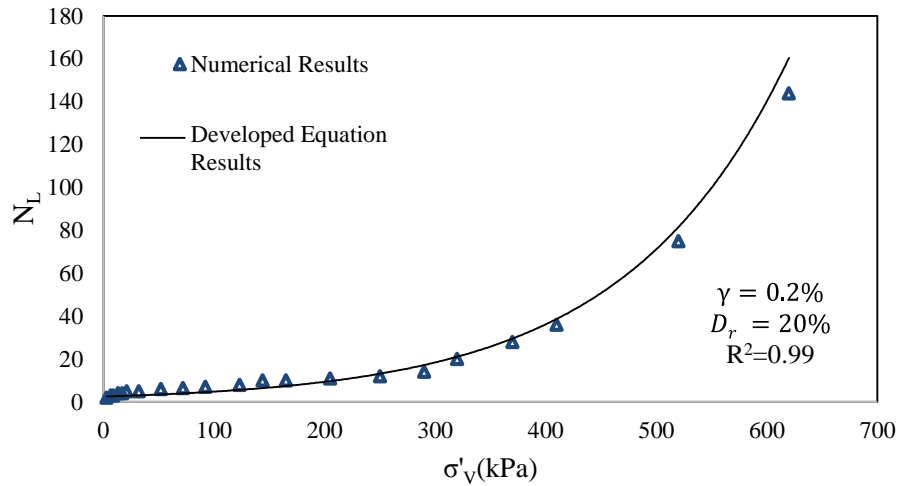


Figure 5.43: Comparison of of the N_L results obtained from FLAC^{3D} and the developed equation for different σ'_v , when $\gamma=0.2\%$ and $D_r=20\%$.

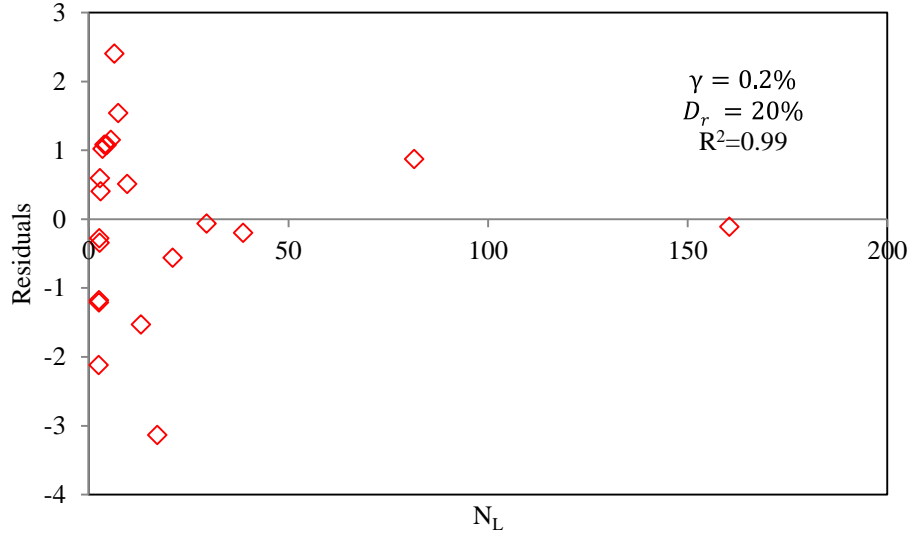


Figure 5.44: Residuals of N_L obtained from FLAC^{3D} analysis and N_L obtained from the developed equation for different σ'_v , when $\gamma=0.2\%$ and $D_r=20\%$.

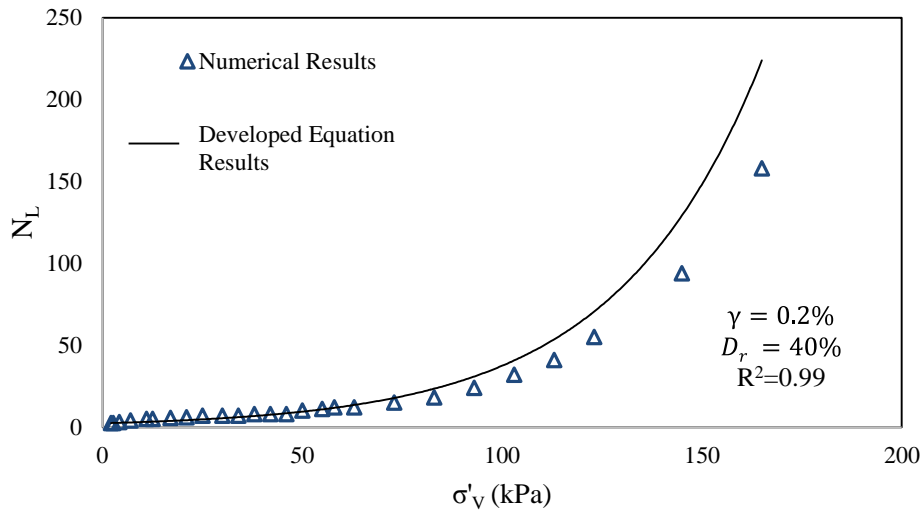


Figure 5.45: Comparison of N_L results obtained from FLAC^{3D} and the developed equation for different σ'_v , when $\gamma=0.2\%$ and $D_r=40\%$.

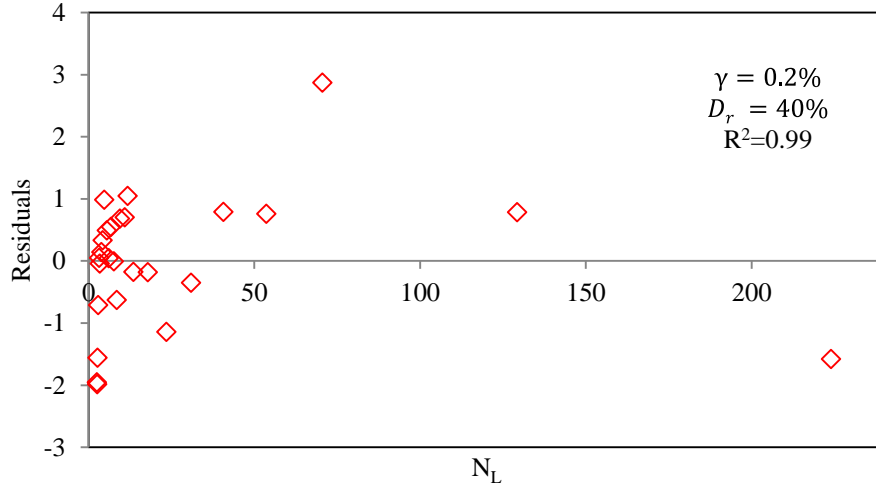


Figure 5.46: Residuals of the NL results obtained from FLAC^{3D} and the developed equation for different σ'_v , when $\gamma=0.2\%$ and $D_r=40\%$

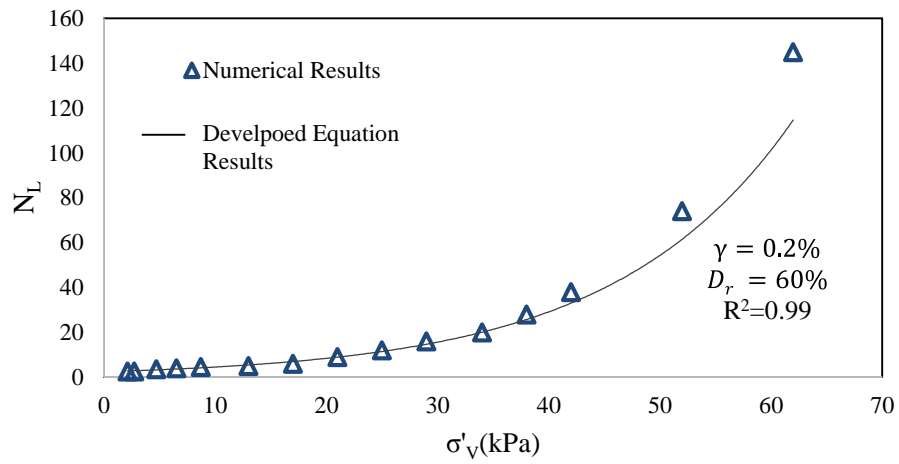


Figure 5.47: Comparison of N_L results obtained from FLAC^{3D} and the developed equation for different σ'_v , when $\gamma=0.2\%$ and $D_r=60\%$.

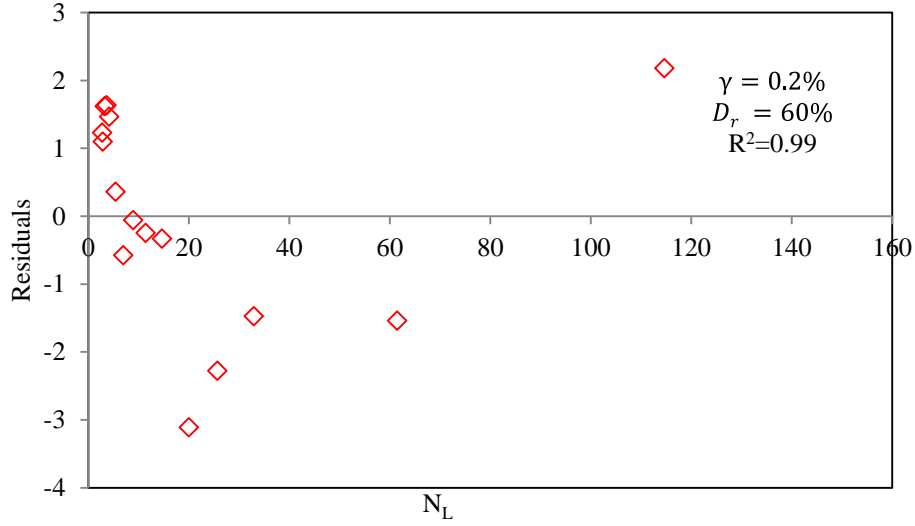


Figure 5.48: Residuals of N_L obtained from FLAC^{3D} analysis and N_L obtained from the developed equation for different σ'_v , when $\gamma=0.2\%$ and $D_r=60\%$.

At the end of this section, linear equation prepared by Eseller-Bayat to correlate N_L with σ'_v and γ is compared with equation 5.8 in figures 5.49, 5.50, 5.51. As it is obvious in figures, linear and exponential equations are good fitted in smaller effective stresses.

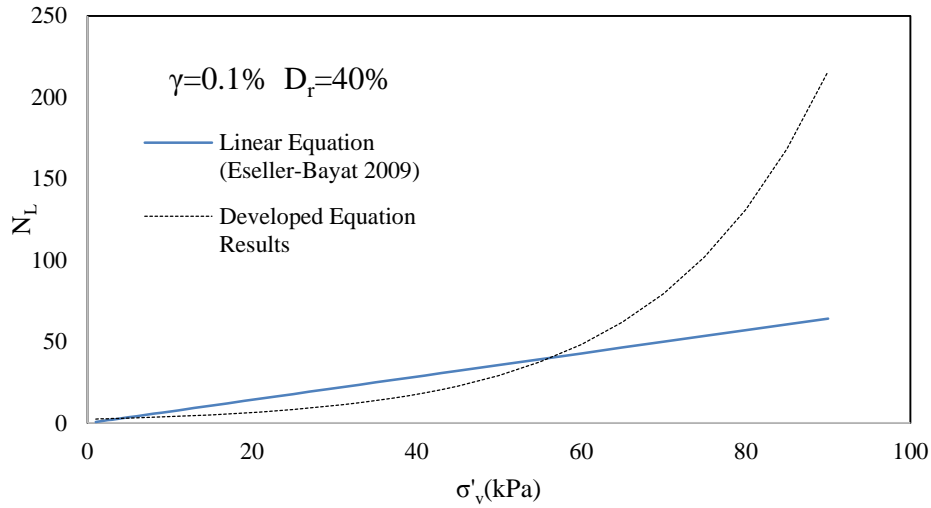


Figure 5.49: Comparison of modified equation and linear equation by Eseller-Bayat (2009), when $\gamma=0.1\%$ and $D_r=40\%$.

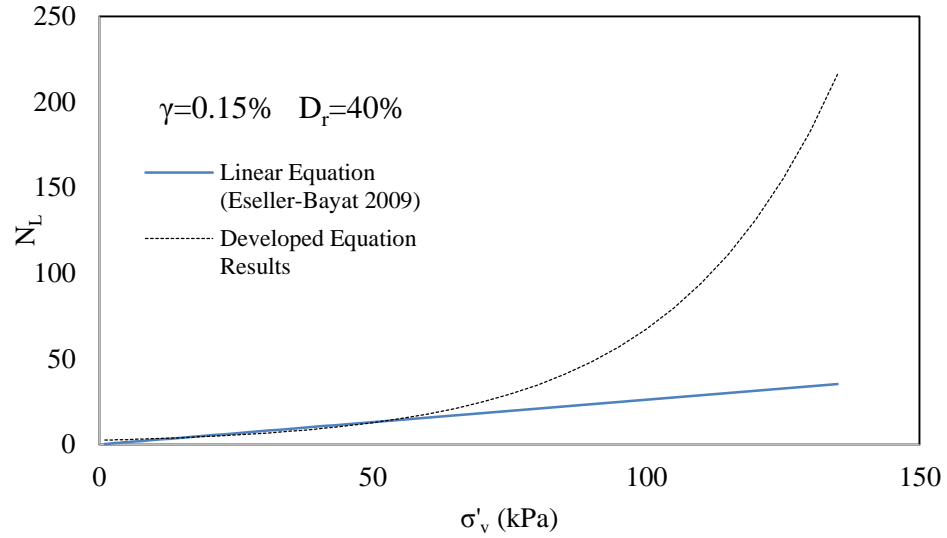


Figure 5.50: Comparison of modified equation and linear equation by Eseller-Bayat (2009), when $\gamma=0.15\%$ and $D_r=40\%$.

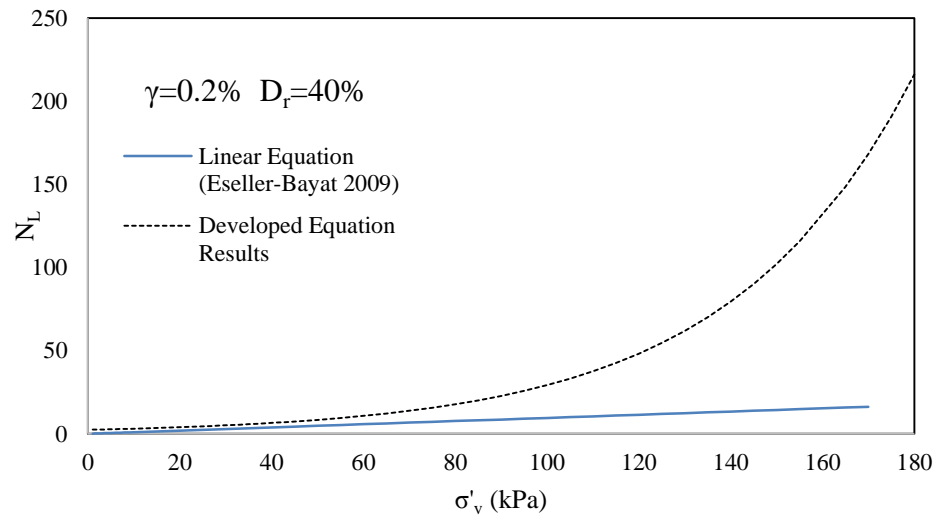


Figure 5.51: Comparison of modified equation and linear equation by Eseller-Bayat (2009), when $\gamma=0.2\%$ and $D_r=40\%$.

5.2.4 Numerical model results for partially saturated sand

After confirming that the numerical model developed in $FLAC^{3D}$ gives reasonable results for fully saturated sands tested in CSSLB under cyclic simple shear strains, attempts are made for performing liquefaction analysis for partially saturated sands. The important issue here is when degree of saturation is entered as $S < 100\%$, $FLAC^{3D}$ don't generate excess pore water pressures. Therefore, the degree of saturation is kept as 100% while the bulk modulus of the fluid in the void is reduced in order to reflect

the compressibility of the water-air mixture. As it was discussed in section 4.5.2., Koning developed an equation for calculating the bulk modulus of air and water mixture. Equation 4.24 is used for numerical modeling of partially saturated sand. As shown in Figure 5.52, 5.53, 5.54 experimental and numerical results do not fit well. Number of cycles to reach $r_{u\max}$ (N_{\max}) in numerical analysis is much higher than the one obtained in shaking table tests. Also pore pressure ratio do not fit in numerical analysis with experimental setup. Pore pressure ratio in numerical model is smaller than pore pressure ratio of experimental setup, when degree of saturation is 84%. For smaller degrees of saturation, pore pressure ratio taken from numerical analysis is bigger than pore the pressure ratio of experimental test.

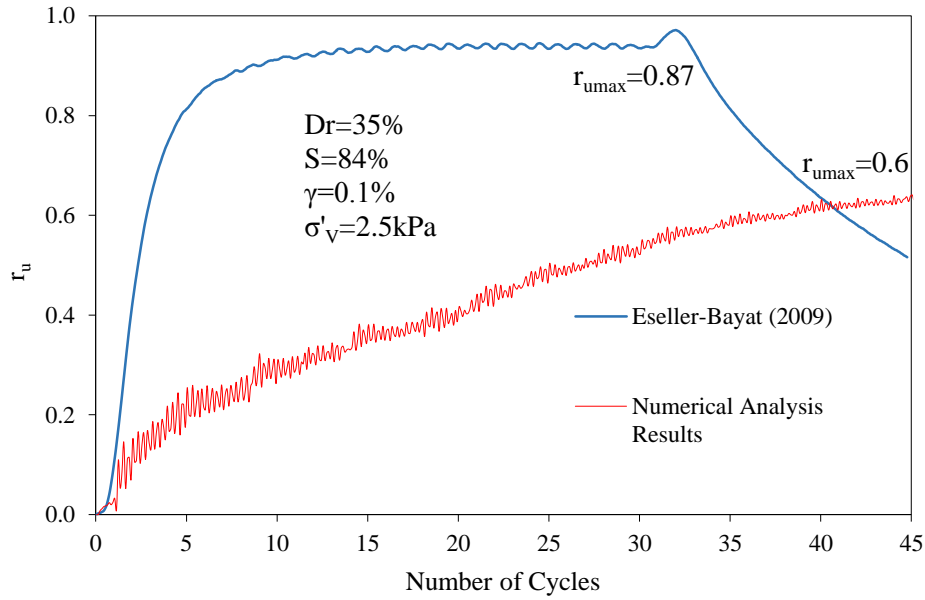


Figure 5.52: r_u vs. Number of cycles for partially saturated sand when $\gamma=0.1\%$, $D_r=35\%$ and $\sigma'_v=2.5$ kPa and $S=84\%$.

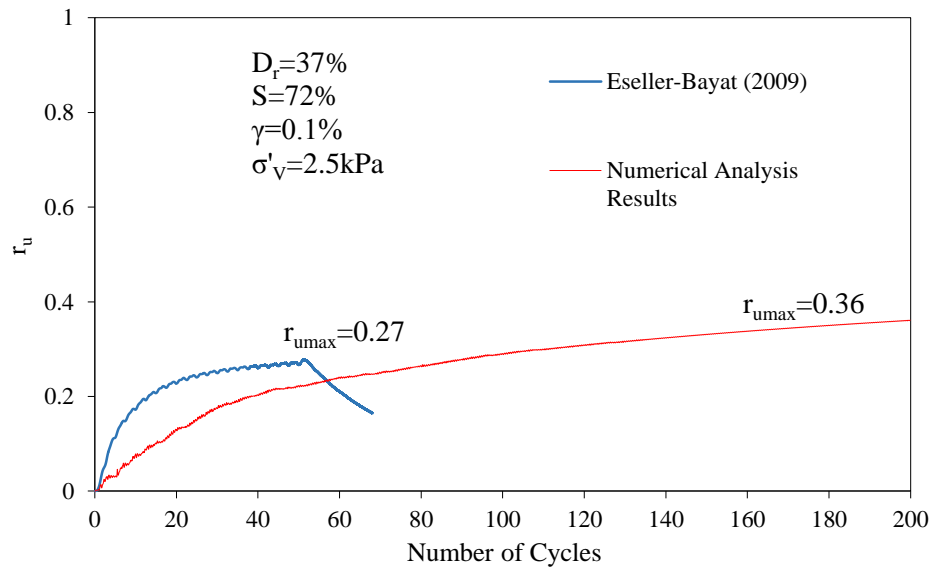


Figure 5.53: r_u vs. Number of cycles for partially saturated sand when $\gamma=0.1\%$, $D_r=37\%$ and $\sigma'_v=2.5$ kPa and $S=72\%$.

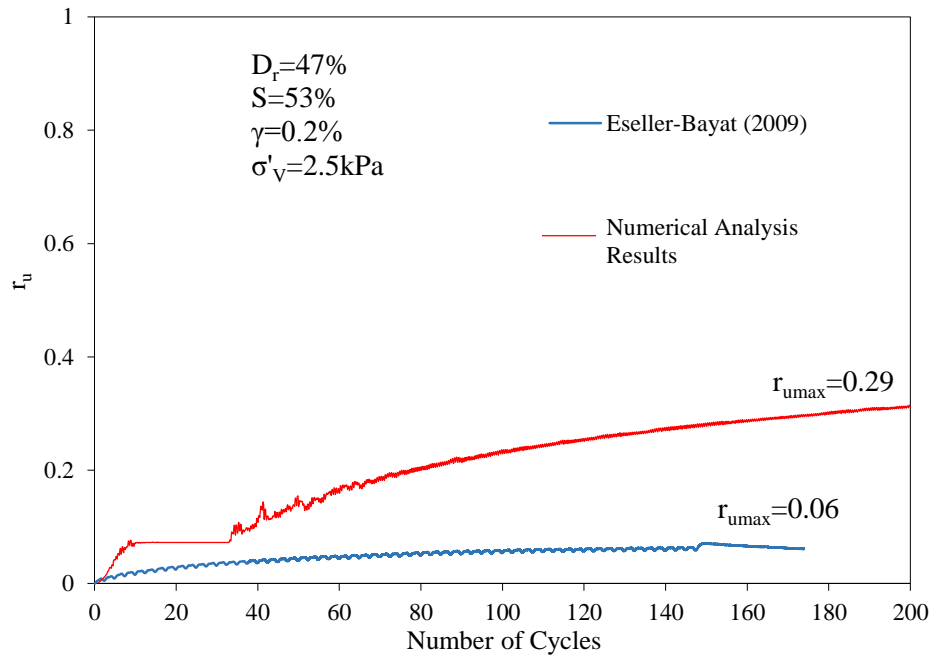


Figure 5.54: r_u vs. Number of cycles for partially saturated sand when $\gamma=0.2\%$, $D_r=47\%$ and $\sigma'_v=2.5$ kPa and $S=53\%$.

The equation developed by Koning is simplified model which formulates the compressibility of air and water mixture in the voids of the sand. It is necessary to do

more effort at this step for numerical modeling of partially saturated sands and use other compressibility formulations. This stage of research can be focused in future for more accurate results for compressibility of air and water mixture. Another analytical model can be developed for considering the bulk modulus of air-water mixture under cyclic condition.

5.3 Numerical Analysis Results for Free-Field Model

In this section, liquefaction analysis is performed in a free-field model to validate the N_L formulation developed for fully saturated sands and to compare the RuPSS model with numerical analysis results for partially saturated sands. In the RuPSS model by Eseller-Bayat was developed. , (for the model to be valid for real problems), proposed a procedure to find equivalent uniform shear trains for irregular earthquake induced shear strains. In the determination of equivalent number of uniform cycles, an equivalent strain (or stress) amplitude also needed to be selected. In Seed et al studies the equivalent amplitude for the irregular earthquake was determined equal to $0.65 \tau_{max}$ (or γ_{max}). Idriss and Sun, 1992 developed a relationship to find the equivalent shear stress (or strain) amplitude by earthquake magnitude, which is mentioned as equation 5.10 and 5.11

$$\gamma_{eqv} = \gamma_{max} * R \quad (5.10)$$

$$R = \frac{M - 1}{10} \quad (5.11)$$

where M is the magnitude of the earthquake. Based on the equation developed by Idriss and Sun the equivalent amplitude for the irregular earthquake with a magnitude M is equal to $\gamma_{eqv} = R * \gamma_{max}$. Figure 5.55 shows the concept of equivalent number of cycles.

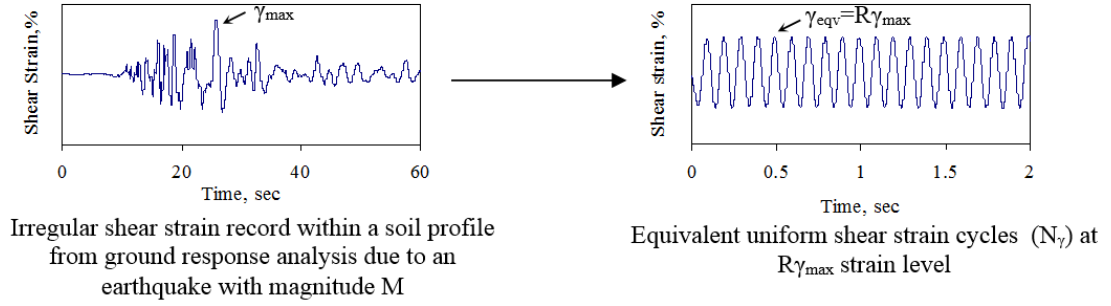


Figure 5.55: Concept of equivalent number of cycles for an earthquake with magnitude M (Eseller-Bayat, 2009).

Seed et al. (1975) determined the equivalent number of uniform stress cycles, at a stress level of $0.65\tau_{\max}$ ($R=0.65$) from acceleration records of past earthquakes but they did not introduce an equation for it.

A fitted equation was represented by Eseller-Bayat by linear regression analysis for this purpose which is mentioned as equation 5.12.

$$N_{eqv} = 0.057e^{0.72M} \text{ for } R=0.65 \quad (5.12)$$

Conversion factor (k), is used for calculation of equivalent number of cycles, when R is not 0.65. Eseller-Bayat introduced relationship (equation 5.13 and 5.14) between conversion factors k and R by using the studies of Astunias and Dobry 1982.

$$k(R) = 0.114 * e^{\left(\frac{1}{R^{1.8}}\right)} \quad (5.13)$$

$$N_{eqv-R} = N_{eqv-R=0.65} * k(R) \quad (5.14)$$

Equation 5.14 can be written as a function of earthquake magnitude (M), which is represented as equation 5.15

$$N_{eqv-M} = N_{eqv-M=7.5} * k(M) \quad (5.15)$$

By considering the N_{eqv-M} as N_γ equation (5.16) is going to be written as

$$N_\gamma = 0.0065 * e^{\left[\left(\frac{10}{M-1}\right)^{1.8} + 0.72M\right]} \quad (5.16)$$

where M is the magnitude of earthquake. Figure 5.56 shows N_γ versus earthquake magnitude M . Dashed lines are N_{eqv} for different R . Since in ground response analysis, equivalent strain amplitude ($R\gamma_{\max}$) is also related to the earthquake magnitude M , the

strain ratio (R) is unique for that magnitude and there is only one equivalent number of uniform strain cycles corresponding to each earthquake magnitude.

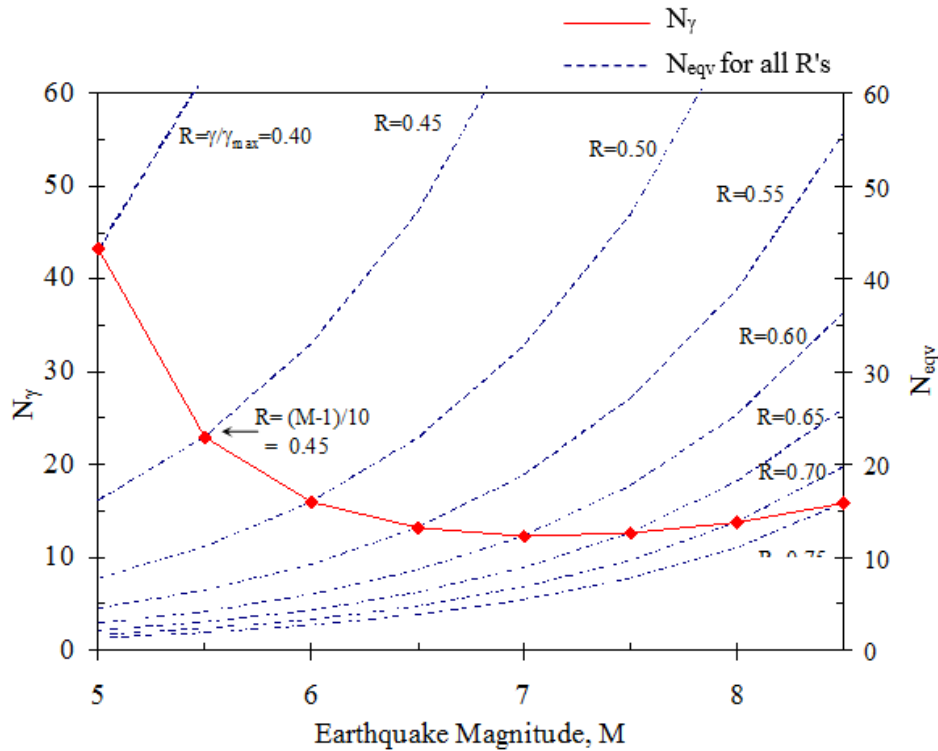


Figure 5.56: Earthquake magnitude (M) vs. N_γ (Eseller-Bayat, 2009).

Northridge earthquake is applied to the field as real earthquake. The 1994 Northridge earthquake occurred on January 17, was centered in Reseda, a neighborhood in the north-central San Fernando Valley region of Los Angeles, California. It had a duration of approximately 20 seconds. The earthquake had magnitude of 6.7, which produced ground acceleration that were the highest ever instrumentally recorded in an urban area in North America. Strong ground motion was felt as far away as Las Vegas, Nevada, about 360 km from the epicenter. The peak ground velocity in this earthquake at the Rinaldi Receiving station was 183 cm/s the fastest peak ground velocity ever recorded.

The free field which is simulated in numerical model has 15 meter depth and 150 meters diameter in lateral directions (figure5.57). It is consist of one sand layer with $D_r=40\%$. Sand parameters that are used as material properties are mentioned in section 4.2.

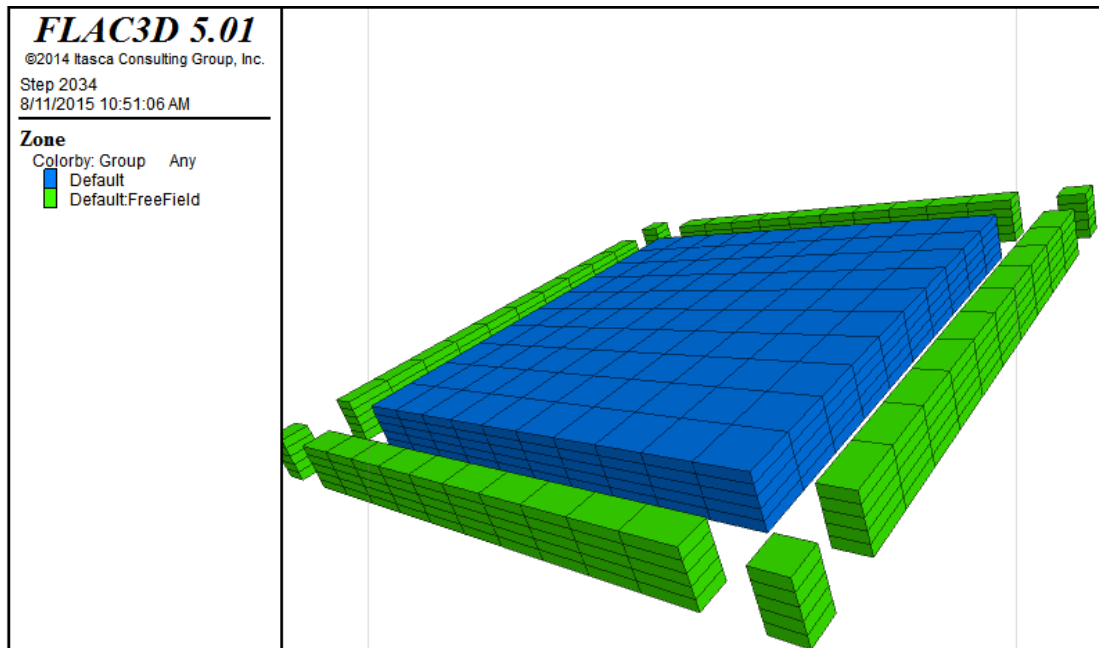


Figure 5.57: Free field model in FLAC^{3D}.

Velocity of the Northridge earthquake is applied at the bottom of the field model in this analysis. Figure 5.58 shows the acceleration, velocity and displacement of Northridge earthquake that are obtained from Seimosignal program.

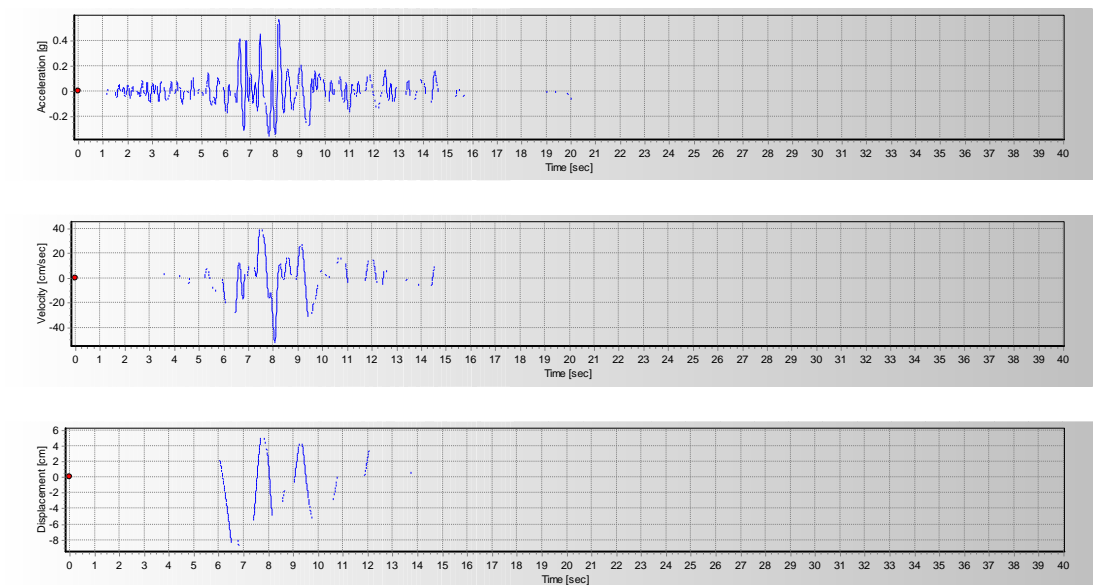


Figure 5.58: Acceleration, Velocity and displacement records of Northridge earthquake from Seimosignal program.

Equivalent uniform cycles can be calculated by the procedure mentioned at first part of this section. Number of cycles in uniform equivalent shear strain cycles is calculated by magnitude of Northridge earthquake using equation 5.16 for M=6.7..

$$N_{\gamma} = 0.0065 * e^{\left[\left(\frac{10}{6.7-1} \right)^{1.8} + 0.72 * (6.7) \right]} = 12.66 \text{ Cycles}$$

By applying the velocity to numerical model, maximum shear strain can be obtained. Shear strain time history is obtained in FLAC^{3D} for each layer. Equivalent shear strain (γ_{eqv}) is calculated for each layer by the equation 5.10, in order to estimate N_L and whether or not the liquefaction occurs in fully saturated sands. Also, γ_{eqv} will be needed to estimate excess pore water pressure ratios from RuPSS model. Figure 5.59 show the displacement of field numerical model due to Northridge Earthquake at H=12m.

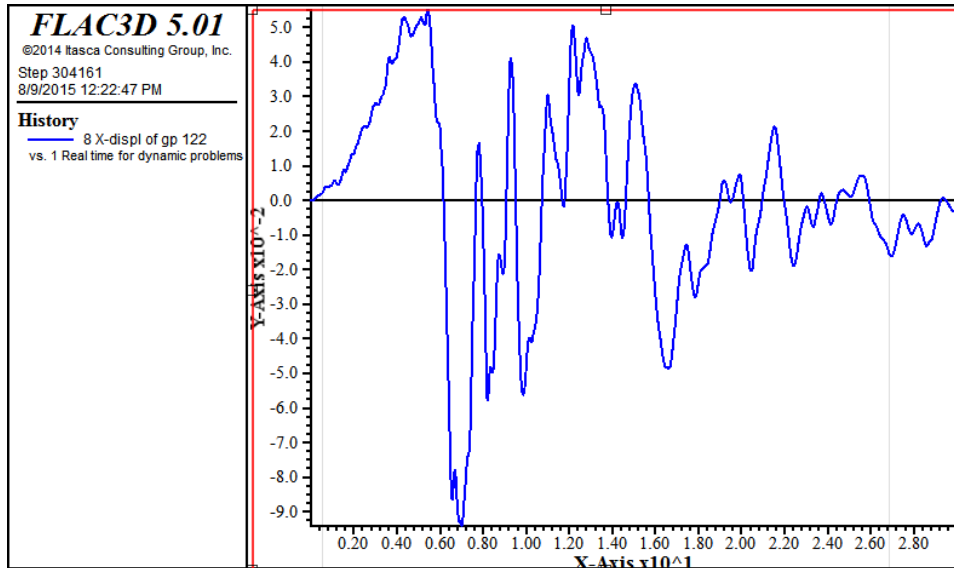


Figure 5.59: Displacement of field numerical model in X direction (m), when accelartion is applied in X-direction (H=12m)

5.3.1 Numerical results for fully saturated sand in free-field

Sand which is used in field numerical model is Ottawa sand with $D_r=40\%$. The field is divided to 5 layers in height and shear strains generated in each layer due to the Northridge earthquake velocity record applied at the bottom.. Maximum shear strain for H=12m is obtained as $1.2 * 10^{-2}$, which is shown in figure 5.60.

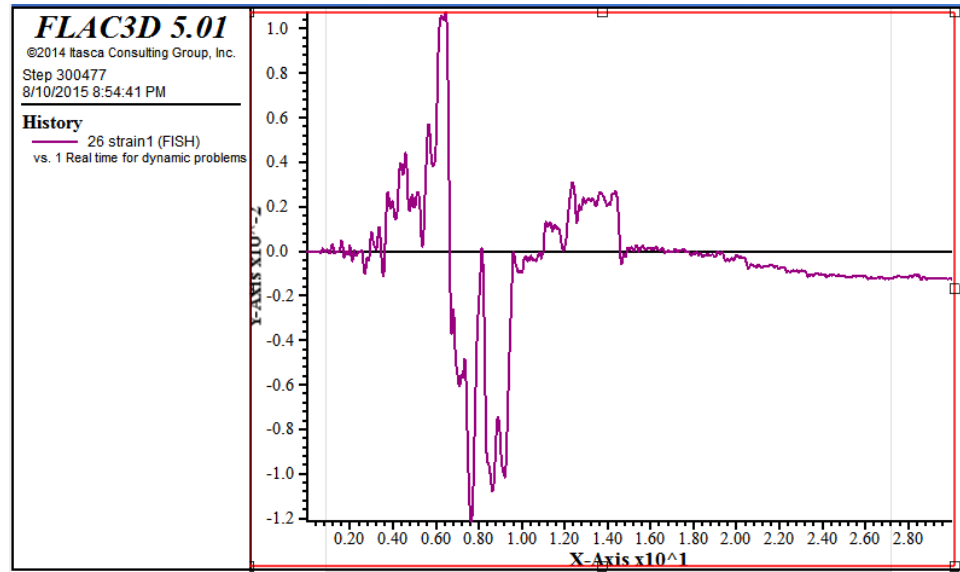


Figure 5.60: Shear strain obtained for H=12m under Northridge earthquake

Maximum shear strains (γ_{max}) and equivalent shear strains (γ_{eqv}) for each layer are calculated as tabulated in Table 5.3. Number of cycles to reach liquefaction (N_L) and equivalent number of cycles (N_γ) are also determined for every layer. For H=12m:

$$R = \frac{M - 1}{10} = \frac{6.7 - 1}{10} = 0.57$$

$$\gamma_{eqv} = \gamma_{max} * R = 1.2 * 10^{-2} * 0.57 = 6.8 * 10^{-3}$$

$$N_L = 2.4 * e^{\frac{0.00035 * Dr^2 * \sigma'_V}{\gamma_{eqv}}} = 2.4 * e^{\frac{0.00035 * 0.4^2 * 110}{6.8 * 10^{-3}}} = 5.93 \text{ Cycles}$$

$$N_\gamma = 0.0065 * e^{\left[\left(\frac{10}{6.7-1} \right)^{1.8} + 0.72 * (6.7) \right]} = 12.66 \text{ Cycles}$$

Table 5.3 : Possibility of liquefaction at different depths for field affected by Northridge earthquake.

H(m)	γ_{max}	γ_{eqv}	N_L (Equation 5.6)	$\frac{N_\gamma}{N_L}$ (if >1 liquefaction occurs)
3	$1 * 10^{-2}$	$0.57 * 10^{-2}$	2.7	4.7
6	$1.1 * 10^{-2}$	$0.63 * 10^{-2}$	3.4	3.7
9	$0.8 * 10^{-2}$	$0.46 * 10^{-2}$	5.2	2.4
12	$1.2 * 10^{-2}$	$0.68 * 10^{-2}$	5.9	2.38

$\frac{N_y}{N_L}$ is bigger than one for all four considered depths. This results show that liquefaction occurs under Northridge earthquake in all considered layers of Ottawa sand. The excess pore water pressure generation at each layer due to Northridge earthquake are computed in FLAC^{3D} and presented in figures 5.61, 5.62, 5.63, 5.64.

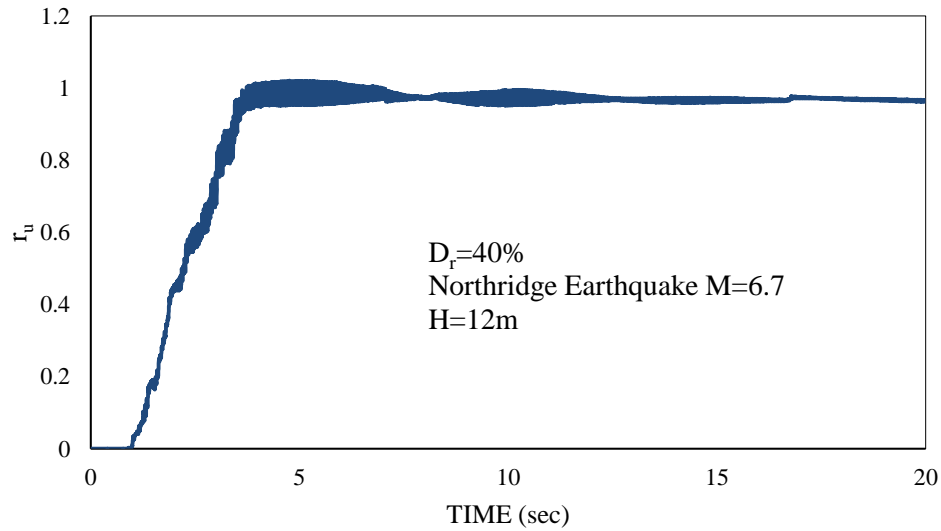


Figure 5.61: r_u generation at H=12m under Northridge Earthquake.

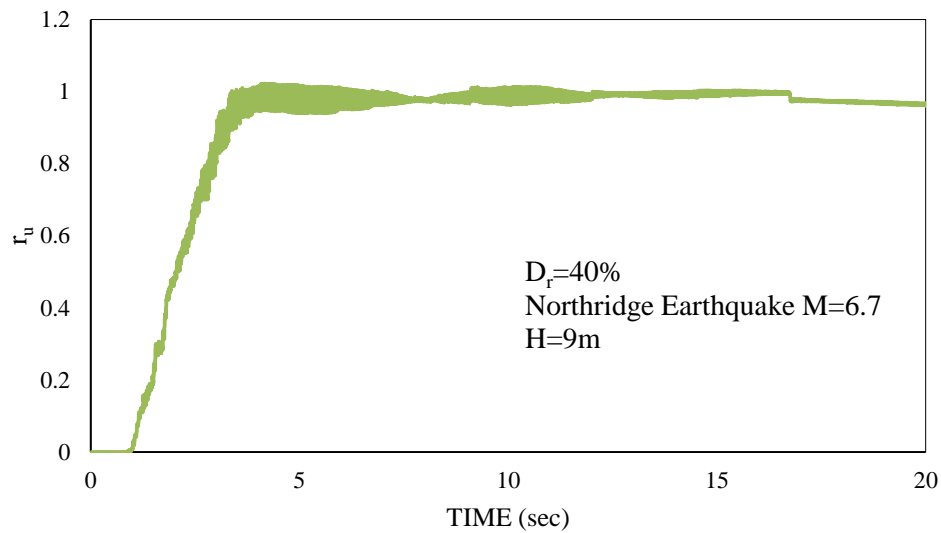


Figure 5.62: r_u generation at H=9m under Northridge Earthquake.

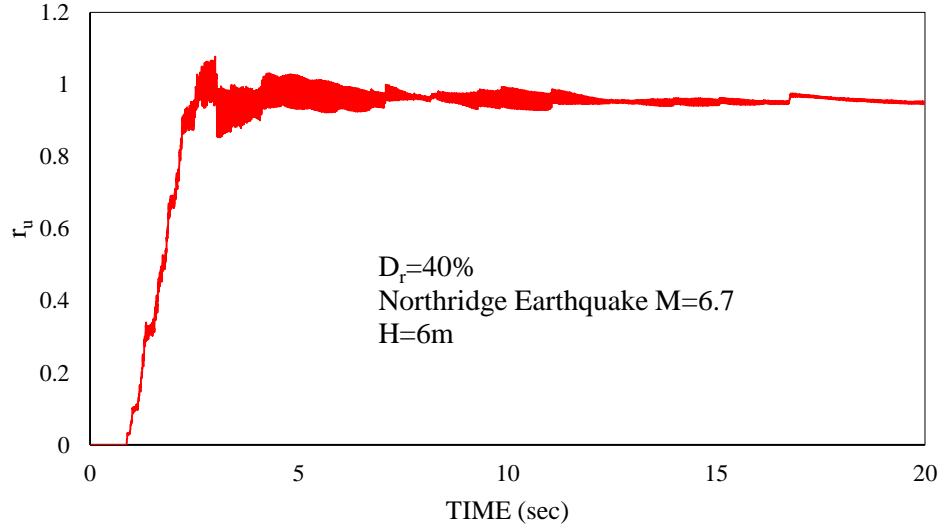


Figure 5.63: r_u generation at $H=6\text{m}$ under Northridge Earthquake.

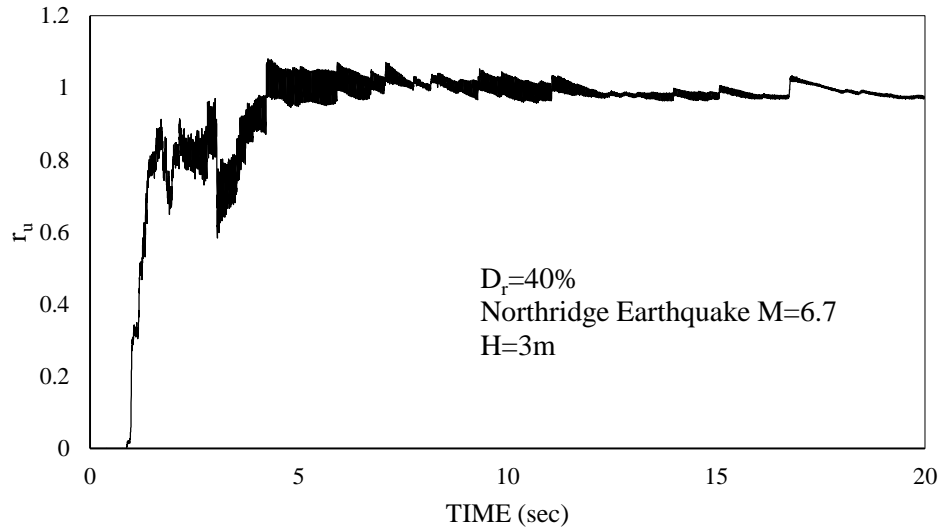


Figure 5.64: r_u deneneration at $H=3\text{m}$ under Northridge Earthquake.

As it can be seen in above mentioned figures, excess pore water pressure ratio reaches one in the first 3-5 seconds of the earthquake in all layers. This results confirms the liquefaction occurrence in the field under Northridge earthquake as determined from the N_γ/N_L formulation.

5.3.2 Numerical results for partially saturated sand in free-field

Liquefaction analysis is performed in the free-field sand model which is partially saturated under Northridge earthquake. Partially saturated sand is introduced in the

model again by changing the bulk modulus of the fluid in the voids, using Koning equation described at section 4.5.2:

$$\frac{1}{K_{WA}} = \frac{S}{K_W} + \frac{1-S}{u_w}$$

Parameters that are used for compressibility calculation, are degree of saturation (S), water bulk modulus (K_w) and absolute initial pore water pressure (u_w). K_w and S are parameters which have constant values. Absolute initial pore water pressure (u_w) is entered in the equation for each layer. Excess pore water pressure ratios generations for all layers are presented in figures 5.65, 5.66, 5.67, 5.68.

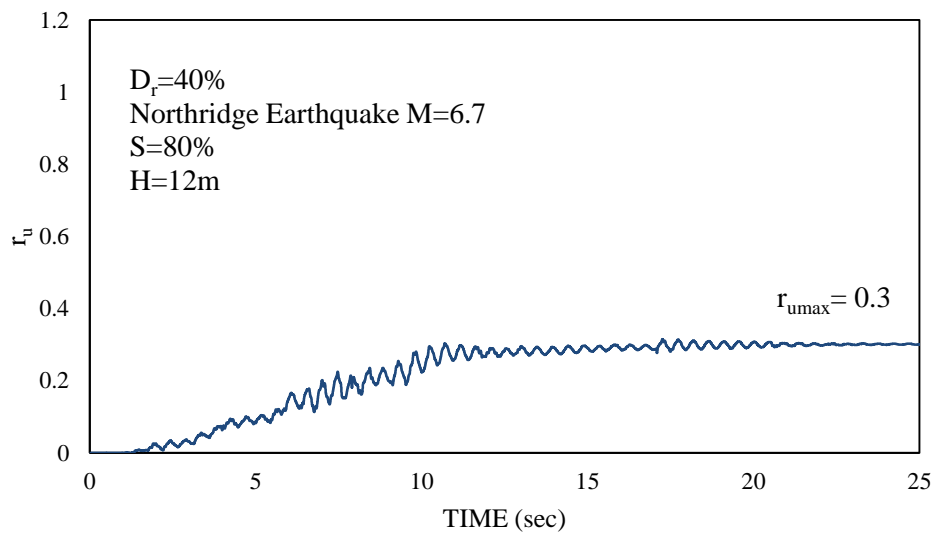


Figure 5.65: Pore pressure ratio for sand with $D_r=40\%$ and $S=80\%$ at $H=12\text{m}$.

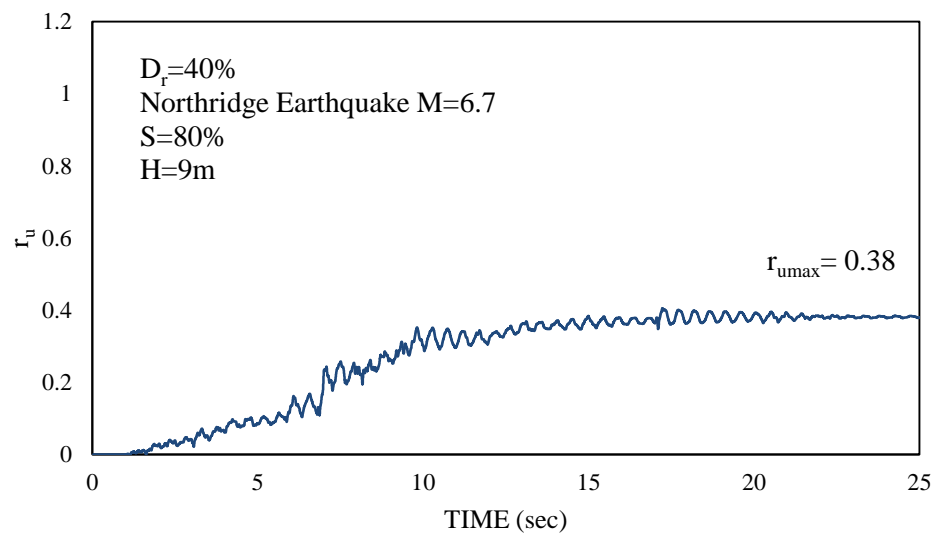


Figure 5.66: Pore pressure ratio for sand with $D_r=40\%$ and $S=80\%$ at $H=9\text{m}$.

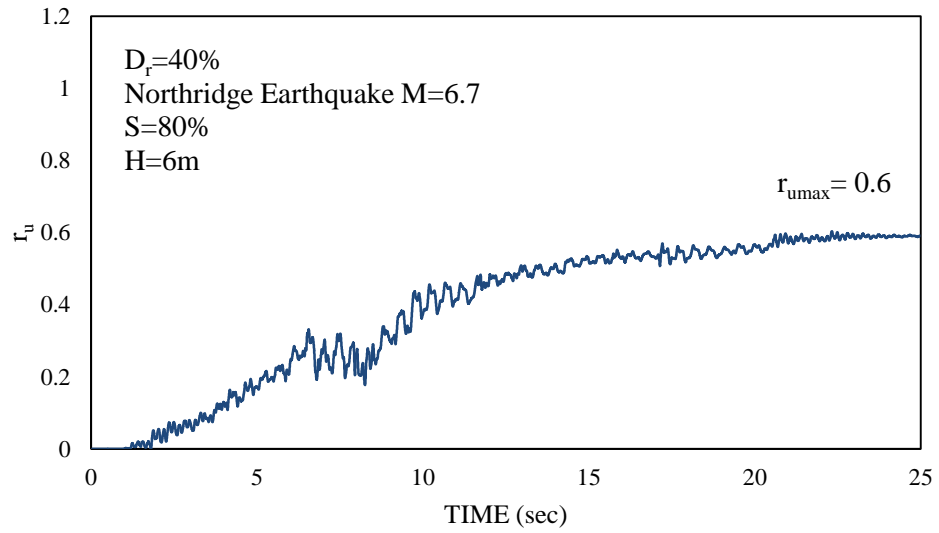


Figure 5.67: Pore pressure ratio for sand with $D_r=40\%$ and $S=80\%$ at $H=6\text{m}$.

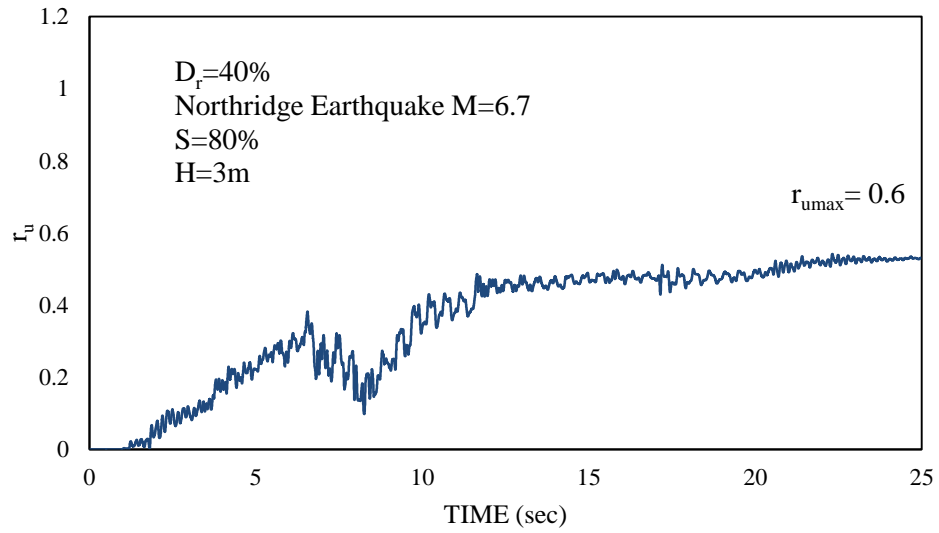


Figure 5.68: Pore pressure ratio for sand with $D_r=40\%$ and $S=80\%$ at $H=3\text{m}$.

RuPSS empirical model is a model for predicting excess pore water pressure ratio developed by Eseller-Bayat 2009. Excess pore water pressure ratio obtained from field numerical model is compared with r_u obtained from RuPSS. The progress of calculation of pore pressure ratio is mentioned in this part for $H=12\text{m}$. At first step $r_{u\max}$ is calculated

$$f = S^{0.5} * e^{-\left[\frac{1-S}{0.54}\right]^4} = 0.8^{0.5} * e^{-\left[\frac{1-0.8}{0.54}\right]^4} = 0.88$$

$$F_D = 1 - 8.75(0.4 - 0.2) * (1 - 0.8) * e^{\left[-\frac{(1-0.8)^2}{2 * \left(1 - 0.84 * \left(\frac{0.2}{0.4} \right)^{0.25} \right)^2} \right]} = 0.72$$

$$F_\gamma = 1 - 1.75 * \left(-\log \frac{0.007}{0.001} \right) * (1 - 0.8) * e^{[-3.1 * (1-0.8)^2]} = 1.25$$

$$r_{umax} = f * F_D * F_\gamma = 0.88 * 0.72 * 1.25 = 0.8$$

In the second step number of cycles to reach liquefaction N_{max} is calculated.

$$N_{max} = 48 * e^{\left(\frac{0.00035 * 0.4^2 * 100}{7 * 10^{-3}} - 3 * 0.33 \right)} = 8.12$$

N_γ is factor calculating the equivalent number of cycles of earthquake.

$$N_\gamma = 0.0065 * e^{\left[\left(\frac{10}{6.7-1} \right)^{1.8} + 0.72 * 6.7 \right]} = 12.66$$

$$\frac{N_\gamma}{N_{max}} \geq 1 \text{ then}$$

$$r_u = r_{umax} = 0.80$$

Excess pore water pressure ratio r_u is equal to r_{umax} since equivalent number of cycles due to the earthquake exceeds N_{max} .

Table 5.4 : Comparison of r_u 's obtained from RuPSS and numerical model.

H(m)	γ_{max}	γ_{eqv}	r_{umax}	N_{max}	r_u (RuPSS)	r_u (Numerical model)
3	0.01	0.0057	0.78	6.1	0.78	0.6
6	0.011	0.0063	0.79	6.3	0.79	0.6
9	0.008	0.0046	0.76	11.5	0.76	0.38
12	0.012	0.007	0.80	9.54	0.80	0.3

It can be seen from table 5.4 that pore pressure ratio calculated by numerical model is lower than the r_u obtained from RuPSS model. The r_u generation plots obtained from FLAC^{3D} confirm excess pore water pressure reaches the r_{umax} value and stays steady at that value.

These results imply that future research is needed to numerically model the partially saturated sands for liquefaction analysis.

6. SUMMARY AND CONCLUSION

The numerical modelling of sand behavior in a special setup (CSSLB, Cyclic Simple Shear Liquefaction Box) under cyclic simple shear conditions is presented in this thesis. After modelling the CSSLB and confirming uniform simple shear strains throughout the sand specimen, liquefaction analysis is performed in both fully saturated and partially saturated sand specimens.

Fully saturated Ottawa sand specimens (19x30x40 in cm) are modelled in CSSLB and numerically tested under cyclic simple shear strains using finite difference program FLAC^{3D}. The dynamic behavior and dynamic settlements are first investigated. Then after confirming the dynamic stability of the model, liquefaction analysis is conducted for a series of relative densities and shear strain amplitudes. The results are presented as excess pore water pressure ratio (r_u) and number of cycles necessary to reach liquefaction (N_L). The r_u and N_L values are compared with the experimental shaking table tests performed by Eseller-Bayat (2009). Liquefaction-induced settlements are also computed using Byrne model equation. The model was tested at high effective stresses, which could not be done in shaking table tests. A formulation for number of cycles to liquefaction (N_L) under cyclic simple shear testing conditions is developed.

The main objective of this thesis, for also future work, is to numerically model liquefaction behavior of partially saturated sands, especially obtained by a novel liquefaction mitigation technique IPS (Induced Partial Saturation) in FLAC^{3D}. After confirming the proper modelling of fully saturated sand specimens in CSSLB, partially saturated sand specimens are modeled by changing the bulk modulus of the water-air mixture in the voids using Koning (1963) equation. The results are compared with the shaking table test results by Eseller-Bayat (2009).

Finally, a free-field sand model (150x150x15 m) is constituted in FLAC^{3D} and tested under Northridge Earthquake M6.7 record in fully saturated loose as well as in partially

saturated loose conditions. The initiation of liquefaction in fully saturated sand is sought in FLAC 3D r_u output and compared with the methodology proposed by using the equivalent number of cycles N_γ and N_L formulation. In partially saturated condition, the excess pore water pressure ratio r_u generations are obtained and compared with the maximum excess pore water pressure ratio $r_{u\max}$ and r_u values obtained from RuPSS (r_u generated in partially saturated sands) empirical model results.

The following results can be drawn from this study:

1. A FLAC^{3D} code is prepared for testing fully and partially saturated sand specimens in CSSLB (Cyclic simple shear liquefaction box) under cyclic simple loading as on a shaking table. This code may be used for liquefaction testing of any type of sand under cyclic simple shear strain conditions.
2. The excess pore water pressure ratio r_u and number of cycles to liquefaction N_L values achieved at different relative densities and shear strain amplitudes are compatible with the experimental results for fully saturated sand, confirming the proper numerical modelling of the experimental tests.
3. One necessity for numerical modeling of the CSSLB setup was due to the limitation for testing specimens under high effective stresses. The liquefaction analysis is performed under high effective stresses in FLAC^{3D}. Based on a set of numerical data, a formulation for number of cycles to liquefaction N_L is developed as a function of initial effective stress, relative density and shear strain amplitude.
4. The future research aims to appropriately model the liquefaction behavior in partially saturated sands for the implementation of IPS in the field. Preliminary work is performed in this study and the model using Koning equation, which models the bulk modulus of air-water mixture in the voids, predicted the excess pore water pressures lower than the experimental results in high degrees of saturation (75-95%) and higher in low degrees of saturation (50-70%). Also, the number of cycles to N_{\max} (number of cycles to reach $r_{u\max}$) is much higher than the N_{\max} found in the experimental results. Future research is needed to suitably model the bulk modulus of the air-water mixture in the voids.

5. One of the achievements of this study is the modification of the N_{\max} , which is derived in RuPSS model based on experimental data by Eseller-Bayat (2009). N_{\max} was formulated in RuPSS by a normalized function to N_L . When N_L is modified for high effective stresses, N_{\max} is also improved for high effective stresses.
6. A procedure is proposed for the initiation of liquefaction of a sand layer under an earthquake loading when the relative density (or SPT N) is known. After ground response analysis, maximum shear strain amplitude the layer experiences is determined. Equivalent number of uniform cycles (N_γ) is determined using the earthquake magnitude M . N_L is found using the equivalent shear strain (γ_{eqv}), relative density, and initial effective stress. If $N_\gamma / N_L \geq 1$, initiation of liquefaction occurs. The proposed procedure is confirmed with numerical free-field model results.
7. The free-field model of partially saturated sand layer under an earthquake loading is compared with the results found from RuPSS model with modified N_{\max} formulation. According to the RuPSS model, the r_u generation in partially saturated sand reached to the r_{umax} , which is also confirmed in FLAC^{3D} results. However, the r_{umax} values in numerical analysis is smaller than the predicted values by RuPSS model. Further research is needed for the numerical modeling of the liquefaction resistance in partially saturated sands.

REFERENCES

- Byrne, P. M. (1991).** A Cyclic Shear Volume Coupling and Pore-Pressure Model for Sand. In *Second International Conference on Recent Advances in Geotechnical Engineering and Soil Dynamics* (pp. 47–55).
- Chaney, R. (1978).** “Saturation Effects on the Cyclic Strength of Sands”, *Earthquake Engineering and Soil Dynamics*, Vol.1, pp.342–358.
- Chaney, R., Demars, K., Santamarina, J., & Cho, G. (2001).** Determination of Critical State Parameters in Sandy Soils—Simple Procedure. *Geotechnical Testing Journal*, 24(2), 185. doi:10.1520/GTJ11338J
- Das, B. M. (n.d.).** _ 6th Edition of PRINCIPLES OF FOUNDATION ENGINEERING_0.pdf.
- De Alba, P and Pyke, R. . (1987).** Behavior of Embankments on Soft Soil under Earthquake Loading. *International Symposium on Geotechnical Engineering of Soft Soil-Mexico City*, 2, 125–141.
- Dobry, R.Ladd, R.S , Yokel, F.Y., Chung , R.M AND Poweel, D. (1982).** Prediction of Pore Water Pressure Buildup and Liquefaction of Sands during Earthquake by Cyclic Strain Method. *NBS Building Science Series 138 National Bureau of Standards , Gaithersburg, Maryland 150 Pp.*
- Eseller-Bayat. (2009).** Seismic Response and Prevention of Liquefaction Failure of Sands Partially Saturated Through Introduction of Gas Bubbles.
- Eseller-Bayat, E., Gokyer, S., Yegian, M. K., Ortakci, E., & Alshawabkeh, A. (2013).** Design and Application of Simple Shear Liquefaction Box. *Geotechnical Testing Journal*, 36(3), 20120025.
- Eseller-bayat, E., Yegian, M. K., & Alshawabkeh, A. (2013).** Liquefaction Response of Partially Saturated Sands. II : Empirical Model. *Journal of Geotechnical and Geoenvironmental Engineering*, (June), 872–879.
- FLAC 3D version 5, 2012. (2012).** 3 Dynamic Analysis, (dynamic analysis), 1–108.
- Hazirbaba, K. (2005).** Pore Pressure Generation of Silty Sands due to Induced Cyclic Shear Strains. *Journal of Geotechnical and Geoenvironmental Engineering*. doi:10.1061/(ASCE)GT.1943-5606.0000147

Ishihara, K. and Y. M. (1992). Evaluation of Settlement in Sand Deposits Following Liquefaction During Earthquake. *Soil and Foundations*, 32, 173–188.

Ishihara, K. & Tsukamoto, Y. (2004). “Cyclic Strength of Imperfectly Saturated Sand and Analysis of Liquefaction”, Proceedings of Japan Academy, Series B, Vol. 80 No. 8, pp. 372-391.

Koning, H. (1963). Some Observation on the Modulus of Compressibility of Water. In *settlement and compressibility of soil. wisbaden*.

Kramer, S. L. (1996). *Geotechnical Earthquake Engineering. Engineering* (Vol. 6). doi:10.1007/978-3-540-35783-4

Kuhlemeyer, R.L., and J. J. ysmers. (1973). Finite Element Method Accuracy for Wave Propagation Problems. *J. Soil Mech & Foundations, Div. ASCE*, 99, 421–427.

Lee K.L and Albaisa, A. (1974). Earthquake Induced Settlement in Saturated Sand. *Journal of the Soil Mechanics and Foundation Divisions. ASCE*, 100.

Liam Finn, W. D., Lee, K. W., & Martin, G. R. (1977). An effective stress model for liquefaction. *Journal of Geotechnical Engineering Division*, 103(ASCE), 517–533.

Marcuson, William F., III, Hynes, M.E and Franklin, A. G. (1990). Evaluation and Use of Residual Strength in Seismic safety Analysis of Embankments. *Earthquake Spectra*, 6, 529–572.

Martin, G. R., Seed, H. B., & Finn, W. D. L. (1975). Fundamentals of Liquefaction under Cyclic Loading. *Journal of the Geotechnical Engineering Division*, 101(5), 423–438.

Niels Saabye. (2005). Ottosen and Matti Ristinmaa: The Mechanics of Constitutive Modeling.

Okamura, M., Ishihara, M., Tamura, K. (2006). “Degree of Saturation and Liquefaction Resistances of Sand Improved with SCP”, *Journal of Geotechnical and Geoenvironmental Engineering*, ASCE, Vol. 132, No. 2, pp. 258-264.

Ortakci, E. (2007). Design and manufacturing of a cyclic simple shear box.

Schurmaan. (1967). The Compressibility of an air/water Mixture and a Theoretical Relation Between the air and water Pressures. *Géotechnique*, 17, 297–298. doi:10.1680/geot.1967.17.3.297

Seed, H. . and L. (1966). Liquefaction of Saturated Sands During Cyclic Loading. *Journal of Soil Mechanics & Foundations Division, ASCE*, 92, 105–134.

- Seed, H.B and Idriss, I. . (1971).** Simplified Procedure for Evaluating Soil Liquefaction Potential. *Journal of Soil Mechanics & Foundations Divison,ASCE, 107*, 1249–1274.
- Seed, H.B, Idriss I.M, Lee K, L. A. M. (1975).** The Slides in the San Feranando Dams During THE Earthquake of feb.9.1971. *Journal of Soil Mechanics & Foundations Division, ASCE, 101*, 651–688.
- Skoglund, G. R.Marcuson III, W.F and Cunny, R. . (1976).** “Evaluation of Resonant Test Column Test Devices.” *ASCE, 102*, 1147–1158.
- Tokimatsu, K and Seed, H. . (1987).** Evaluation of Settlement in Sand due to Earthquake Shaking. *Journal of Geotechnical Engineering ASCE, 113*, 861–878.
- Whitman, R. . (1971).** *Resistance of Soil to Liquefaction and Settelement.*
- Yang, J.,, Savidis, S., Sato, T., Li, X. S. (2003).** “Influence of Vertical Acceleration on Soil Liquefaction: New Findings and Implications”, Proc., of Soil and Rock America 2003, Cambridge, Massachusetts, Vol. 1, June.
- Youd, T. . . (1984).** Recurrence of Liquefaction at the Same Site. In *Proceedding. 8th world conference on Earthquake Engineering, Vol3* (pp. 231–238).

APPENDICES

Appendix A

Appendix B

Appendix C

Appendix A

Table A-1: Comparison of experimental and numerical results when $\gamma\%=0.05$

D_r %	$\gamma\%$	σ'_v kPa	Experimental Results	FLAC ^{3D} Results
31	0.0525	0.8	2.1	2.5
31	0.0525	2.5	3.2	3
42	0.0525	0.8	2.5	3
42	0.0525	2.5	3.9	3.2
55	0.052	0.8	4.3	3.5
55	0.052	2.5	5.3	4
62	0.051	0.8	4.3	3.5
62	0.051	2.5	5	4.5
89	0.055	0.8	4.2	4
89	0.055	2.2	5	5.5

Table A-2: Comparison of experimental and numerical results when $\gamma\%=0.01$

D_r %	$\gamma\%$	σ'_v kPa	Experimental Results	FLAC ^{3D} Results
32	0.01	0.8	4	4
32	0.01	2.5	7.4	6
38	0.01	0.8	4.3	5
38	0.01	2.5	6	8
50	0.012	0.8	5.8	8
50	0.012	2.5	6	16
58	0.012	0.8	5.9	12
58	0.012	2.5	6.1	22
68	0.012	0.8	6.7	15
68	0.012	2.5	6.2	30
75	0.012	0.8	6.4	25
75	0.012	2.5	6.4	45
89	0.012	0.8	7.1	32
89	0.012	2.5	7.1	65

Table A-3: Comparison of experimental and numerical results when $\gamma\%=0.1$

Dr %	$\gamma\%$	σ'_v kPa	Experimental Results	FLAC ^{3D} Results
40	0.1	0.8	3	2.4
40	0.1	2.5	3	2.6
48	0.1	0.8	3	2.5
48	0.1	2.5	3	3
55	0.1	0.8	3.1	2.8
55	0.1	2.5	3.1	3.5
62	0.1	0.8	3.1	2.7
62	0.1	2.5	3.1	3.8
69	0.1	0.8	3.1	3
69	0.1	2.5	3.1	4
88	0.1	0.8		4
88	0.1	2.5	4.3	4

Appendix B

Table B-1: Number of cycles to reach liquefaction under higher effective stress for sand with $D_r=20\%$.

D_r %	σ'_v kPa	$\gamma\%$	N_L (FLAC ^{3D})	N_L (Develpoed Equation)
20	2.1	0.052	2	2.5
20	2.7	0.052	2	2.6
20	4.7	0.052	3	2.7
20	6.5	0.052	4	2.8
20	8.7	0.052	4	3.0
20	13	0.052	5	3.4
20	17	0.052	5	3.7
20	21	0.052	5.5	4.1
20	32	0.052	6	5.5
20	42	0.052	6	7.2
20	52	0.052	8	9.3
20	62	0.052	10	12.1
20	72	0.052	14	15.7
20	82	0.052	19	20.4
20	92	0.052	28	26.4
20	103	0.052	34	35.2
20	123	0.052	50	59.3
20	144	0.052	89	102.5
20	165	0.052	140	177.2
20	2.7	0.1	2	2.5
20	4.7	0.1	2.5	2.6
20	6.5	0.1	3.5	2.6
20	8.7	0.1	3.5	2.7
20	13	0.1	4	2.9
20	17	0.1	4	3.0
20	21	0.1	4.5	3.2
20	32	0.1	5	3.7
20	42	0.1	5	4.2
20	52	0.1	6	4.9
20	62	0.1	6	5.6
20	72	0.1	6	6.4
20	82	0.1	7	7.3
20	92	0.1	8	8.4
20	103	0.1	8	9.7
20	123	0.1	12	12.7
20	144	0.1	15	16.9

20	165	0.1	20	22.5
20	185	0.1	25	29.5
20	205	0.1	38	38.7
20	250	0.1	54	71.1
20	290	0.1	90	122.3
20	320	0.1	150	183.7
20	4.7	0.15	2	2.4
20	8.7	0.15	3	2.6
20	13	0.15	3	2.7
20	17	0.15	4	2.8
20	21	0.15	4	2.9
20	32	0.15	4.5	3.2
20	42	0.15	4.5	3.5
20	52	0.15	5	3.8
20	62	0.15	5.5	4.2
20	72	0.15	6	4.6
20	82	0.15	6.5	5.0
20	92	0.15	6.5	5.5
20	103	0.15	7	6.1
20	123	0.15	7	7.3
20	144	0.15	7.5	8.8
20	165	0.15	9	10.7
20	185	0.15	12	12.8
20	205	0.15	14	15.3
20	250	0.15	20	23.0
20	290	0.15	29	33.0
20	320	0.15	43	43.3
20	370	0.15	60	68.0
20	410	0.15	90	97.6
20	450	0.15	130	140.1
20	2.7	0.2	2	2.4
20	6.5	0.2	3	2.5
20	8.7	0.2	3	2.5
20	13	0.2	4	2.6
20	17	0.2	4	2.7
20	21	0.2	5	2.8
20	32	0.2	5	3.0
20	72	0.2	6.5	3.9
20	92	0.2	7	4.5
20	123	0.2	8	5.5
20	144	0.2	10	6.4
20	165	0.2	10	7.3
20	205	0.2	11	9.6
20	250	0.2	12	13.1

20	290	0.2	14	17.1
20	320	0.2	20	21.0
20	370	0.2	28	29.5
20	410	0.2	36	38.7
20	520	0.2	75	81.5
20	620	0.2	144	160.5

Table B-2: Number of cycles to reach liquefaction under higher effective stress for sand with $D_r=40\%$.

D_r %	σ'_v kPa	$\gamma\%$	N_L (FLAC ^{3D})	N_L (Developed Equation)
40	2.1	0.052	4	3.0
40	2.7	0.052	5	3.2
40	4.2	0.052	4	3.8
40	7	0.052	5	5.1
40	11	0.052	6	7.8
40	12.5	0.052	8	9.2
40	17	0.052	14	15.0
40	21	0.052	18	23.0
40	25	0.052	26	35.4
40	30	0.052	39	60.7
40	34	0.052	58	93.4
40	38	0.052	85	143.7
40	42	0.052	124	221.1
40	46	0.052	184	340.1
40	2.1	0.1	2	2.7
40	2.7	0.1	2	2.8
40	4.2	0.1	3.5	3.0
40	7	0.1	4	3.5
40	11	0.1	5	4.4
40	12.5	0.1	5	4.8
40	17	0.1	6	6.1
40	21	0.1	11	7.6
40	25	0.1	11	9.5
40	30	0.1	12	12.5
40	34	0.1	13.5	15.6
40	38	0.1	14	19.4
40	42	0.1	17	24.2
40	46	0.1	22	30.1
40	50	0.1	26	37.5
40	55	0.1	32	49.4
40	58	0.1	39	58.2
40	63	0.1	48	76.7

40	73	0.1	78	132.9
40	83	0.1	128	230.2
40	94	0.1	210	421.5
40	2.1	0.15	3	2.6
40	2.7	0.15	3.5	2.6
40	4.2	0.15	3.5	2.8
40	7	0.15	4	3.1
40	11	0.15	4	3.6
40	12.5	0.15	5	3.8
40	17	0.15	5.5	4.5
40	21	0.15	6.5	5.2
40	25	0.15	6.5	6.0
40	30	0.15	6.5	7.2
40	34	0.15	9.5	8.3
40	38	0.15	10	9.7
40	42	0.15	10.5	11.2
40	46	0.15	11	13.0
40	50	0.15	12	15.0
40	55	0.15	15	18.0
40	58	0.15	18	20.1
40	63	0.15	20	24.2
40	73	0.15	29	34.9
40	83	0.15	41	50.3
40	94	0.15	60	75.3
40	104	0.15	84	108.6
40	123	0.15	170	217.9
40	2.1	0.2	2.5	2.5
40	2.7	0.2	2.5	2.6
40	4.2	0.2	3	2.7
40	7	0.2	4	2.9
40	11	0.2	5	3.2
40	12.5	0.2	5	3.4
40	17	0.2	5.5	3.8
40	21	0.2	6	4.3
40	25	0.2	7	4.8
40	30	0.2	7	5.5
40	34	0.2	7	6.1
40	38	0.2	8	6.8
40	42	0.2	8	7.6
40	46	0.2	8	8.5
40	50	0.2	10	9.5
40	55	0.2	11	10.9
40	58	0.2	12	11.8
40	63	0.2	12	13.6
40	73	0.2	15	17.9

40	83	0.2	18	23.5
40	93	0.2	24	30.9
40	103	0.2	32	40.7
40	113	0.2	41	53.6
40	123	0.2	55	70.6
40	145	0.2	94	129.2
40	165	0.2	158	224.0
40	2.7	0.25	2.7	2.5
40	4.2	0.25	2.7	2.6
40	7	0.25	3	2.8
40	11	0.25	4	3.1
40	12.5	0.25	5	3.2
40	17	0.25	5	3.5
40	21	0.25	6	3.8
40	25	0.25	6	4.2
40	30	0.25	6	4.6
40	34	0.25	6.5	5.1
40	38	0.25	7.5	5.5
40	42	0.25	7.5	6.0
40	46	0.25	7.5	6.6
40	50	0.25	7.5	7.2
40	58	0.25	9	8.6
40	73	0.25	11	12.0
40	83	0.25	12.5	14.9
40	93	0.25	16	18.6
40	103	0.25	19	23.1
40	113	0.25	24	28.8
40	123	0.25	30	35.9
40	145	0.25	45	58.2
40	165	0.25	70	90.4
40	185	0.25	106	140.4
40	205	0.25	164	217.9

Table B-3: Number of cycles to reach liquefaction under higher effective stress for sand with $D_r=60\%$.

D_r %	σ'_v kPa	$\gamma\%$	N_L (FLAC ^{3D})	N_L (Developed Equation)
60	2.1	0.052	3.5	4.0
60	2.7	0.052	4	4.6
60	4.7	0.052	7	7.4
60	6.5	0.052	12	11.4
60	8.7	0.052	22	19.3
60	13	0.052	62	54.2
60	17	0.052	190	141.6
60	2.1	0.1	3	3.1
60	2.7	0.1	4	3.4
60	4.7	0.1	4.5	4.3
60	6.5	0.1	5	5.4
60	8.7	0.1	6	7.1
60	13	0.1	11.5	12.1
60	17	0.1	21	20.0
60	21	0.1	38	32.9
60	25	0.1	62	54.2
60	29	0.1	100	89.3
60	34	0.1	175	166.7
60	2.1	0.15	3	2.9
60	2.7	0.15	3.7	3.0
60	4.7	0.15	4	3.5
60	6.5	0.15	4.5	4.1
60	8.7	0.15	5	4.9
60	13	0.15	6	7.1
60	17	0.15	9.5	9.9
60	21	0.15	14	13.8
60	25	0.15	18	19.2
60	29	0.15	26	26.8
60	34	0.15	38	40.5
60	38	0.15	54	56.5
60	42	0.15	71	78.9
60	52	0.15	160	181.1
60	2.1	0.2	2.5	2.7
60	2.7	0.2	2.5	2.8
60	4.7	0.2	3.5	3.2
60	6.5	0.2	4	3.6
60	8.7	0.2	4.5	4.1

60	13	0.2	5	5.4
60	17	0.2	6	6.9
60	21	0.2	9	8.9
60	25	0.2	12	11.4
60	29	0.2	16	14.6
60	34	0.2	20	20.0
60	38	0.2	28	25.7
60	42	0.2	38	32.9
60	52	0.2	74	61.4
60	62	0.2	145	114.6
60	2.1	0.2	3	2.7
60	2.7	0.2	3	2.7
60	4.7	0.2	4	3.0
60	6.5	0.2	4.5	3.3
60	8.7	0.2	4.5	3.7
60	13	0.2	6	4.6
60	17	0.2	6.5	5.6
60	21	0.2	7	6.8
60	25	0.2	8	8.4
60	29	0.2	10	10.2
60	34	0.2	12	13.1
60	38	0.2	15	16.0
60	42	0.2	19	19.5
60	52	0.2	32	32.1
60	62	0.2	55	52.9
60	72	0.2	88	87.1
60	83	0.2	145	150.8

Appendix C

FLAC^{3D} Code (Liquefaction Analysis)

```
;-----  
; Cyclic Simple Shear Liquefaction Box (CSSLB)  
;-----  
;  
new  
  
define constant  
Dr=50  
  
shearmod=7.2e6  
bulkmod=2.75e7  
  
porosity=0.4  
friction=30  
  
drydensity=1500  
  
amplitude=0.03  
frequency=10  
  
verticalstress=-0e4  
horizontalstress=0e4  
  
solveage=10  
end  
@constant  
; There is no automatic correction  
set fish autcreate off  
;  
; Sets the model Title.  
title "Dynamic analysis --- Shaking table test"  
; Dynamic analysis is set off at first for calculating unbalanced force in static  
condition  
set dyn off  
; Walls of the CSSLB are going to generated and name is assigned for each wall  
; fixeds slidewalls  
gen zone brick size 1,1,1 p0 (0.01,0,0.3) p1 (0.18,0,0.3) p2 (0.01,0.49,0.3) ...  
p3 (0.01,0,0.32) group boundary1  
fix x y z range group boundary1  
gen zone brick size 1,1,1 p0 (0.01,0,-0.02) p1 (0.18,0,-0.02) p2 (0.01,0.49,-0.02) ...  
p3 (0.01,0,0) group boundary2  
fix x y z range group boundary2  
;.....  
.....
```

```

; Rotating sidewalls
gen zone brick size 1,1,1 p0 (0.19,0.01,-0.02) p1 (0.21,0.01,-0.02) p2 (0.19,0.49,-
0.02) ...
p3 (0.19,0.01,0.32) group largeboundary1
fix y z range group largeboundary1
;
gen zone brick size 1,1,1 p0 (-0.02,0.01,-0.02) p1 (0,0.01,-0.02) p2 (-0.02,0.49,-0.02)
...
p3 (-0.02,0.01,0.32) group largeboundary2
fix y z range group largeboundary2
;
;.....
.....
; Bottom of the box
gen zone brick size 1,1,1 p0 (-0.11,-0.02,-0.2) p1 (0.3,-0.02,-0.2) p2 (-0.11,0,-0.2) ...
p3 (-0.11,-0.02,0.5) group bottom
fix y z range group bottom
;.....
.....
; rubber
gen zone brick size 1,1,1 p0 (0,0,0.3) p1 (0,0,0.32) p2 (0.01,0,0.3) ...
p3 (0,0.49,0.3) group rubber1
fix x y z range group rubber1
gen zone brick size 1,1,1 p0 (0,0,0) p1 (0,0.49,0) p2 (0.01,0,0) ...
p3 (0,0,-0.02) group rubber2
fix x y z range group rubber2
gen zone brick size 1,1,1 p0 (0.18,0,0.3) p1 (0.18,0,0.32) p2 (0.19,0,0.3) ...
p3 (0.18,0.49,0.3) group rubber3
fix x y z range group rubber3
gen zone brick size 1,1,1 p0 (0.18,0,0) p1 (0.18,0.49,0) p2 (0.19,0,0) ...
p3 (0.18,0,-0.02) group rubber4
fix x y z range group rubber4
gen zone brick size 1,1,1 p0 (-0.02,0,-0.02) p1 (0,0,-0.02) p2 (-0.02,0.01,-0.02) ...
p3 (-0.02,0,0.32) group bottomrubber1
fix x y z range group bottomrubber1
gen zone brick size 1,1,1 p0 (0.19,0,-0.02) p1 (0.21,0,-0.02) p2 (0.19,0.01,-0.02) ...
p3 (0.19,0,0.32) group bottomrubber2
fix x y z range group bottomrubber2

;.....
.....
; Walls are defined as an elastic material
model mech elastic range group boundary1
prop bulk 2e11 shear 1e11
model mech elastic range group boundary2
prop bulk 2e11 shear 1e11
model mech elastic range group largeboundary1
prop bulk 2e11 shear 1e11
model mech elastic range group largeboundary2
prop bulk 2e11 shear 1e11

```

```

model mech elastic range group bottom
prop bulk 2e11 shear 1e11
; Rubbers are defined as an elastic material
model mech elastic range group rubber1
prop bulk 2.5e5 shear 8.333e5
model mech elastic range group rubber2
prop bulk 2.5e5 shear 8.333e5
model mech elastic range group rubber3
prop bulk 2.5e5 shear 8.333e5
model mech elastic range group rubber4
prop bulk 2.5e5 shear 8.333e5
model mech elastic range group bottomrubber1
prop bulk 2.5e5 shear 8.333e5
model mech elastic range group bottomrubber2
prop bulk 2.5e5 shear 8.333e5
;set large
;.....
;.....
; Defining the sand model
gen zone brick size 1,2,2 p1 (0.19,0,0) p2 (0,0.4,0) p3 (0,0,0.3) group byrne
;plot zone

; constitutive models.
model mech finn range group byrne
;
; Fluid is defined as an isotropic material
model fluid fl_iso
;Setting direction and quantity of gravity acceleration
set grav 0,-10,0
;y is fixed at the bottom of the box
fix y range y 0.0
; Fixes x-velocity and y-velocity
fix x z

; The fluid flow calculation may be turned off for a mechanical-only calculation or a
thermal-only
; calculation.
set fluid off

;.....
;.....
; Define mass density in kg/m^3 , shear and bulk modulus K in pa
prop dens @Drydensity shear @shearmod bulk @bulkmod ;dry density should to be
assigned
;angle of friction , Porosity n
prop fric @friction poros @porosity

;.....
;.....

```

```

; Minimum number of timesteps between reversals that is defined only in FINN
model
prop ff_latency=50
;.....

; Fluid bulk modulus for fluid-flow model in pa
ini fmod 2.2e9 fden 1000 ;6.37e5
; Fluid bulk modulus for fluid-flow model in pa
;.....

ini pp 0.4e4 grad 0 -1.00e4 0
ini syy -0.8e4 grad 0 2.00e4 0 ;initial value 0.8e4 (pa)
ini sxx -0.64e4 grad 0 1.6e4 0 ;initial value 0.64e4 (pa)
ini szz -0.64e4 grad 0 1.6e4 0 ;initial value 0.64e4 (pa)

;Applying vertical forces to the sample
apply syy @verticalstress range y 0.39 0.41
apply sxx @horizontalstress range x 0
apply sxx @horizontalstress range x 0.19
apply szz @horizontalstress range z 0
apply szz @horizontalstress range z 0.3

;.....

hist add unbal
solve
;set dytime 0
set dyn on
;.....

; Parameters for Byrne formula
def setCoeffByrne(n1_60)
local val_c1 = 7600*((Dr)^(-2.5)) ;the input is relative density in percent
global ff_c1 = 0.5*val_c1
global ff_c2 = 0.4/val_c1
global ff_c3 = 0.0000
end
@setCoeffByrne(6)
prop ff_switch=1 ff_c1=@ff_c1 ff_c2=@ff_c2 ff_c3=@ff_c3 range group Byrne
;.....

; Constant point for hist are defined
define constants
global pzm = z_near(0.095,0.115,0.195)
global pzb = z_near(0.095,0.30,0.15)
global pzb1 = z_near(0.095,0.27,0.15)
global pzb2 = z_near(0.095,0.15,0.15)

```

```

;
global pgp1b = gp_near(0.0475,0.49,0.075)
global pgp2b = gp_near(0.1425,0.49,0.075)
global pgp3b = gp_near(0.0475,0.49,0.225)
global pgp4b = gp_near(0.1425,0.49,0.225)
global pgp5b = gp_near(0.095,0.06,0.15)
global pgp6b = gp_near(0.095,0.11,0.15)
global pgp7b = gp_near(0.095,0.24,0.15)
global pgp8b = gp_near(0.095,0.26,0.15)
global pgp9b = gp_near(0.095,0.39,0.15)
global pgp10b = gp_near(0.095,0.41,0.15)
global pgp11b = gp_near(0.095,0.1,0.15)
global pgp12b = gp_near(0.095,0.25,0.15)
global pgp13b = gp_near(0.095,0.4,0.15)
global pgp14b = gp_near(0.095,0.01,0.15)
global pgp15b = gp_near(0.095,0.1,0.15)
;
global freq
global ampl
end
@constants
;.....
.....
; Assigned dynamic load is defined
define sine_wave
whilestepping
;if dytime<0.1
;Execute during every step, amplitude and freq are going to defined at the end of the
code
global vv = ampl * sin(2.0 * pi * freq * dytime)
;dytime creates a history of real time for dynamic problems (only available for
dynamic model option)
loop foreach local p_gp gp_list
; gridpoint data. An optional keyword can be specified to display selected gridpoint
data. The following keywords apply:
local vvv = vv * (0.49 - gp_ypos(p_gp))/0.49
gp_xvel(p_gp) = vvv
endloop
;else
;vvv=0
;end_if
end
@sine_wave
;.....
.....
; Effective stress is defined as a FISH
def eff_stress_b
local tmp = (z_sxx(pzb);
eff_stress_b = tmp + z_pp(pzb)
end

```

```

@eff_stress_b
;.....
.....
def eff_stress_b1
local tmp1 = (z_sxx(pzb1);
eff_stress_b1 = tmp1 + z_pp(pzb1)
end
@eff_stress_b1
;.....
.....
def eff_stress_b2
local tmp2 = (z_syy(pzb2))
eff_stress_b2 = tmp2 + z_pp(pzb2)
end
@eff_stress_b2
;.....
.....
; Calculating the shear strain by dividing relative displacement on the height of the
zone
def strain1 ;one dimensional earthquake excitation of uniform layer
*****
strain1 = ((gp_xdisp(pgp6b) - gp_xdisp(pgp5b))/0.2) ;height of each zone 0.4/2=0.2
end
@strain1
def strain2
strain2 = ((gp_xdisp(pgp8b) - gp_xdisp(pgp7b))/0.2)
end
@strain2
def strain3
strain3 = ((gp_xdisp(pgp10b) - gp_xdisp(pgp9b))/0.2)
end
@strain3
;.....
.....
; Rayleigh damping is assigned beside the hyst damping to decrease the noise
set dyn damp ray 0.0005 10
ini damp hyst sig3 1.014 -0.4792 -1.249

;.....
.....

set dyn dt 1e-4
hist add dytime
hist add fish @strain1
hist add fish @strain2
hist add fish @strain3
hist add zone sxy 0.095 0.1 0.15
hist add zone sxy 0.095 0.25 0.15
hist add zone sxy 0.095 0.4 0.15
;

```

```

hist add gp ydisp 0.0475 0.49 0.075
hist add gp ydisp 0.1425 0.49 0.075
hist add gp ydisp 0.0475 0.49 0.225
hist add gp ydisp 0.1425 0.49 0.225
hist add gp ydisp 0.0475 0.49 0.075
hist add gp ydisp 0.1425 0.49 0.075
hist add gp ydisp 0.0475 0.49 0.225
hist add gp ydisp 0.1425 0.49 0.225
;
; Plot of pore pressure for different points
hist add zone pp 0.095,0.4,0.15
hist add zone pp 0.095,0.24,0.15
hist add zone pp 0.095,0.15,0.15
;
hist add fish @eff_stress_b
hist add fish @eff_stress_b1
hist add fish @eff_stress_b2

hist add zone vsr 0.0475 0.35 0.075
hist add zone vsr 0.0475 0.15 0.075

hist add zone vsi 0.0475 0.35 0.075
hist add zone vsi 0.0475 0.15 0.165
hist add zone vsi 0.1475 0.35 0.165
hist add zone vsi 0.1475 0.15 0.075

list hist

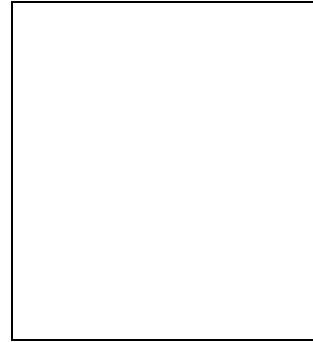
list zone strain
;.....
.....

;Program monitors changes in Variables, in mentioned steps
hist nstep 100
;
; Amplitude of the applied velocity wave
set @ampl=@amplitude @freq=@frequency
save stt-ini
;
; Number of stages that problem is going to be solved
solve age @solveage

;
return

```


CURRICULUM VITAE



Name Surname: Ataollah Nateghi

Place and Date of Birth: Iran/Tabriz 09/08/1988

E-Mail: ataollahnateghi@gmail.com

nateghi@itu.edu.tr

EDUCATION: Bachelor of science

B.Sc.: Tabriz University